THE SOLAR EXTREME ULTRA-VIOLET CORONA: RESOLVED LOOPS AND THE UNRESOLVED ACTIVE REGION CORONA

by

Jonathan Wesley Cirtain

A dissertation submitted in partial fulfillment
of the requirements for the degree

of

Doctor of Philosophy

in

Physics

MONTANA STATE UNIVERSITY
Bozeman, Montana

April 2005

APPROVAL

of a dissertation submitted by

Jonathan Wesley Cirtain

This dissertation has been read by each member of the dissertation committee and has been found to be satisfactory regarding content, English usage, format, citations, bibliographic style, and consistency, and is ready for submission to the College of Graduate Studies.

Dana W. Longcope, Ph. D.

Approved for the Department of Physics

Dr. William Hiscock

Approved for the College of Graduate Studies

Dr. Bruce McLeod

STATEMENT OF PERMISSION TO USE

In presenting this dissertation in partial fulfillment of the requirements for a doctoral degree at Montana State University, I agree that the Library shall make it available to borrowers under rules of the Library. I further agree that copying of this dissertation is allowable only for scholarly purpose, consistent with "fair use" as prescribed in the U.S. Copyright Law. Requests for extensive copying or reproduction of this dissertation should be referred to Bell & Howell Information and Learning, 300 North Zeeb Road, Ann Arbor, Michigan 48106, to whom I have granted "the exclusive right to reproduce and distribute my dissertation in and from microform along with the non-exclusive right to reproduce and distribute my abstract in any format in whole or in part."

Jonathan Wesley Cirtain

DATE

I kept my promise Dad.
Melissa, you made this possible.
I love you.

ACKNOWLEDGMENTS

Mom, thanks for buying me telescopes. You have always supported me in the productive things I tried, and I love you. You are the best. (I am a DR. first).

I must say that my experience at Montana was not always a pleasure. However, Piet you were always supportive and it truly was my pleasure to have you for a mentor. Thank you for putting up with me. Dana, I learned more from our numerous conversations than you may know. I appreciate how you forced me to learn to analyze situations and critically think about physics and math. Charles, I appreciate your teaching me to TRACE plan, and for reading my thesis. I also thank all of my committee members for their participation in this endeavor. I would like to thank NASA for paying my bills and affording me the fantastic opportunity to pursue my dream of being an astronomer. I am especially grateful for the support of Dr. Joe Gurman of NASA/GSFC for supporting my fellowship. The TRACE science team was equally supportive and I owe a great deal to the scientists at Lockheed Martin for the honor of serving as science planner.

Alisdair, I taught you to play golf and you beat me at it. I thank you and Meredith for numerous science discussions and for reading my thesis. I will start paying for the beers (and occasionally golf) now that I have a real job.

Trae, Andrew, Angela and Trish: I really enjoyed being in 'our' little group. I will always think of you as my friends and hope you would feel free to call on me if you ever need my help. Andrew, talking with you about physics was fantastic. You really enriched my graduate school experience with the insight you offer to some complicated problems. Thank you for that.

Finally, I would like to thank Ed Deluca, Leon Golub and Mark Weber for having me out to SAO. I have learned more about the science of observing in the short time I have been there than I knew before. I am also grateful you hired me.

TABLE OF CONTENTS

LIST OF TABLES

LIST OF FIGURES

ABSTRACT

In this work, physical characteristics of the solar corona as observed in the Extreme Ultra-Violet (EUV) regime are investigated. The focus will be the regions of intense EUV radiation generally found near the locations of sunspots. These regions are commonly called active regions. Multiple space-based observing platforms have been deployed in the last decade; it is possible to use several of these observatories in combination to develop a more complete picture of the solar corona. Joint Observing Program 146 was created to collect spectroscopic intensities using the Coronal Diagnostic Spectrometer on Solar and Heliospheric Observatory and EUV images using NASA's Transition Region and Coronal Explorer.

The emission line intensities are analyzed to develop an understanding of the temperature and density of the active region coronal plasma. However, the performance of the CDS instrument in the spatial and temporal domains is limited and to compensate for these limitations, data collected by the TRACE instrument provide a high spatial and temporal resolution set of observations.

One of the most exciting unsolved problems in solar astrophysics is to understand why the corona maintains a temperature roughly two orders of magnitude higher than the underlying material. A detailed investigation of the coronal emission has provided constraints on models of the heating mechanism, since the temperature, density and evolution of emission rates for multiple ionic species are indicative of the mechanism(s) working to heat the corona. The corona appears to consist of multiple unresolved structures as well as resolved active region structures, called coronal loops. The purpose of the present work is to determine the characteristics of the unresolved background corona. Using the characterizations of the coronal unresolved background, results for loops after background subtraction are also presented. This work demonstrates the magnitude of the unresolved coronal emission with respect to the total emission along the line of sight, and the relationship of the coronal background emission to the resolved loop emission. It is apparent from this analysis that the unresolved corona is the dominant source of radiation in active regions. Additionally, the unresolved active region coronal emission can be characterized by hydrostatic scaling laws.

CHAPTER 1

THE STRUCTURE OF THE SOLAR CORONA

Introduction

During a solar eclipse, the disk of the sun can be completely obscured by the passage of the moon between the sun and the earth. Observations of solar eclipses were first recorded by the Chinese nearly four thousand years ago. During these rare events, the solar atmosphere becomes visible. The earliest observers of solar eclipses did not realize that the filamentary structures observed during these events were the solar atmosphere. In the 19^{th} century it was decided that this was in fact a solar phenomenon. The solar corona varied in extent and brightness from one eclipse observation to the next, and this was the state of coronal observations until the invention of the coronagraph in the twentieth century [7]. An example of a solar eclipse observation is shown in Figure 1.1 [1].

The solar corona is dynamic; its extent and density are highly dependent on the underlying structure of the magnetic field. Figure 1.2 shows two images. The image on the right was taken by the Soft X-ray Telescope (SXT) [8] on the Japanese satellite *Yohkoh* and an image taken with the Extreme Ultraviolet Imaging Telescope (EIT) [9] on the Solar and Heliospheric Observatory (SoHO) [10]. These images show several bright areas called active regions (AR); these regions appear above sunspots, locations of intense magnetic flux emergence from the solar convective zone. Figure 1.3 is a magnetogram taken by the Michelson Doppler Imager (MDI) [11] on SoHO.

[1] Image courtesy of http://www.aa6g.org/Astronomy/Eclipses/solareclipse.html

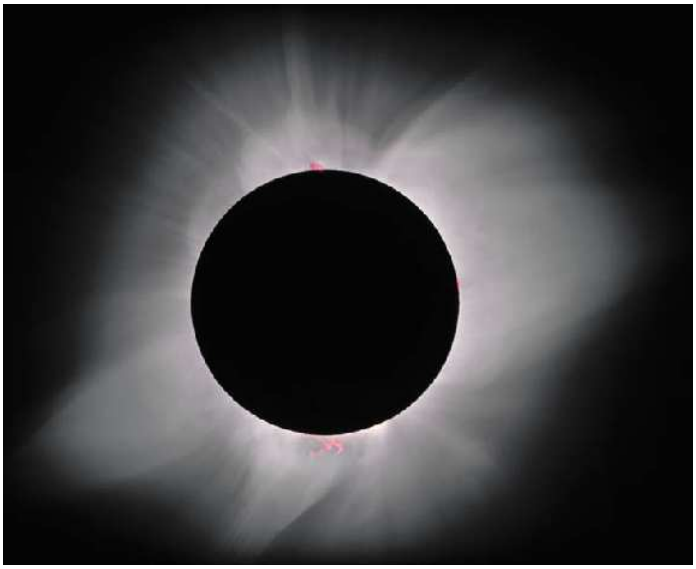

Figure 1.1: Solar eclipse observed July 11, 1991 near Baja, CA.

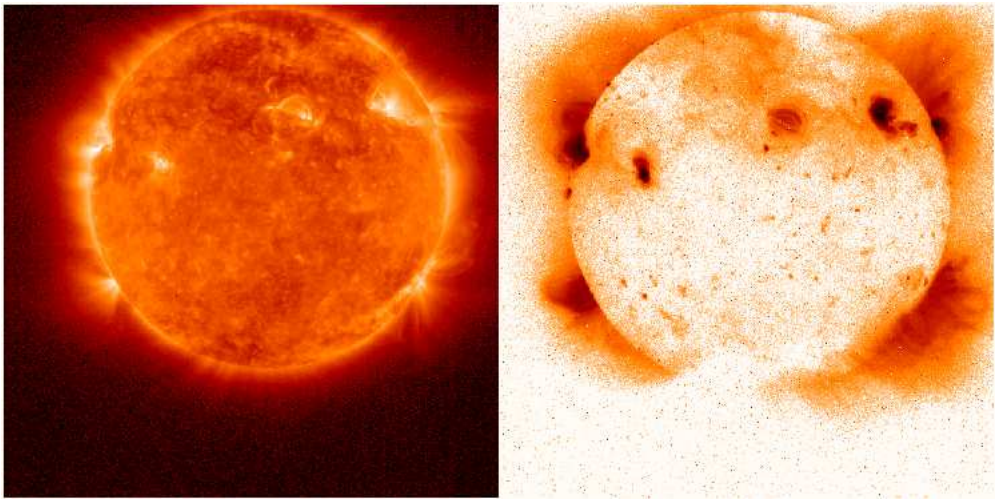

Figure 1.2: Simultaneous images of the sun in EUV (left) and X-ray (right). Image taken 22-June-1998.

The bright and dark concentrations are co-spatial with observed sunspots in visible light images. The atmosphere above locations of flux emergence is heated to high temperatures (> 1 MK). This is evidenced by the X-ray and Extreme Ultraviolet (EUV) radiation which is being emitted by the highly ionized gas that exists at such temperatures.

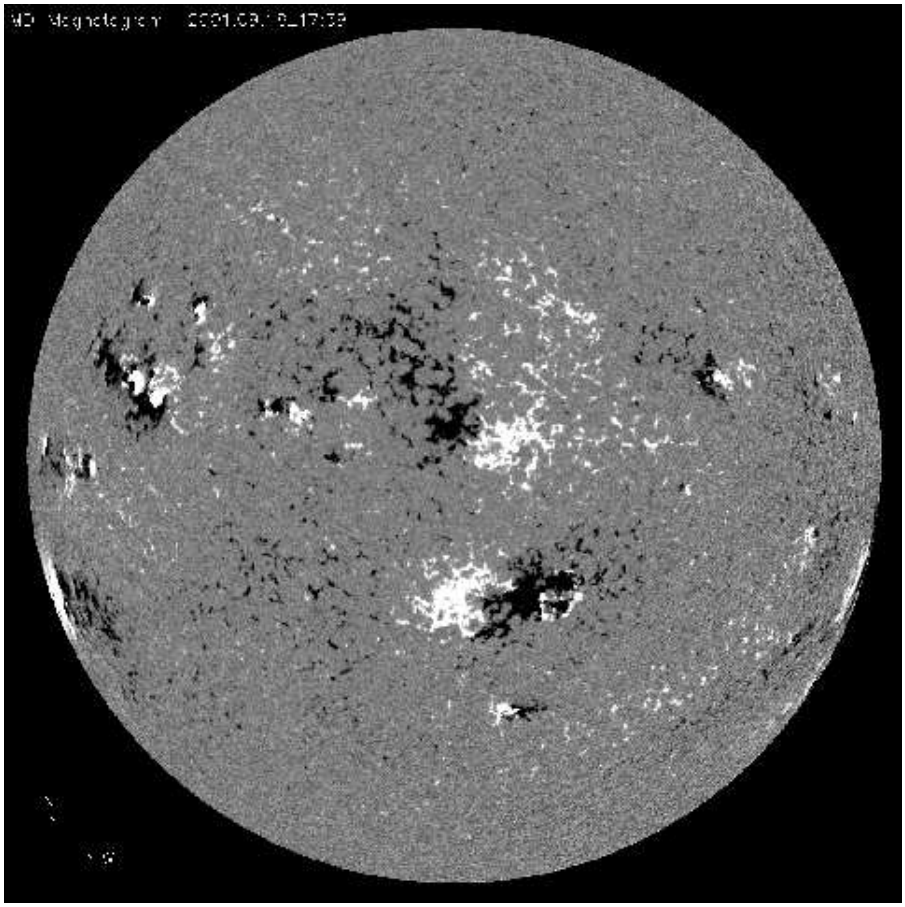

Figure 1.3: MDI magnetogram from September 18, 2001 at 1739 UT.

The Solar Magnetic Field

With the advent of UV and X-ray imaging, the ubiquitous nature of the solar corona became apparent, much as Alfvén had predicted [12]. It is now widely believed that the topology of the magnetic field dominates the inner solar atmosphere, independent of the scale of the structures observed, e.g. coronal loops, X-ray bright points, prominences, etc. It is clear from the high resolution images now available that understanding the magnetic field connectivity, whether it is closed within the AR, or is open to the interplanetary field, is essential to determining the coronal temperature and density distributions.

The most abundant coronal structure is the coronal loop, which is taken as observational evidence for the existence of magnetic fields in the coronal volume. Field lines exit from and return to the photosphere; some lines rise into the corona and return forming a closed loop while others effectively do not (i.e. open lines). These "open" field lines do eventually close, either with the interplanetary magnetic field (IMF), galactic magnetic field, or elsewhere. Plasma at the photosphere is free to move mechanically and carries these lines of force along such that elements of the plasma initially at the footpoints of the loops remain connected to the field lines on which they started. These photospheric motions are quasi-random, and as the field lines become increasingly twisted, the magnetic field in the corona is necessarily stressed until coronal magnetic field develops an instabilities which returns the atmosphere toward a current-free (i.e. potential field) configuration.

Given this simplistic introduction to the solar corona and the magnetic field plasma coupling that shapes the nature of the solar atmosphere, a more formal description of the equations describing the physics of the corona is in order. The mechanism responsible for the generation of the emergent magnetic flux, the solar dynamo, is beyond the scope of this thesis. As such, it will be assumed that magnetic field is generated below the photosphere and emerges into the corona. The following discussion will detail the frozen-in-flux concept, provide a simple model of the coronal field based on observations, and examine the most basic model of the solar corona, the hydrostatic atmosphere.

Frozen-in-Flux

In a seminal paper, Alfvén [13] introduced the concept of flux-freezing. In the non-relativistic limit, Ohm's law

$$\vec{j} = \frac{1}{\eta}(\vec{E} + \frac{\vec{v}}{c} \times \vec{B}) \quad , \tag{1.1}$$

with $\vec{j}$ the current density, $\vec{B}$ the magnetic induction, $\vec{E}$ the electric field, and η the electric resistivity, can be combined with the Maxwell relation

$$\bigtriangledown \times \vec{B} = \mu_0 \vec{j} \quad . \tag{1.2}$$

This allows the electric field $\vec{E}$ to be written in terms of $\vec{B}$ and $\vec{j}$

$$\vec{E} = \frac{\eta}{\mu_o} \bigtriangledown \times \vec{B} - \frac{\vec{v}}{c} \times \vec{B} \quad . \tag{1.3}$$

Substitution of equation 1.3 into Faraday's law, written as

$$\frac{\partial \vec{B}}{\partial t} = -c \vec{\bigtriangledown} \times \vec{E} \quad . \tag{1.4}$$

yields the induction equation and it is one of the most important equations in MHD. It is written

$$\frac{\partial \vec{B}}{\partial t} = \bigtriangledown \times (\vec{v} \times \vec{B}) + \lambda \bigtriangledown^2 \vec{B} \quad . \tag{1.5}$$

It is often the practice in MHD to take the ratio of the two terms in the induction equation to determine the dominant term. The dimensionless number, R_m, is the ratio of the terms from the induction equation and is called the magnetic Reynolds number. It is written

$$R_m = \frac{\mu_0 L V}{\eta} \quad , \tag{1.6}$$

with μ_0 the permeability of free space, L a characteristic length, V the volume and η the electrical resistivity (Choudhuri [14]). For many astronomical plasmas $R_m > 10^6$ so the second term can be neglected and the induction equation becomes

$$\frac{\partial \vec{B}}{\partial t} = \vec{\bigtriangledown} \times (\vec{v} \times \vec{B}) \quad . \tag{1.7}$$

This is the ideal form of the induction equation. If a surface, S, is bounded by a curve, C, and this surface is moving with the plasma, it will trace out an element of volume equal to $\vec{v} \times d\vec{s}\ dt$. Here dt is an element of time, $d\vec{s}$ is an element of the curve C, and $\vec{v}$ is the velocity of the plasma. The time rate of change of the flux of $\vec{B}$ through C is then

$$\frac{d}{dt}\int_S \vec{B}\cdot d\vec{S} = \int_S \frac{\partial \vec{B}}{\partial t}\cdot d\vec{S} + \int_C \vec{B}\cdot \vec{v}\times d\vec{s}\ \ . \tag{1.8}$$

The second term on the right hand side of equation 1.9 may be rewritten, using the identities of the triple product, to yield

$$\vec{B}\cdot\vec{v}\times d\vec{s} = -\vec{v}\times\vec{B}\cdot d\vec{s}\ \ . \tag{1.9}$$

Substitution of equation 1.10 into 1.9 and applying Stokes' theorem to the contour integral produces

$$\frac{d}{dt}\int_S \vec{B}\cdot d\vec{S} = \int_S (\frac{\partial \vec{B}}{\partial t} - \vec{\bigtriangledown}\times(\vec{v}\times\vec{B}))\cdot d\vec{S}\ \ . \tag{1.10}$$

Now equation 1.11 will equal zero in the limit of the ideal induction equation assumed initially. So the net flux through the surface S, bounded by C, is a constant as C moves along with the plasma, tracing out an area equal to $dt\int_C v\times ds$. Therefore, the net flux though S is conserved.

To complete the description of the frozen-in-flux condition, the conservation of field lines must also be addressed. This is also a straightforward application of equation 1.6 with the inclusion of the equation for mass conservation. The equation for

conservation of mass is of the form

$$-\rho\vec{\bigtriangledown}\cdot\vec{v}=\frac{\partial\rho}{\partial t}+\vec{v}\cdot\vec{\bigtriangledown}\rho \quad . \tag{1.11}$$

The combination of the two equations yields

$$\frac{D}{Dt}(\frac{\vec{B}}{\rho})=(\frac{\vec{B}}{\rho}\cdot\vec{\bigtriangledown})\vec{v} \tag{1.12}$$

It should be noted that $\frac{D}{Dt}$ is the advective derivative equal to $\frac{\partial}{\partial t}+\vec{v}\cdot\bigtriangledown$.

Therefore, any two plasma elements initially on the same field line will remain on that field line for all time. They will maintain a separation proportional to $\frac{\vec{B}}{\rho}$. This relationship permitted derivation of the previous statement that indicates that plasma elements initially at neighboring points on a field line will remain on that field line for all time. The condition for frozen-in-flux is thus the requirement that the velocity of the magnetic field lines is equal to the plasma velocity [14].

As will become apparent in Chapters 3 and 4, the distinction between a bundle of field lines and observed coronal structures, called coronal loops, is important and often not well differentiated. In this thesis a flux tube is a bundle of field lines that is topologically coherent, where the tube maintains constant flux through its cross-section. A coronal loop is defined to be an observationally distinct feature that is nearly semi-circular. In solar physics the relationship between flux tubes and coronal loops has not been well-established.

The previous description of the interdependence of the plasma and the magnetic field does not indicate what determines which influence, plasma or magnetic, is dominant. The use of the descriptive parameter plasma β, a ratio of the thermal plasma pressure (gas pressure), p_g, and the magnetic pressure, p_m, is used to describe the case in which the plasma is in charge, so to speak, or the magnetic field is dominant.

It is important to note that the previous discussion on frozen-in-flux only shows that the structure of the corona is defined by the field. The mechanism driving the field and plasma motions is described in the following discussion.

The magnetic field exerts a force, the Lorenz force, on the plasma via

$$\vec{F} = q(\vec{E} + \vec{v} \times \vec{B}) \quad , \tag{1.13}$$

where q is the charge of the particle, $\vec{E}$ the electric field, $\vec{v}$ the particle velocity and $\vec{B}$ is the magnetic induction. As a consequence of this force, particles are guided along the field. The parameter β is formally written as

$$\beta = \frac{p_g}{p_m} = \frac{8\pi(2n_e k_b T)}{B^2} \quad . \tag{1.14}$$

In equation 1.12, n_e stands for the electron density, k_b is Boltzmann's constant, T is the temperature, and B^2 is the square of the magnetic induction. In the solar corona below approximately 100 Mm above the solar photosphere, the plasma β is expected to be less than unity (Choudhuri (1998) [14]). Near the photosphere and above 100 Mm it is greater than unity. The fact that the magnetic pressure is greater than the gas pressure in the corona, required for $\beta < 1$, indicates that the magnetic field inhibits plasma motion perpendicular to the direction of the magnetic field. Of course, for $\beta > 1$ the plasma pressure drives the field. So for the corona it is readily seen that the ionized gas along individual flux elements is essentially shielded from any interaction with plasma along other field lines. It was this fact that led Vaiana and Rosner to develop the "mini atmospheres" description of the corona [15].

The Potential Magnetic Field Corona

With the introduction of the concept of the "mini atmosphere" it is now appro-

priate to define the topology of the corona using the potential field extrapolation. A potential field is one that satisfies $\bigtriangledown \times \vec{B} = 0$. A general description of this can be found in Priest & Forbes (2000) [16], and the following derivation was presented as part of a project for a magneto-hydrodynamics (MHD) course offered at Montana State University (Longcope & Martens (2003) [17]).

One of the first potential field approximations was performed by Rust [18]. He showed that the magnetic fields above the photosphere were similar to those derived from potential field theory. Newkirk [19] claimed that a potential dipole model was capable of crudely representing the magnetic field above active regions. Since these initial efforts many applications of the potential field model of the coronal magnetic field have been used to describe a wide array of coronal features (e.g. Rudenko [20], Wang [21], or Schatten [22]).

Magnetographs are now used to map the magnetic fields that are ubiquitous in the photosphere. The MDI instrument on SoHO is such a device. The Zeeman splitting is measured from the filtergram components taken separately in right-hand and left-hand circularly polarized light. The uncertainty per pixel in the measurement of the line of sight component of the field for a two-minute exposure is approximately $\pm$ 20 Gauss, with typical values for flux emergence regions of magnitude 100 Gauss.

We selected a full disk MDI magnetogram taken on 13 September 2001 to demonstrate the usefulness of the potential field approximation. A 256 x 256 pixel area was chosen that enclosed a region with both positive and negative flux. A magnetogram of this region is shown in figure 1.4.

In selecting a data set it was necessary we require the active region be close to disk center so that the signal along the line-of-sight was essentially the z component of the magnetic field. If the region is far from disk center the signal is a mixture of all of the components of the field, an added problem we avoided. The 256 square image selected

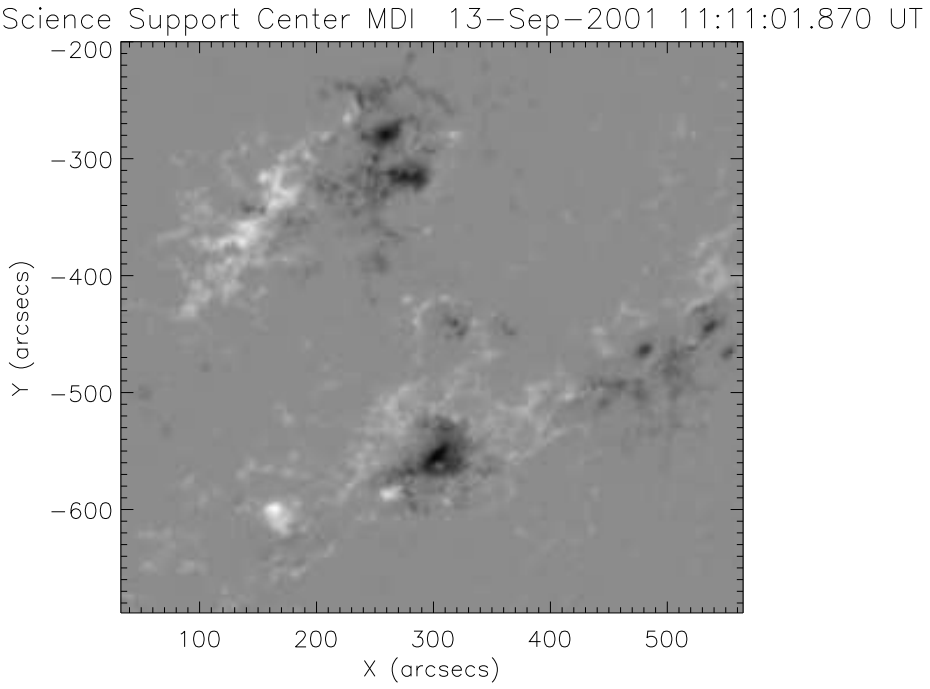

Figure 1.4: MDI magnetogram of Active Regions NOAA 9610 (top) and NOAA active region 9608 (bottom).

for study was converted to an array, and the Fourier transform of this array generated the Fourier expansion coefficients necessary to construct the $\vec{B_x}$ and $\vec{B_y}$ components of $\vec{B}$. The Fast Fourier Transform method determines the frequency spectra of the signal. In the case of the magnetogram, this spectrum is in wave numbers. These wave numbers correspond to the Fourier modes of the magnetic field. The inverse transform, where b_k is the expansion coefficient for every grid point in the array, is defined by

$$b_k = \sum_k B_z exp[i\vec{k} \cdot \vec{x}] \quad . \tag{1.15}$$

Here k is the wavenumber, and x is the coordinate vector (which only consists of the

x and y components and z is treated separately). The forward transform is then,

$$B_x = \sum_k \frac{ik_x}{|\vec{k}|} \cdot b_k \cdot \exp[-i\vec{k} \cdot \vec{x} - |\vec{k}| \cdot z] \quad , \tag{1.16}$$

where an exponential decay term is included to insure that the field meets the boundary conditions at infinity, specifically that $B \rightarrow 0$ as $z \rightarrow \infty$ required to satisfy $\bigtriangledown^2 \chi = 0$. Here χ is the scalar potential for the magnetic induction $\vec{B}$. An identical equation in y is used to calculate the component of the field in that direction. The z component of the field is calculated in a similar way, by performing the Fourier transform of the expansion coefficients multiplied by the exponential decay term. Having determined the components for the field, a 2-dimensional plot of the field lines is shown in Figure 1.5 for the field at the photosphere ($z = 0$). This is a reasonable approximation for the geometry of the solar magnetic field when compared

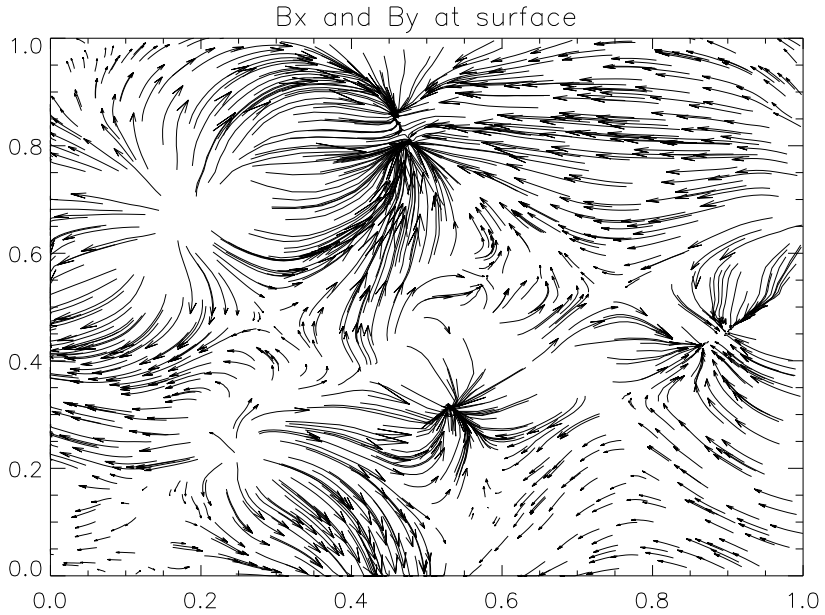

Figure 1.5: Potential field calculation for MDI magnetogram shown in Figure 1.4.

to observations of the structures observed in EUV images.

The remainder of this thesis will focus on the coronal magnetic field and the plasma constrained to move along it as prescribed by the topology and evolution of the magnetic field. This situation is the low plasma β regime, and the magnetic pressure thus dominates the plasma or gas pressure.

The Hydrostatic Atmosphere

With the basic characterization of the magnetic field in place and the summarization of the plasma magnetic field coupling complete, it is now necessary to describe the pressure, density, and other relevant properties of the plasma. It is the hydrostatic formalism which allows a description of the variation of the density and pressure with altitude. In the simple case of the atmosphere of the earth, a general example of the stratification of the atmosphere with altitude is noticed by anyone who has ever climbed a tall mountain. Near the base the air is thick and breathing is not difficult, yet once at the summit of the mountain the climber will notice that it is much harder to intake sufficient oxygen, and consequently breathes faster to take in more air to maintain the level of O_2 in the blood. This is the result of the gravitational stratification of the atmosphere; there is less air at higher altitudes. If the pressure of the gas is only balanced by the force of gravity, it is typical to refer to this situation as gravitationally stratified or in hydrostatic equilibrium. The force due to gravity is directed radially toward the center of mass. Accordingly, the potential energy associated with an object above the surface of a much more massive object, e.g. the sun, has potential energy, U_g, defined by the relation

$$U_g = -\frac{GM_{sun}m}{r} \quad . \tag{1.17}$$

Here m is the mass of the smaller object, G is the universal gravitational constant ($G = 6.67 \times 10^{-8}$ dynes cm^2 g^{-2}), and M_{sun} is the solar mass with r the length of the radial vector from the center of mass of the sun to the location of the object. The force on the mass due to gravitational attraction is

$$\vec{F} = m\vec{a} = m\vec{g}_{sun} \quad , \tag{1.18}$$

and $\vec{g_{sun}}$ is the solar gravitational constant equal to 274 $\frac{\mathrm{m}}{\mathrm{s}^2}$. Pressure is the force per unit area, $p = \frac{F}{dA}$. The gradient of the pressure, $\frac{dp}{dr}$, must then have the dimensions of a force per unit volume. This can be readily seen from the equation

$$\frac{dp}{dr} = \frac{F}{dA \times dr} = \frac{F}{dV} \quad . \tag{1.19}$$

This is simply the product of the force and volumetric particle density (cm^{-3}),

$$\frac{dp}{dr} = F \times n \quad . \tag{1.20}$$

The pressure equilibrium or momentum equation in hydrostatics is simply the product of the force per particle and the density. Substituting all known variables, this becomes

$$\frac{dP}{dr}(r) = -mn(r)g_{sun} \quad . \tag{1.21}$$

The mass of the particle may be rewritten in terms of the variables ρ, mass density, and n, the particle density. Then $m = \frac{\rho}{n}$, and in the solar atmosphere the total mass density is equal to the sum of the electron density, n_e, and the ion density, n_i. Consequentially, ρ can be written

$$\rho = mn = m_e n_e + m_i n_i \approx \mu m_H n_e \quad , \tag{1.22}$$

with m_H representing the mass of atomic hydrogen. Here it has been assumed that the gas is essentially charge neutral per unit volume, and it is therefore valid to assume the $n_p \approx n_e \approx n_i$. The proton density, n_p, is basically equal to the ion density and it is not customary to include additional atomic masses in these calculations, other than for helium, as the relative abundance of these heavier ions is much lower than that of hydrogen and helium. The mean molecular weight of the plasma, μ, is defined to be the sum of the molecular weight for each ion, weighted with the appropriate ratio of hydrogen to helium. For the solar corona the ratio of hydrogen to helium is 10:1, and so μ becomes

$$\mu = \frac{10 \times 1(^1H) + 1 \times 4(^4He)}{n_p + n_{He} + n_e} \quad . \tag{1.23}$$

From this calculation for the molecular weight, $\mu \approx 0.6$ (Mariska 1992) [23]. The momentum equation, Equation 1.22, can now be written using the coronal electron density as

$$\frac{dP}{dr}(r) = -m_H \mu n_e g_{sun} \quad . \tag{1.24}$$

In order to solve this equation, the development of the relation between the density and pressure into the thermodynamic *equation of state* must be completed. For the solar atmosphere, the ideal gas law is sufficient, and $p = nk_BT$. The plasma pressure in the corona is the sum of the ion and electron gas pressures, and this is equal to

$$p(h) = 2n_e(h)k_BT_e(h) \quad . \tag{1.25}$$

The equation of state may be solved for the electron density and substituted into the momentum equation. Performing the substitution, the momentum equation is now

$$\frac{dp}{dh}(h) = -p(h)\frac{\mu m_H g_{sun}}{2k_BT_e(h)} \quad . \tag{1.26}$$

Assuming T_e is constant, one may integrate equation 1.27 to find that the pressure of the coronal atmosphere as a function of height above the solar photosphere is

$$p(h) = p(0)\exp[-\frac{\mu m_H g_{sun}}{2k_B T_e}h] \quad . \tag{1.27}$$

The constants contained in the exponential are generally grouped to form the *hydrostatic pressure scale height*, $\lambda_p(T_e)$. The pressure scale height for the solar corona is

$$\lambda_p(T_e) = \frac{2k_B T_e}{\mu m_H g_{sun}} \approx 4.67 \times 10^9 (\frac{T_e}{1\mathrm{MK}})cm \quad . \tag{1.28}$$

It should be clear that the hydrostatic scale height is dependent on the temperature of the plasma along the magnetic field line.

A variant of the pressure scale height is the emission measure scale height. The emission measure is define in Mariska [23] to be the value of the integral

$$\int_R n_e^2 dV \quad , \tag{1.29}$$

for the emitting volume. The equation of state can be solved for density instead of pressure, and a scale height for the emission measure can be found. It is simply $\frac{1}{2}$ the pressure scale height. The importance of this parameter will become apparent in a later section. However, the theoretical value for the emission measure scale height will be compared to the exponent in an actual fit to observations. This is a direct measure of whether the corona is in hydrostatic equilibrium, a result that is important in coronal modeling.

In order to qualify the description of the plasma as being in hydrostatic equilibrium, the conditions for equilibrium must be established. The momentum equation

for plasma along a magnetic field line may be written

$$\rho\frac{\partial v}{\partial t} + \rho v\frac{\partial v}{\partial s} = -\frac{dP}{ds} + \rho g_{\|} \quad . \tag{1.30}$$

Here ρ is the mass density, s is distance along the loop, v is the velocity, P is the pressure, and $g_{\|}$ is the component of gravity acting parallel to the loop. The pressure may be written as $P = \rho c_s^2$, where c_s is the sound speed and $c_s \approx 200\frac{km}{s}$ for the corona. For hydrostatic equilibrium to exist the terms on the left hand side of the momentum equation must be much smaller than those on the right hand side. It is often required that the left hand side be equal to zero but this is not strictly necessary for equilibrium to be maintained. Rewriting 1.31 in terms of the units of the variables we have

$$\frac{\rho v}{\tau} + \frac{\rho v^2}{l} = \frac{\rho c_s^2}{l} + \rho g_{\|} \quad . \tag{1.31}$$

In 1.31, τ is a time and l is a characteristic length. It is obvious that if $v^2 \ll c_s^2$ and $\tau > \tau_d = \frac{l}{c_s}$ then the first term on the right hand side of equation 1.31 is dominant. The plasma along the field line will remain in hydrostatic equilibrium, the variation in pressure with altitude will be balanced by gravity, and flows with velocities much smaller than the sound speed will not perturb this equilibrium. Additionally, for changes to the loop that occur over time scales longer than the dynamic time, τ_d, the loop will have time to distribute the effect of the change over the loop, thus maintaining its equilibrium state.

Summary

In this chapter, the solar corona has been characterized in terms of its plasma and magnetic field properties. The coronal plasma β, a measure of the ratio of the gas pressure to the magnetic pressure, is less than unity. For example, a "typical" AR

has a mean temperature of 3 MK, density of 3×10^9 cm^{-3}, and magnetic induction of $\approx$ 10G. Using equation 1.12, one finds $\beta = 2 \times 10^{-3}$. This indicates that the magnetic field is dominating the motions of the plasma, and the plasma is only allowed one degree of freedom: motion parallel to the magnetic field. The guiding center is simply the name for the approximate center about which the charged particles spiral while moving along the field. This point is only mentioned for completeness, and the subject of guiding center motion is a topic for another day.

The solar photospheric magnetic field defines the structure of the solar corona. The plasma at the footpoints of the emergent magnetic flux drags the field along and forces the coronal field to store the transferred magnetic energy. When the magnetic field becomes unstable to further perturbations, the field may re-organize. It is believed to be a source of energy for heating the corona to millions of degrees Kelvin, and a source for solar flares (Priest and Forbes (2000) [16]).

The plasma in a flux tube is stratified according to the temperature, base pressure or density, and, if applicable, dynamics. In the instance of a hydrostatic atmosphere the pressure exerted on the gas is balanced only by gravity. In the slow evolution of the heating rate and mass loss to the chromosphere, and save any dynamic events, the plasma along a coronal flux tube will settle to a hydrostatic equilibrium. Sometimes this plasma is at sufficient density and temperature to be observed in the EUV. The distinction between flux tubes and coronal loops is often not carefully delineated. In this thesis, a coronal loop is a resolved structure in the solar corona which often appears to be nearly semi-circular. The unresolved AR corona refers to emission above the instrumental noise threshold.

Hydrostatic equilibrium is maintained when the dynamic time, equal to a characteristic length divided by the sound speed, is shorter than the time in which changes to the state of the plasma occur. For coronal loops with characteristic lengths of tens

of Mm, the dynamic time is of order a few minutes. Observations presented in this thesis have no observed increases in intensity over such a short time scale. The other requirement for hydrostatic equilibrium is that the velocity of the plasma along the loop be much smaller than the sound speed. Indications from the measurement of the centroid wavelengths in our observation to not provide any evidence for large velocities, $v > 100\frac{km}{s}$, nor are there any local intensity enhancements that propagate along the loop, a possible indication of laminar flow. Ionization equilibrium is maintained if the electron-ion collisions are balanced by radiative and dielectronic recombination. For ions at the typical coronal temperatures (1 MK), this is maintained for the low densities associated with resolved coronal loops and the unresolved background. It is most likely violated in small volumes near the location of a solar flare, a topic outside the scope of this thesis. It is assumed that ionization equilibrium is maintained for structures studied herein, and ionization processes are discussed further in Chapter 2. Radiative and conductive cooling times are typically on the order of several tens of minutes and a heating mechanism must maintain the temperature of the plasma within a loop's cross section and sustain the temperature along the length to maintain LTE.

In Chapter 3, observations of the corona of an AR are used to determine whether the emission decrease can be modeled by the hydrostatic formalism introduced in the previous section. No model of the heating mechanism for the results of Chapter 3 are presented as they are beyond the scope of this thesis.

All of the previous research performed on data collected for coronal active regions primarily focuses on coronal loops and the other resolved features (e.g. the review of Trimble and Aschwanden (2004) [24]). The temperature, density and modeling of coronal loops has been the pursuit of many researchers and a volume of work is available on this topics. Winebarger, Warren, and Seaton (2003) [25] study the

emission along coronal loops and provide a model for dynamic cooling loops. Schmelz et al. [5] provide estimates of the amount of emission as a function of temperature for loops using spectral line intensities, and Testa, Peres, and Reale (2003) investigate loops imaged by TRACE in an effort to determine temperature and density for these AR structures. Aschwanden, Nightengale and Alexander (2000a.) [26] study the characteristics of resolved coronal loops using a narrow band instrument filter ratio to determine the temperature along the loops, and Lenz et al. (1999a) [27] analyze numerous TRACE loops to determine the temperature and density of resolved loops in ARs.

This thesis will focus on the unresolved AR corona and after a detailed investigation of the physical characteristics of the unresolved corona, the implications for coronal loop studies will be presented. We believe that this is the first study of coronal ARs where the primary focus is the unresolved (background) emission. We will present a physical model for the unresolved corona based on observations. Using the results for the unresolved corona, an examination of coronal loops will be offered that incorporates a background subtraction method based on a physical model of the emission of the unresolved corona. This is the first background subtraction routine we know of that uses a physical model of the background emission to remove the line-of-sight contribution from the AR observations. We believe this permits a better analysis of the emission from resolved structures.

CHAPTER 2

OBSERVING THE SOLAR ATMOSPHERE

Early observations of the corona demonstrated the variability of the solar atmosphere, and this was later found to directly correlate with the 11 year solar cycle. A spectrum was first observed by Sir Isaac Newton which led to the development of the science of spectroscopy and was first applied to the solar spectrum in 1814. Josef von Fraunhofer, a German physicist, observed absorption lines characteristic of elements in the solar atmosphere absorbing the radiation emitted from below, producing 'dark' lines in the solar spectrum. It was from these early pioneers that the science of solar coronal physics was born.

Figure 2.1: This is an image of *Skylab*, The image was taken from a crew transport module and is courtesy of NASA, http://mix.msfc.nasa.gov /IMAGES/MEDIUM/

As humans ventured to altitudes above the earth's atmosphere, observations using a myriad of different telescope designs over much of the electromagnetic spectrum were

made. The first rocket launches with telescopic payloads provided images of the solar corona, making it clear that the corona was a hot tenuous gas. On May 14, 1973, the highly successful *Skylab* mission was launched into orbit. This 'space station' was operational for 251 days. It had a mass of a whopping 96,000 kg and was launched by a Saturn 5b rocket to an altitude of 435 km. Three crews of astronauts carried out experiments; in particular they used the Apollo Telescope Mount (ATM), located at one end of the space station, which contained eight different observing instruments capable of collecting solar data over the wavelength range 2 Å - 7000 Å . Through the use of photographic film some 150,000 images were taken during the operational lifetime of the ATM. The S-052 instrument was an X-ray spectrograph, and the S-056 telescope was an X-ray imaging device. In addition to these two instruments, ATM had an ultraviolet spectrograph and an EUV spectroheliograph, S-082B and S-082A, respectively [7]. In combination these instruments provided a view of the solar corona that spanned a temperature range of over 5 million K, a first for solar astrophysics. An image of a flare captured by the S-056 device is shown in Figure 2.2, and the Skylab module is shown just prior to de-orbit in Figure 2.1.

The instruments onboard *Skylab* marked a turning point in the history of coronal observations. As higher resolution platforms were launched into space, and with the advent of Charge Coupled Device (CCD) technology, long duration missions were possible that further expanded the view of the corona. There is now a literal fleet of satellite observatories for solar investigations. These include SoHO, the Transition Region and Coronal Explorer (TRACE), and the Reuven Ramaty High Energy Solar Spectroscopic Imager (RHESSI) [28], among others. Numerous other platforms have contributed much to solar physics, most notably being the *Yohkoh* satellite, a Japanese (ISAS), NASA, and European Space Agency (ESA) collaboration.

The next generation of telescopes is most promising, with several large platforms

Figure 2.2: This solar flare was observed by S-056 X-ray telescope on *Skylab*, courtesy of NASA, http://mix.msfc.nasa.gov/IMAGES/MEDIUM/

currently in development. These include the Solar Dynamics Observatory (SDO), a NASA Living with a Star (LWS) mission[1], and Solar-B, a Solar and Terrestrial Probe class mission (ISAS, ESA, NASA all participating). Numerous instruments will be part of each satellite, and the combination of all the observations promises a more detailed investigation of the solar corona and the mechanisms associated with its heating than available previously. In addition to these multi-million dollar missions, on-going research at the university level is developing the next generation of solar observing techniques. Most notably, the rocket programs of Dr. Roger Thomas at NASA's Goddard Space Flight Center (GSFC) and Dr. Charles Kankelborg at Montana State University (MSU) are developing the most sophisticated EUV and UV spectrometers to date. The development of these new observing methods increase the understanding of coronal physics started by those first eclipse observers many years ago.

[1]http://lws.gsfc.nasa.gov/

Emission Line Spectroscopy

Most of what is known to date about the corona and the underlying Transition Region (TR) and chromosphere is based on the analyses of data collected by UV, EUV and X-ray spectrometers. As such, it is important to understand the processes involved in the formation of emission line spectra. This section will introduce optically-thin emission line formation and the basic assumptions made when characterizing emission from the spectral lines. A development of the methods for inference of physical properties of the emitting plasma will also be introduced. As was detailed in the previous chapter, the corona is a highly rarefied ionized gas. If the temperature, density, and velocity are known as a function of position and time, then the thermodynamic and kinematic states of the plasma are specified. These properties can be determined through the understanding of the physical processes that are present in the corona.

Within the corona, ionization occurs as the result of two main processes, autoionization and electron impact ionization. By far the dominant process for the non-flaring corona, electron impact (collisional) ionization is the means by which the majority of the ionization states in the solar corona are formed [23]. Collisional excitation is a straightforward process. The electrons and ions have large kinetic energies from the random motions of the plasma as a result of the high temperatures of the plasma. Many electrons have enough energy associated with their motions to deflect bound electrons away from the host atom in what is generally called an (e, 2e) reaction (Bransden (2003) [29]).

Autoionization occurs when a doubly excited state of an atom lies in the ground state continuum. The atom loses an electron and transitions to a lower energy state. This autoionization process is radiationless and is evidenced by the associated absorption features present in observations. However, this process a minor contributor to the

total ionization rates in the physical regime under consideration and can consequently be neglected (Mariska (1992) [23])).

There is yet another method for ionization of the elements comprising the corona, namely photoionization. Through this process an atom absorbs a photon, and this excites a bound electron to an energy level higher than the ionization energy, leaving the atom ionized. This process is unimportant in the less active domains of the corona due to the weak radiation field, but may play a role for flaring ARs.

We do not consider other sources of radiation, such as free-free and free-bound radiation, because they are not important processes for the non-flaring active region corona. A brief description of the processes of emission line formation, excitation opacity, and elemental abundances with regard to the non-flaring coronal plasma is presented in the follow sections (for a complete description of the mathematical formalism for these subjects please refer to the classic texts, including Athay [30], Mariska[23], as well as numerous others).

Introduction to Radiation

The measure of impediments to the transmission of radiation is called the opacity. Opacity is simply the inverse of transmittance. An example of an optically thick fluid is the Mississippi River. Light is unable to penetrate to any appreciable depth due to absorption and scattering from the near innumerable set of particulates contained in the water. Often for the solar corona the assumption is made that the plasma is optically thin; it will allow radiation to travel through the entire coronal volume without being scattered or absorbed. Simply put, opacity is the extent to which a medium is opaque to electromagnetic radiation.

For every atomic species composing the coronal plasma there are many possible bound energy states. Atoms may decay into a less excited energy state by spontaneous or stimulated emission. The probability of these transitions is described by the

Einstein rate coefficients. For spontaneous transitions A_{ij} represents the probability rate for excitation from level i to a higher level j, and A_{ji} represents the reverse process of emission. Stimulated emission has similar coefficients for emission and absorption, namely B_{ji} and B_{ij} respectively. For optically thin plasmas it is typical to define a collision coefficient, C_{ij}, which describes the rate transitions occur from i to j.

The difference in energy between the upper state j and the lower state i determines the wavelength of the emitted radiation. Most often the selection rules for electric dipole transitions and knowledge of the transition rates are all that are needed to determine the populations of available states. Given the populations of the various states and the decay rate for radiation production, the total expected intensities for emission lines may be calculated. Occasionally the electric dipole approximation is insufficient. EUV 'forbidden' lines are produced during transitions with such small probability of occurrence that they do not have sufficient time to form between collisions (Bransden (2003) [29]). However, for the rarefied plasma of the corona, the density is sufficiently low that collisions occur infrequently enough to permit such forbidden transitions; it is thus necessary to include the magnetic dipole, electric quadrapole, etc. terms in the expansion of the quantum mechanics operator describing atomic transitions. This is known to be of the form

$$M_{ba} = \sum_{i=1}^{N} \langle \psi_b | \exp(i\vec{k} \cdot \vec{r}) \hat{\varepsilon} \cdot \vec{\bigtriangledown}_{\vec{r}_i} | \psi_a \rangle \quad . \tag{2.1}$$

In equation 2.1, $\vec{k}$ is the propagation vector $\hat{\varepsilon}$ is the polarization unit vector and ψ_a and ψ_B are the approximate eigenfunctions for the unperturbed N-electron Hamiltonian. The exponential term in equation 2.1 is typically called the retardation factor, and this is, in general, set to unity when the dipole approximation is permitted. The dipole approximation is valid for $\lambda \gg r_a$, where r_a is the radius of the atom or when

the density of the plasma is so low that the frequency of collisions permits formation of the forbidden emission lines [29].

Emission lines are created when collisionally or radiatively excited states decay to lower energy states. These transitions are governed by the laws of statistical and quantum mechanics as discussed previously. The expected emission lines of the corona are calculated using the ionization balance equations that describe the balance between electron impact ionizations and dielectronic and radiative recombinations, the abundances of the elements comprising the plasma relative to hydrogen, and the formalisms of quantum mechanics. Mazzota et al. [4] have performed the ionization balance calculations for the major elements of the corona, and the abundance calculations of Meyer [1] are generally used in solar research. Application of all these equations allows the electron density as well as the flux of any emission line to be calculated. Table 2.1 is a listing of the coronal abundances used in this study.

Element	Atomic Number (Z)	Coronal Abundance (log_A)
H	1	12.0
He	2	11.0
C	6	8.37
N	7	7.59
O	8	8.39
Ne	10	7.55
Na	11	6.44
Mg	12	6.57
Al	13	6.44
Si	14	7.59
S	16	6.94
Ar	18	6.33
Ca	20	6.47
Fe	26	7.59
Ni	28	6.33

Table 2.1: Elemental relative abundances for the solar corona (Meyer (1985) [1])

Solar coronal EUV observations are performed using two methods. These are

spectroscopy and finite-passband imaging. Finite-passband imaging is also of two flavors, either narrow-band (normally ten or so angstroms in width) or broad-band imaging. In the following sections the two primary instruments used in this thesis are discussed in detail. These are the Coronal Diagnostic Spectrometer (CDS) and the narrow-band imager TRACE.

The Coronal Diagnostic Spectrometer

The CDS instrument is designed to investigate the solar coronal plasma thermodynamics. This is accomplished by analysis of data collected from the observations of EUV emission lines. The performance requirements of this instrument specifically includes five main goals.

1. The wavelength coverage should include lines formed from ions existing in the temperature range of $10^4 - 10^7$ K. For this purpose the wavelength range of 150-800 Å was chosen.

2. The spectral resolution of the instruments should permit lines of interest to be separated from one another, and most lines of interest can be resolved with a spectral resolution of $\delta\lambda = 0.3$ Å.

3. The field-of-view of the instrument must be able to cover ARs, prominences and large portions of coronal holes or the quiet sun; it must also be able to change targets so that different areas of interest may be investigated.

4. It must have moderate spatial resolution, sufficient for the smaller phenomena of the atmosphere, i.e $1''$pixels.

5. It must posses a temporal resolution as high as feasible based on technological capability, cost, and schedule. At the time of the definition of the science

requirements for the instruments it was hoped that exposures of one second would be possible.

For the most part, these pre-launch science requirements were met. The capabilities of the instrument will be outlined in the subsequent section.

	NIS	GIS
Aperture	34.3 cm^2 per grating	47 cm^2
Wavelength Ranges	308 - 381 Å 513 - 633Å	151 - 221Å 256 - 338Å
		393 - 493Å 656 - 785Å
Prime Slits	$2 \times 240''$, $4 \times 240''$,	$2 \times 2''$, $4 \times 4''$,
	$90 \times 240''$	$8 \times 50''$
Grating Ruling	2400 & 4000 lines/mm	1000 lines/mm
Slit-grating Distance	736.5 mm	NA
Grating-detector Distance	744.6 mm	NA
Rowland Circle Radius	NA	750 mm

Table 2.2: Characteristics of the CDS instruments (Harrison et al. [2]).

Optical Design

It was determined early in the engineering development of the telescope that it was technologically impossible to meet all of the science goals with a single spectrometer. This was primarily due to the technological limitations associated with observing over such a wide range in wavelength, and so the telescope actually consists of two separate devices, the Grazing Incidence Spectrometer (GIS) and the stigmatic imaging device, the Normal Incidence Spectrometer (NIS). The GIS instrument has four wavelength ranges, and these are listed in Table 2.2. It was not used in this study and will not be detailed further.

Telescope

The optical layout for CDS is shown in Figure 2.3. Using a grazing incidence Wolter-Schwarzschild Type 2 telescope design, incident flux is directed onto a slit via

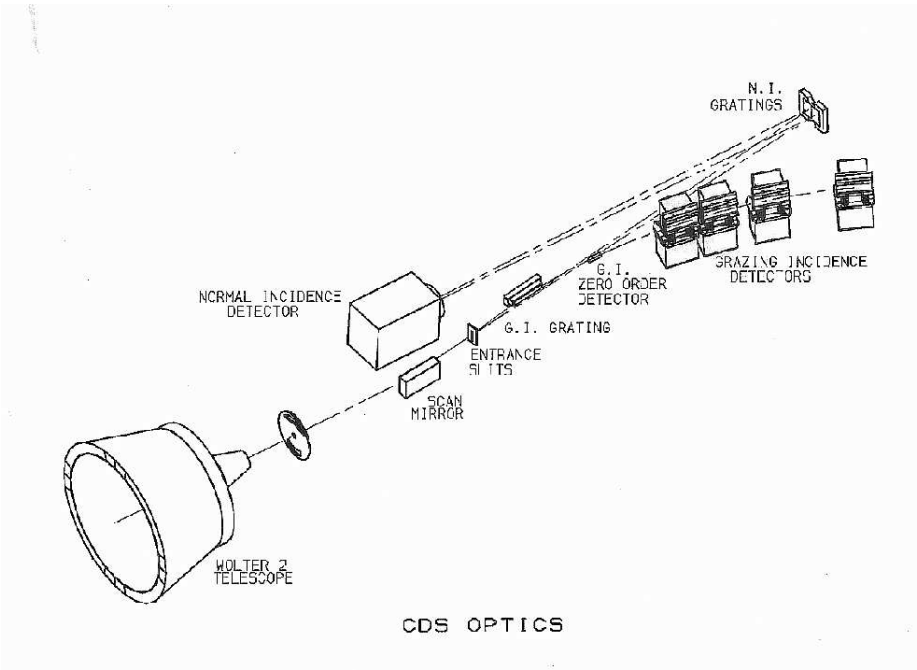

Figure 2.3: This is a schematic of the CDS optical layout. Image provided courtesy of CDS science team.

reflection off paraboloidal and then hyperboloidal surfaces. The mirror is zerodur, a glass ceramic with a very high viscosity and which is stable to thermal variations. It is highly polished to a surface finish of less than 10 Å and coated with gold to increase the reflectivity. The spatial resolution of this telescope is defined by the full width at half maximum (FWHM) of the so-called point spread function (PSF). The PSF is simply the spread in an image of a point source at best focus. The smaller the FWHM of the PSF for the telescope, the higher the resolution of the telescope. The PSF for the mirror was determined prior to launch and is shown in Figure 2 of Harrison et al. [2]. This plot shows a pronounced asymmetry in the direction perpendicular to the dispersion direction. This PSF of the CDS instrument is one of the major limitations of the telescope. It is nearly 2″ FWHM, and with pixels 21 μm on a side, the PSF is larger than the pixel, an obvious deterrent to well-resolved images.

Scanning Mirror and Slits

The beam converging from the telescope is reflected at an angle of incidence/reflection of 5°. Rotation of the mirror allows a region of interest be scanned across the spectrometer slit by stepping the mirror tilt motor. Each move of the stepper motor corresponds to a 2″ move on the sun.

Both the GIS and NIS instruments have three slits for dispersion of the beam. The NIS slits are 25 μm wide for the 2″ slit and 50 μm wide for the 4″ slit. These were constructed from nickel mounted on a copper support, and then this was attached using an epoxy to the aluminum alloy support frame. Each slit has a length of 240″ with reference to distance on the sun. One final slit is available to NIS, the 90″ × 240″ slit, and is used for view-finder images of the strongest spectral lines.

The Normal Incidence Spectrometer

Radiation passing through the entrance slit strikes the two toroidal gratings at an average angle of 7° and is dispersed onto a 2-dimensional imaging detector. The toroidal gratings are used because they produce images that are essentially free from astigmatism. This in turn results in images with moderate spatial resolution and a high spectral resolution. The EUV reflectivity of the mirror coating is a function of wavelength, and this limits the spectral coverage to above 300 Å. The remaining characteristics of the NIS instrument are listed in Table 2.2. For additional details involving this instrument please refer to the engineering paper on CDS [2].

Principle Emission Lines of the NIS Device

Within the spectral passbands where the NIS instrument is sensitive, there are a number of different emission lines with sufficient intensity to permit measurement above the continuum. In addition, the ions emitting in the wavelength ranges for NIS are formed over temperature ranges found in the solar corona. These emission lines

form a set that contains both density sensitive and temperature sensitive line pairs. Density sensitive line pairs are two emission lines from the same ionization stage, but one line is an electric dipole transition and the other is a transition forbidden in the electric dipole approximation yet allowed when the magnetic dipole and electric quadrapole terms are included. This fact that the 'forbidden' line is observed is an indication of the plasma density, and the ratio of the allowed to forbidden intensities specifies the density. These forbidden lines are formed via transitions governed by the higher order terms in the expansion of equation 2.1.

Two electric dipole transition emission lines from different ionization stages of the same element can help specify the temperature. The ratio of the higher ionization stage emission line intensity to that of the lower ionization stage will constrain the temperature as a function of density. This is possible because the two different ionization stages, which exist over a narrow temperature range, have temperature of formation curves that overlap. These ionization curves may be used to construct a ratio of the intensities of the lines formed from the two ionization stages and the value of the ratio is an indication of the temperature of the plasma. The principle emission lines used in this thesis are given in Table 2.3. The ionization curves for Fe VII - Fe XVIII are shown in Figure 2.4. A sample spectrum for a fraction of the wavelength ranges used in this study is shown in Figures 2.5 and 2.6.

Ion	Log_{10} Peak Formation Temperature (K)	Wavelength (Å)	Intensity (ergs $cm^{-2}sr^{-1}s^{-1}$)
He I	4.5	584.33	2.74e+5
O III	5.0	599.59	1.76e+5
O IV	5.2	554.08	1.25e+5
O IV	5.2	554.52	3.17e+5
O V	5.4	629.73	4.31e+5
Ne VI	5.6	562.80	8.66e+3
Ca X	5.8	557.77	1.73e+2
Si IX	6.0	345.12	1.60e+3
Mg IX	6.0	368.06	5.27e+3
Si X	6.2	347.41	1.35e+3
Si X	6.2	356.03	1.87e+3
Mg X	6.2	624.94	9.84e+3
Fe X	6.0	345.72	9.77e+2
Fe XII	6.2	364.47	2.13e+3
Fe XIII	6.2	320.80	2.21e+3
Fe XIII	6.2	348.18	1.16e+3
Si XII	6.3	520.67	5.16e+4
Fe XIV	6.3	334.17	5.71e+3
Fe XIV	6.3	353.84	3.24e+3
Fe XV	6.4	327.02	1.70e+3
Fe XVI	6.6	335.40	3.91e+5
Fe XVI	6.6	360.76	1.87e+5

Table 2.3: Principle emission lines of the NIS spectrometer.

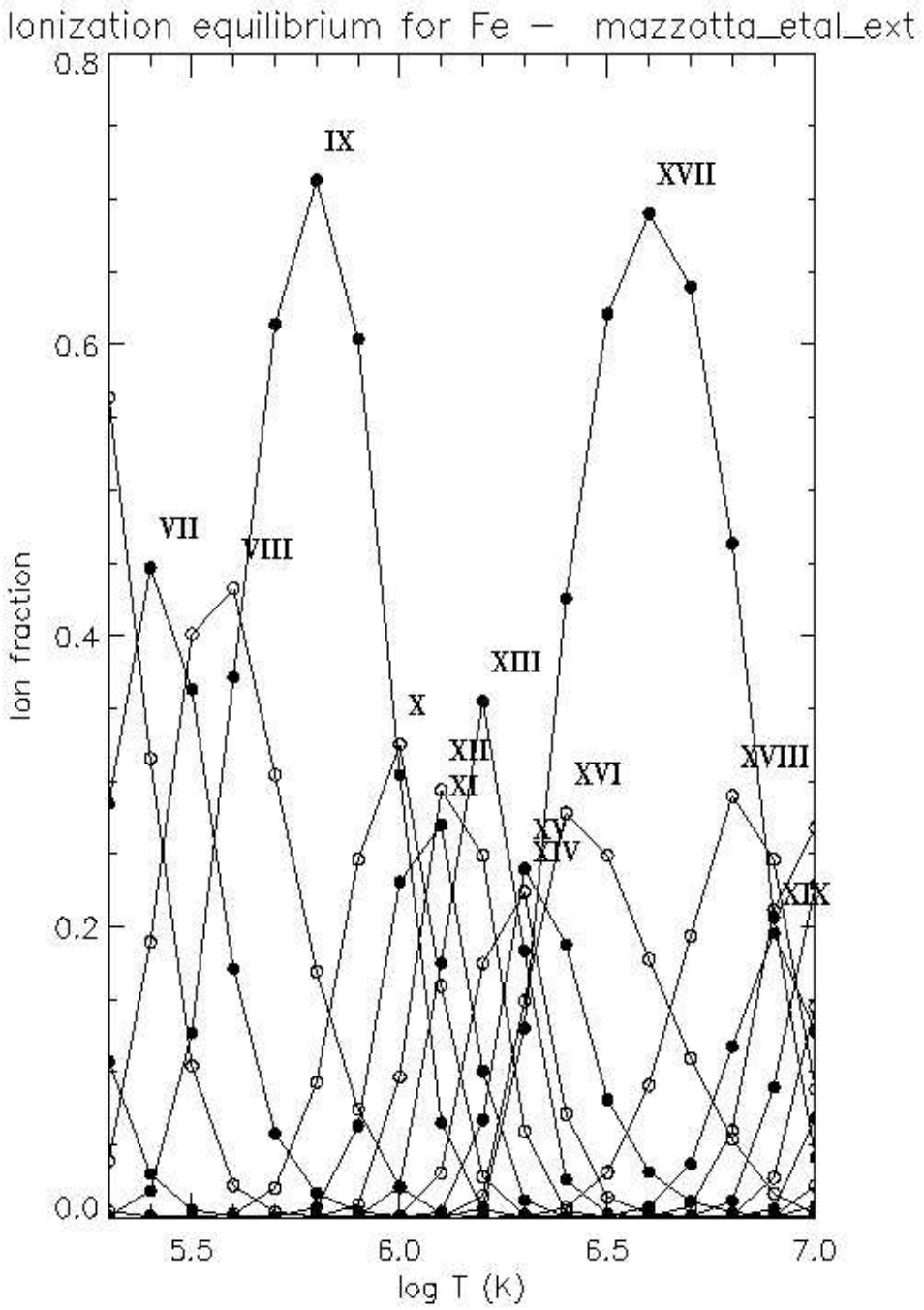

Figure 2.4: The ionization versus temperature curve for multiple ionization stages of iron (Mazzotta et al. (1998) [4]).

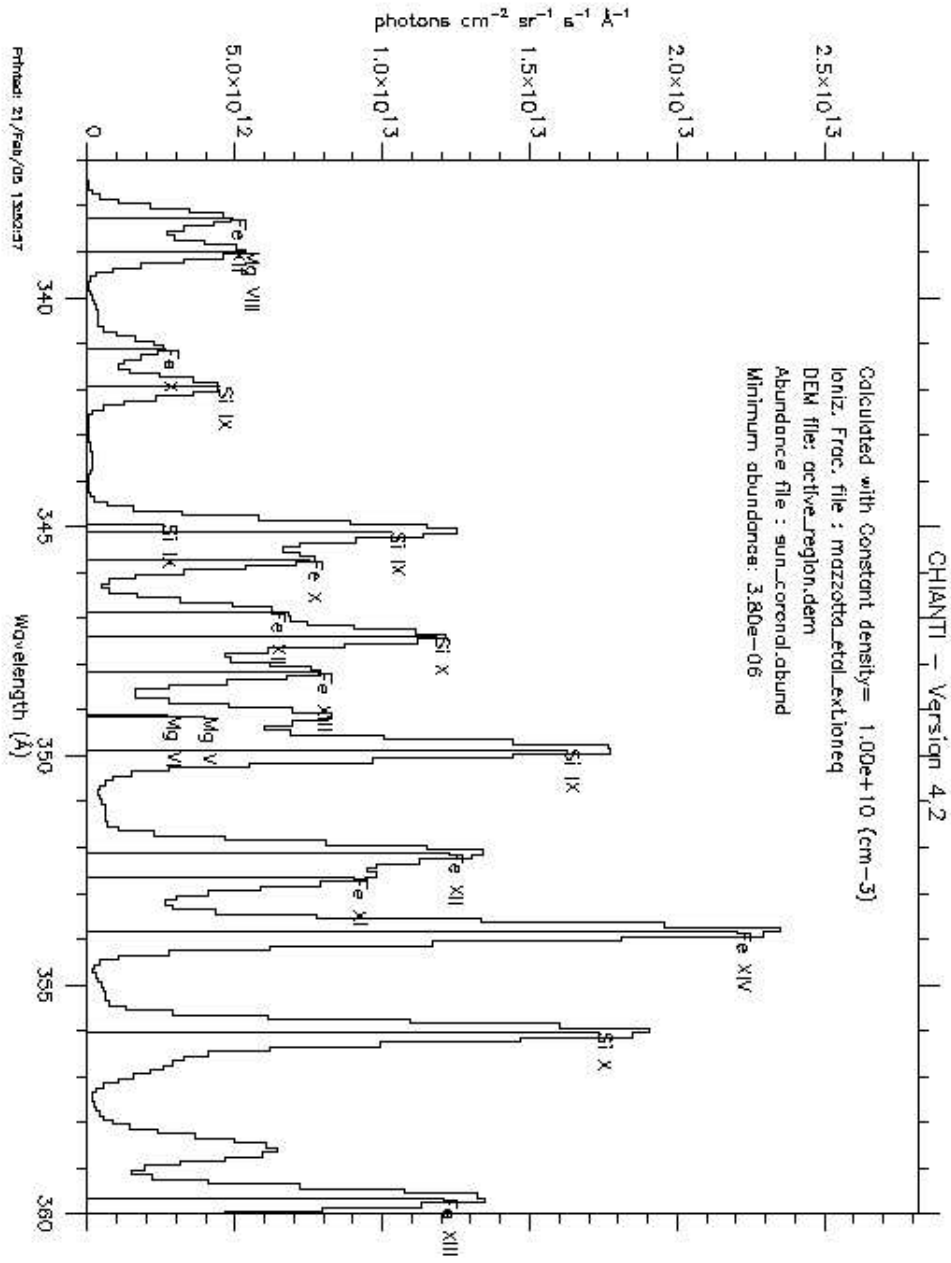

Figure 2.5: This is a sample plot of a fraction of the CDS NIS1 spectrum. The plot was made using the atomic database CHIANTI and a Differential Emission Measure Curve for an Active Region. The DEM was presented in Schmelz et al. (2001) [5].

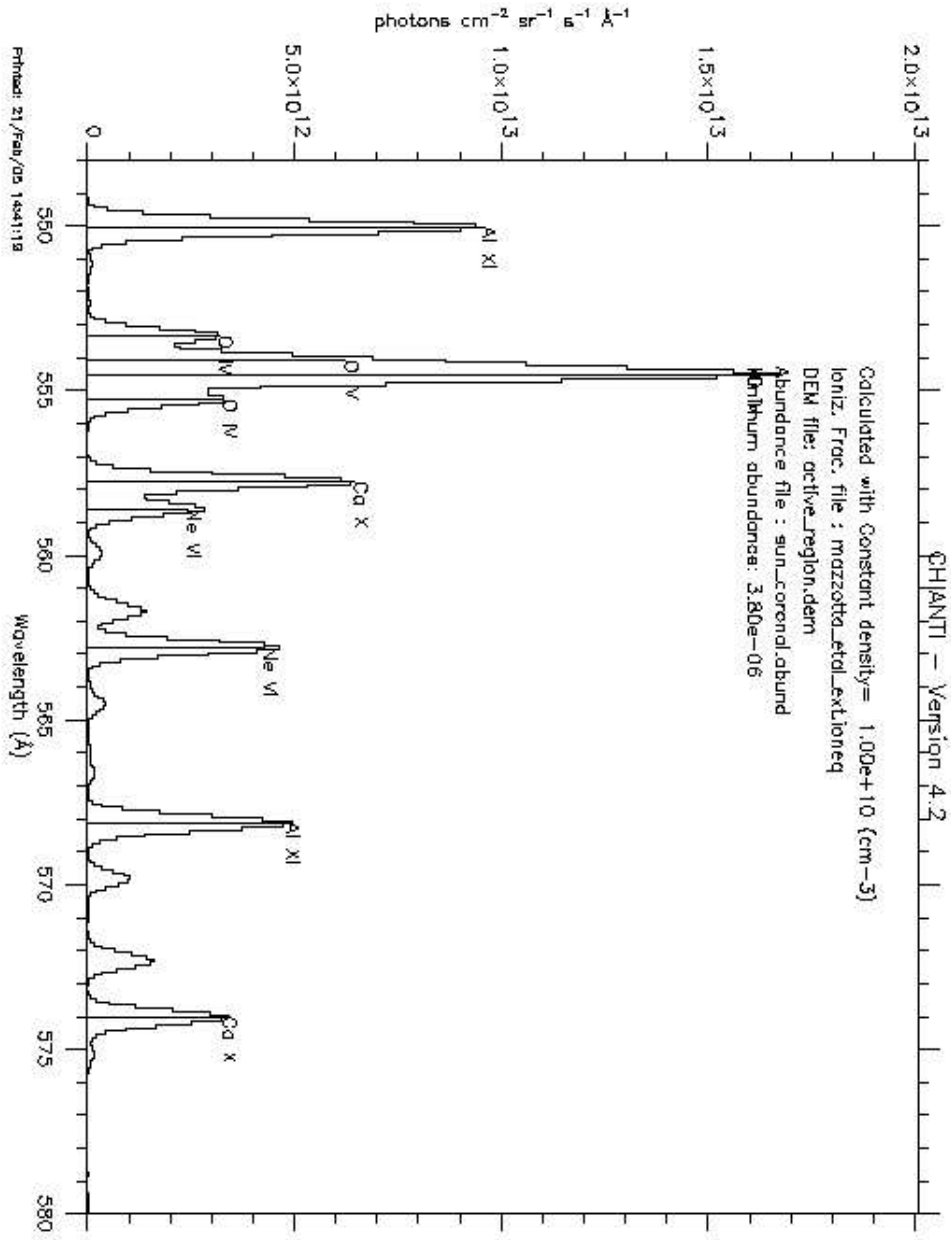

Figure 2.6: This is a sample plot of a fraction of the CDS NIS2 spectrum. The plot was made using the atomic database CHIANTI and a Differential Emission Measure Curve for an Active Region. The DEM was presented in Schmelz et al. (2001) [5].

The Narrow-band Imager, TRACE

Launched on April 2, 1998 from Vandenburg Air Force Base on a Pegasus XL launch vehicle, the Transition Region and Coronal Explorer [3] (TRACE) is a NASA Small Explorer (SMEX) class mission. It has been highly successful considering its small payload and low cost. It is designed to image the solar corona, chromosphere, and transition region, as well as the white light photosphere. For the last 7 years it has outperformed expectations, providing dazzling images of coronal loops, solar flares, prominences, and the eruptions of filaments preceding Coronal Mass Ejections (CME). Its low operational cost and high scientific return per dollar spent make it one of the most successful missions NASA has ever undertaken.

TRACE boasts the highest spatial and temporal resolutions of any EUV imager ever flown. It is a single telescope, and it circles the earth in low polar orbit providing over 8 months of uninterrupted solar observations per year. For the remaining portion of the year it is partially occulted by the earth for a fraction of each orbit. It has four passbands, three are in the EUV and the final passband is UV/white light.

Much of the TRACE instrument instrument concept was inherited from the Normal Incidence X-ray Telescope (NIXT) [31]. NIXT was a sounding rocket which developed the telescope and multi-layer coatings that were eventually used on TRACE. The optics package for the TRACE instrument was manufactured by the NIXT team at the Harvard-Smithsonian Center for Astrophysics in Cambridge, MA, and delivered to Lockheed Martin in Palo Alto, CA for integration into the telescope assembly.

The telescope for TRACE is a 30 cm aperture Cassegrain with an $8.5' \times 8.5'$ solar field of view. The telescope mirror is divided into four quadrants, with each corresponding to a passband for the instrument. It has a Nyquist-limited resolution with CCD pixels of $0.5''$. The image is focused onto a CCD coated with lumogen, a phosphor. Some of the instrument's physical characteristics are listed in Table 2.4.

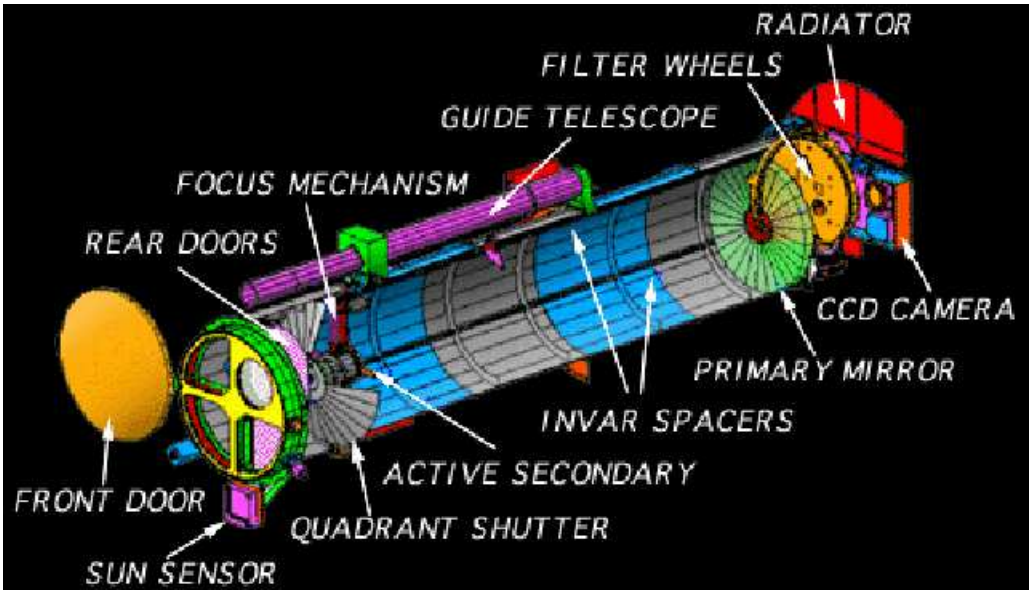

Figure 2.7: This image is a diagram of the TRACE instrument, and is courtesy of the TRACE team

Primary Diameter	30 cm
Effective Focal Length	8.66 m
Field of View	$8.5 \times 8.5'$
Resolution	$1''$
CCD	1024×1024 front illuminated
CCD Coating	lumogen
Pixel Size	21 μm ($0.5''$)
Pointing Stability	$0.1''$ RMS
Telemetry	700 Mb day^{-1}

Table 2.4: Some of the principal characteristics of TRACE [3].

TRACE Optics and Performance

The layout of the TRACE instrument is presented in Figure 2.7. At the front (sun-side) of the telescope are a set of four entrance filters. Light passes through the entrance filters and is reflected from one of four quadrants on the primary mirror; each quadrant is coated with a multi-layer thin-film coating to reflect EUV or UV light.

Upon reflection, radiation must pass through the two filter wheels before incidence on the phosphor-coated CCD.

The entrance filters are designed to permit transmittance of a specific range of EUV or UV radiation. Of the four filters, three are nearly triangular in shape, and are constructed out of aluminum. The UV filter is a circular 10 mm thick $\times$ 11.8 cm diameter Magnesium Fluoride substrate that has been coated with a broadband multi-layer coating. The UV coating, designed by Acton Research Corporation, was developed with a transmittance below 1600 Å and has high attenuation for radiation at 1216 Å and 1550 Å. The EUV filters are a composite of $Al_2O_3/Al/Al_2O_3/C$. At deployment these were the largest EUV filters ever launched into orbit. They were manufactured by Luxel Corporation, and the layers were 40 Å of Al_2O_3, 1500 Å of Al, 20 Å of Al_2O_3, and 50 Å of C, in that order front to back. The carbon film was applied to minimize oxidation on the filters, and the thicknesses of the layers of Aluminum Oxide were calculated as the necessary depth for transmittance of the required wavelengths of radiation while blocking the radiation at shorter and longer wavelengths. These filters are supported by an opaque Ni mesh, approximately 70 lines per inch. As an interested side note, this mesh is visible as a diffraction pattern in the TRACE images whenever an event of extreme intensity such as a flare is within the field of view.

The TRACE primary and secondary mirrors are made of Ultra-Low Expansion (ULE) glass. They were ground to a surface roughness of 7 Å RMS to permit a quality multilayer coating. These mirrors are partitioned into four quadrants; three quadrants on each mirror have matched Mo_2C/Si multi-layer coatings for EUV reflections, and the fourth quadrant is coated with a dielectric multi-layer designed to promote reflection of the C IV emission line at 1550 Å. The secondary mirror of the UV quadrant is coated with Al and MgF_2, which favors the 1216 Å and 1550 Å emis-

sion lines. The reflectivity curves for the TRACE EUV narrow passbands are shown in Figure 2.8.

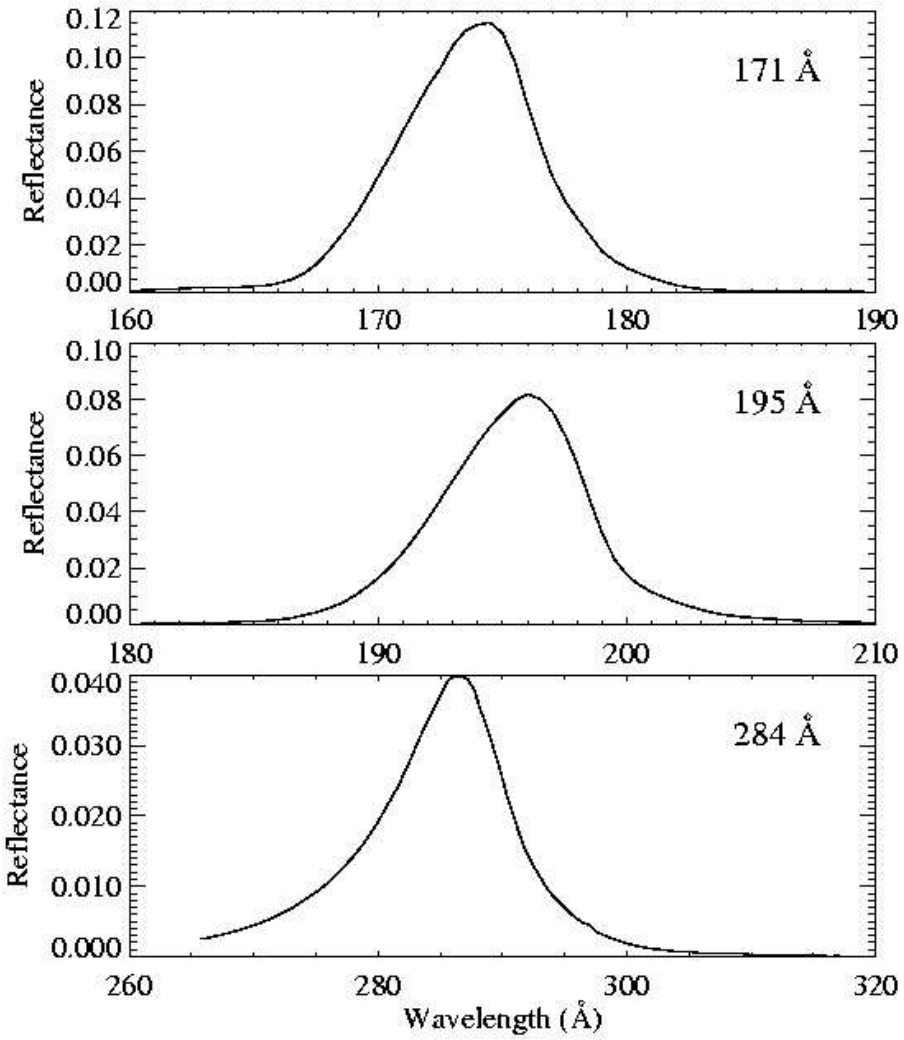

Figure 2.8: TRACE EUV reflectivities for the EUV passbands. This plot is a reproduction of a plot first presented in Handy et al. [3].

In the focal plane are two filters for either the prevention of stray light contamination that may result from pinholes in the entrance filters or the selection of specific wavelength ranges when using the UV channel. The EUV filters are generally used in combination with the entrance filters for stray light control, and are made from thin Aluminum. The UV filters (there are four in the UV selector wheel) are used in various combinations to produce images of specific spectral ranges.

The CCD is a front-illuminated 1024×1024 array. It has 21 μm pixels and is sensitive to wavelengths $\geq$ 4000 Å. The phosphor coating on the CCD front surface was applied with a thickness of 1500 Å, and it fluoresces visible light when impacted by EUV/UV photons. The quantum efficiency of the detector is a function of wavelength as shown in Figure 10 of Handy et al. [3].

The instrumental response of TRACE is a function of wavelength. This wavelength dependence is directly proportional to the temperature of the emitting plasma, and so TRACE images are temperature sensitive. This sensitivity to plasma temperature is complicated by the fact that each narrow passband, although only a few tens of Angstroms in scope, contains a number of emission lines. The passband wavelength centers are defined such that each channel "images" a primary emission line, while the other lines contributing to the total emission recorded by the channel are assumed to be of negligible intensity.

The crux of an argument presented later in this document is heavily dependent on the emission lines contained in the EUV passbands. It is therefore prudent to go into detail on the TRACE spectral coverage for each EUV channel.

The TRACE 173 Å Channel

The 173 Å passband, as the name suggests, is centered at approximately 173 Å. It has a wavelength range of about 11 Å, as is clear from Figure 2.9. Within this range of sensitivity are a number of emission lines. When the predicted intensity for

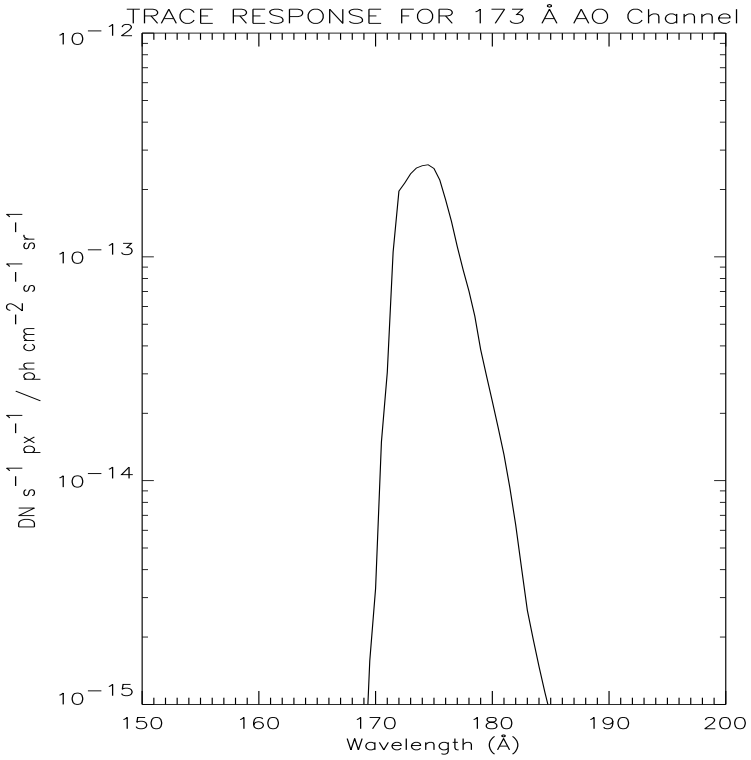

Figure 2.9: TRACE 173 Å wavelength response. This plot was generated using the known quantum efficiency, focal length, mirror effective area, filter throughput vs. wavelength, and several other instrument characteristics. The data were provided Leon Golub and Ed Deluca at the Smithsonian Astrophysical Observatory.

each of the emission lines is determined, they may be convolved with the response of the channel to produce an estimate of the counts detected for such a source. This calculation of the TRACE count rate is highly dependent on the emitting plasma, and the density and temperature prescribe the amount of emission (emission measure) expected from the different spectral contributions. The predicted counts for the 173 Å passband for a typical AR are shown in Figure 2.11. For this sample AR, a range in temperatures is expected, and an emission measure versus temperature, or Differential Emission Measure (DEM) curve, is used to specify the temperature and emission measure suspected to represent the AR plasma (Schmelz et al. (2001) [5]). As is evident from Figure 2.10, the TRACE 173 Å passband is primarily a Fe IX/X

pair for this assumed DEM. Figure 2.12 is a plot of the TRACE temperature response based upon this calculation for the contributions of each of the emission lines shown in Figure 2.10.

It is often assumed that the flux measured by the TRACE EUV channels is nearly isothermal. As is evident in Figure 2.12, this is not always a valid assumption for the 173 Å passband. The channel response is based upon the emission in the wavelength range designated by the filters, and the intensities of the emission lines are a function of temperature and density. Consequently, a structure in the field of view of the telescope could be at a high enough density so the contributions of the weaker lines typically 'washed out' by the Fe IX/X emission becomes appreciable. This is the case, in fact, during a flare. Ions at temperatures of nearly 10^7 K are present during these events, and emission lines in the range of sensitivity for the 173 Å channel produced by ions existing at these temperatures may dominate the channel or, at a minimum contribute significantly to the recorded flux. This is likely in the 173 Å case when one considers the contribution from the Ni XV line at 176.74 Å and the Fe XX line at 173.40 Å. Each of these is a strong emitter under the right circumstances, and certainly the temperature and density during a flare are sufficient for the production of these ions. For comparison to Figures 2.10 and 2.11, Figures 2.13 and 2.14 are included. They are the spectrum of the 173 Å pass band using a DEM for a flare (Dere et al. (1979) [6]) and the 173 Å predicted counts per pixel based upon this spectrum.

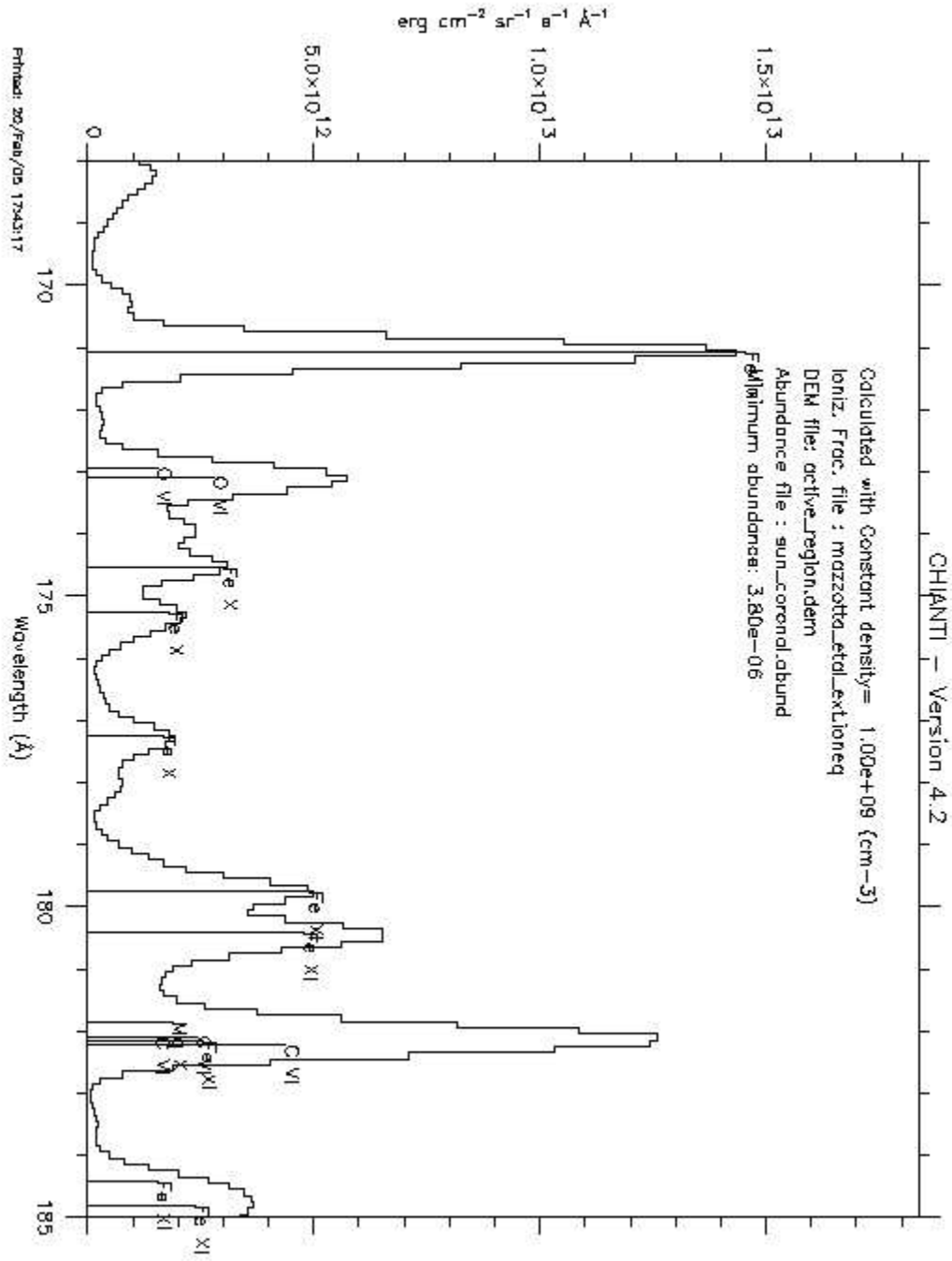

Figure 2.10: TRACE 173 Å AR spectrum. The plot was made using the atomic database CHIANTI and a Differential Emission Measure Curve for an Active Region.

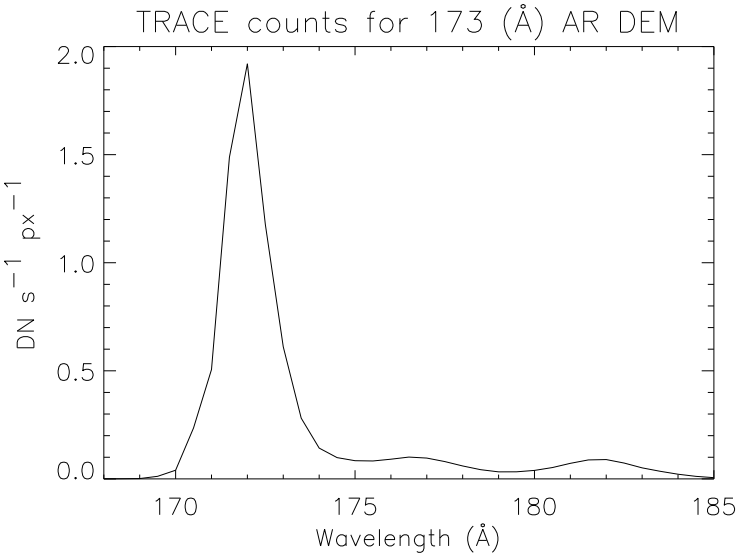

Figure 2.11: TRACE 173 Å predicted flux per pixel using the spectrum in Figure 2.10.

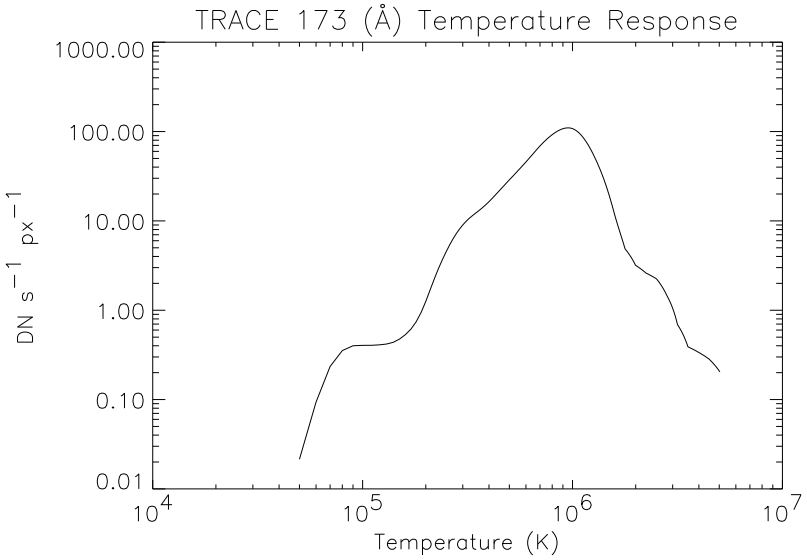

Figure 2.12: TRACE 173 Å temperature response.

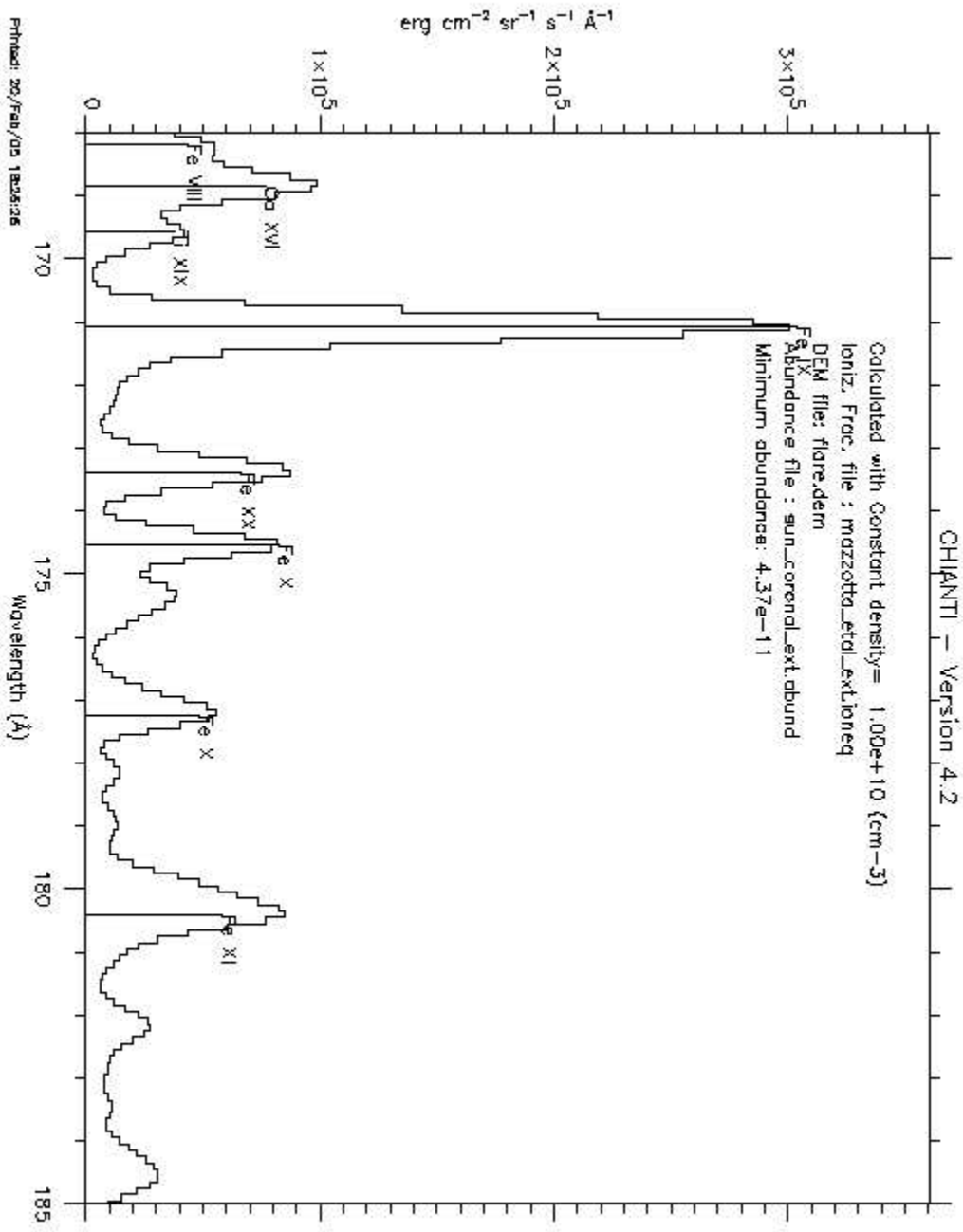

Figure 2.13: TRACE 173 Å flare spectrum. The plot was made using the atomic database CHIANTI and a Differential Emission Measure Curve for a flare. (DEM from Dere et al. (1979) [6]

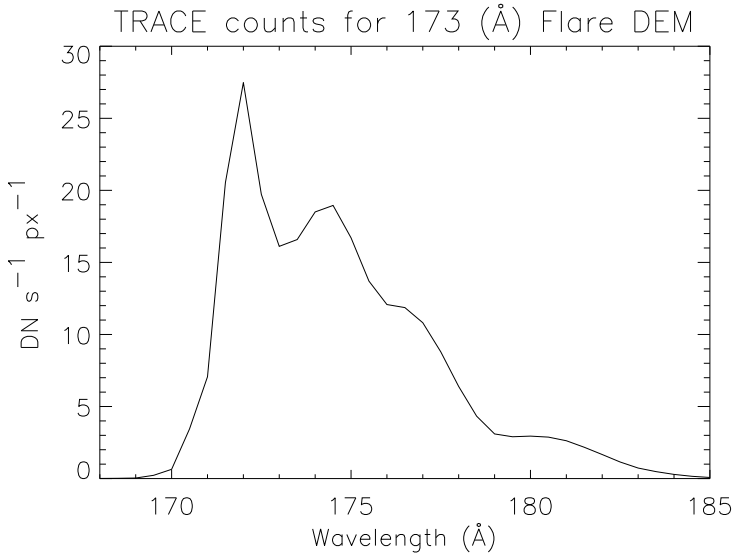

Figure 2.14: TRACE 173 Å channel predicted counts per pixel using the spectrum in Figure 2.13.

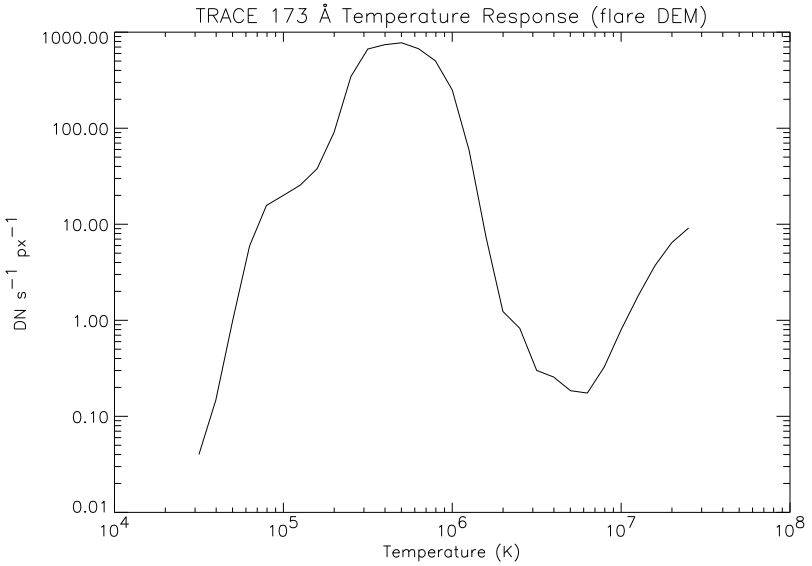

Figure 2.15: TRACE 173 Å temperature response using flare spectrum.

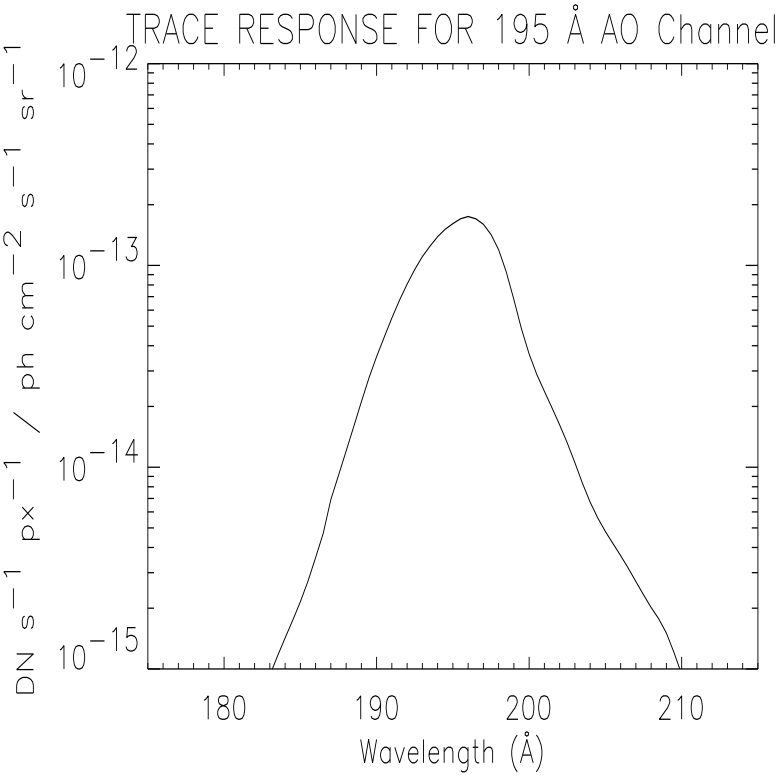

Figure 2.16: TRACE 195 Å wavelength response.

The TRACE 195 Å Channel

The 195 Å channel is dominated by several Fe emission lines from a number of different ionization stages. For the "typical" AR the counts in this channel are due to Fe XII emission at 195.119 Å. It has been shown by Del Zanna [32], that the Fe VIII line at 194.61 Å, may also contribute significantly to the flux in the 195 Å channel near the footpoints of AR loops. The AR spectrum for this channel is shown in Figure 2.17. The same input DEM curve used to calculate the spectrum of Figure 2.10 was used to generate this spectrum. From the predicted spectra shown in Figure 2.17, a plot of the counts as a function of wavelength was made and is presented in Figure 2.18. This method was employed again using a flare DEM and with the spectrum and predicted counts provided in Figures 2.20 and 2.21, respectively. The

temperature response of the 195 Å passband for an AR DEM is shown in Figure 2.19. The spectrum predicted for flare vs. non-flare observations clearly show the flux measured by TRACE is directly related to the emission lines found in the channel. For the flaring AR these are much different than for an AR where no flare has occurred.

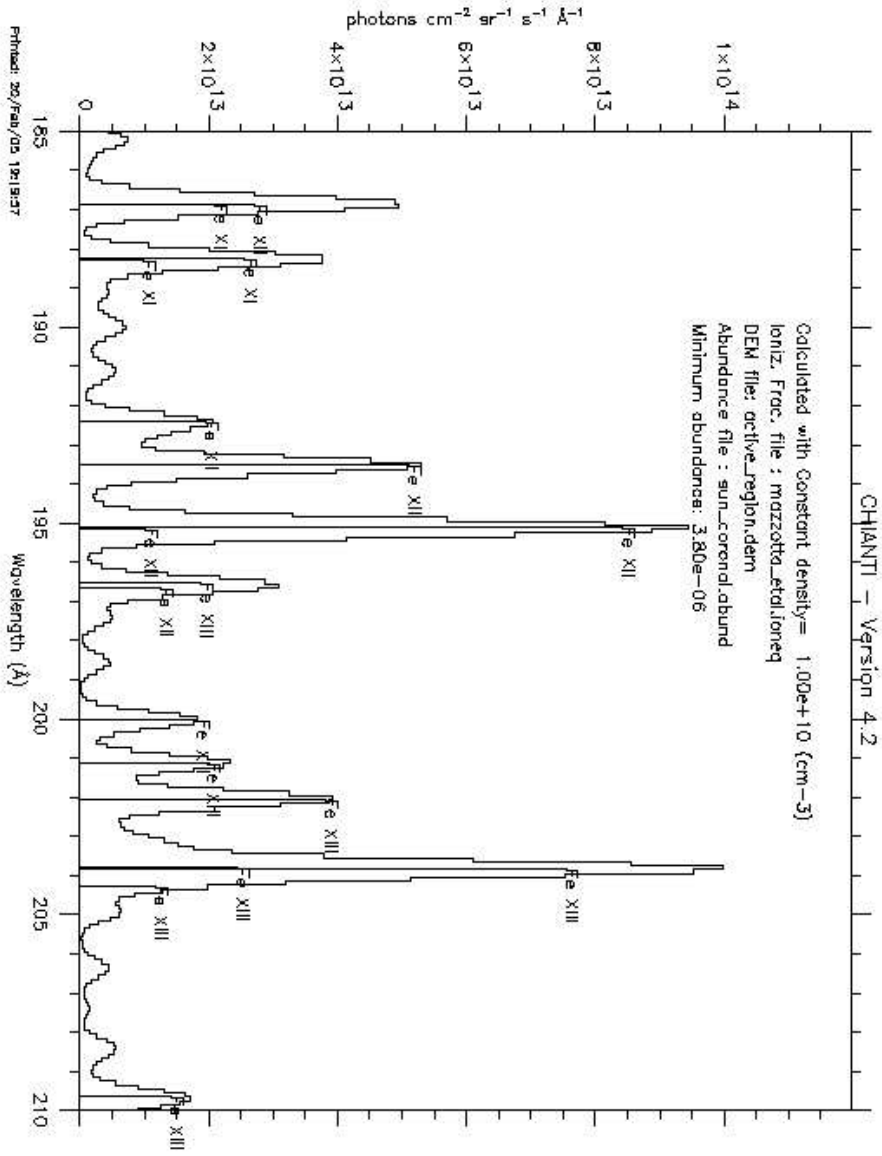

Figure 2.17: TRACE 195 Å AR spectrum. The plot was made using the atomic database CHIANTI and a Differential Emission Measure Curve for an Active Region (same input as used in Figure 2.10).

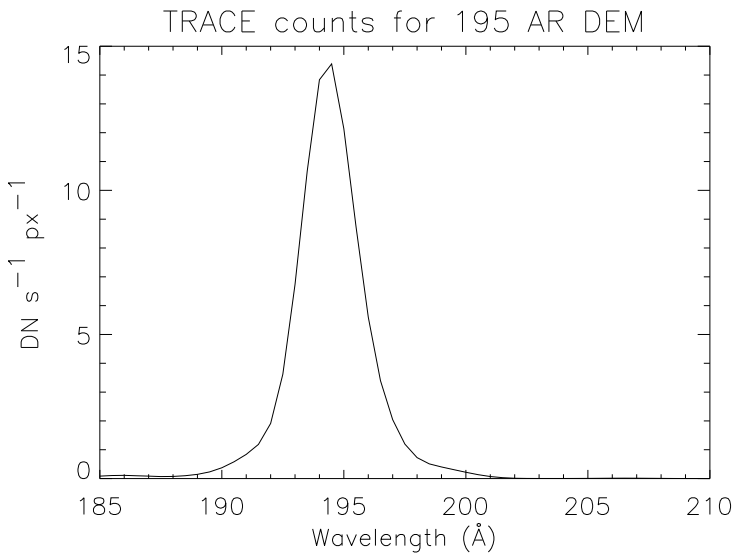

Figure 2.18: TRACE 195 Å predicted flux per pixel using the spectrum in Figure 2.16.

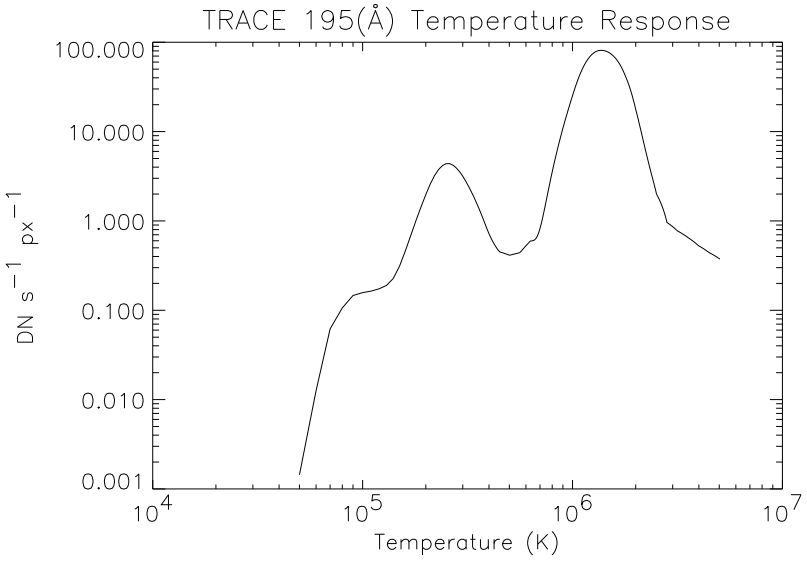

Figure 2.19: TRACE 195 Å temperature response using the spectrum for an AR.

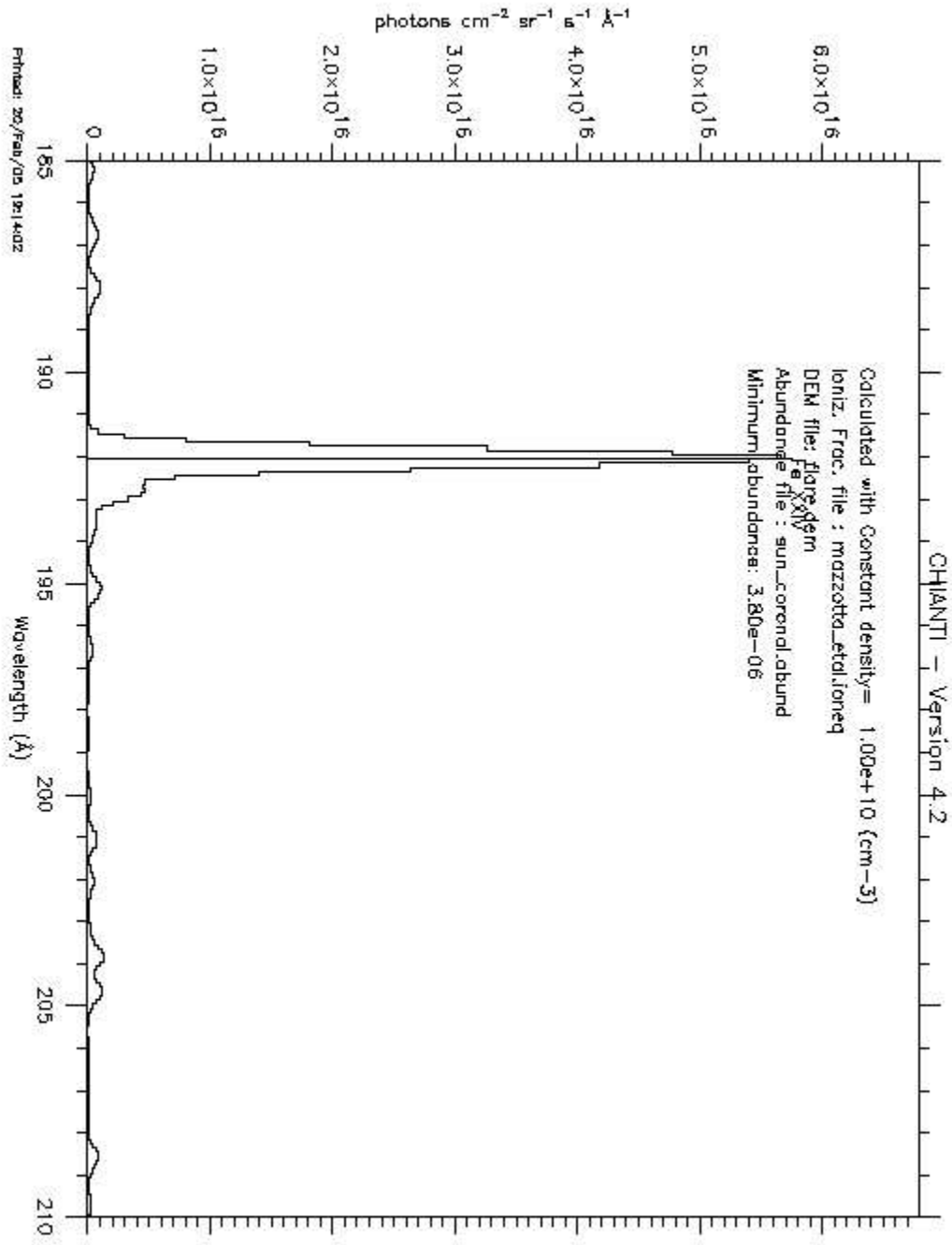

Figure 2.20: TRACE 195 Å flare spectrum. The plot was made using the atomic database CHIANTI and a Differential Emission Measure Curve for a flare (same input as used in Figure 2.13).

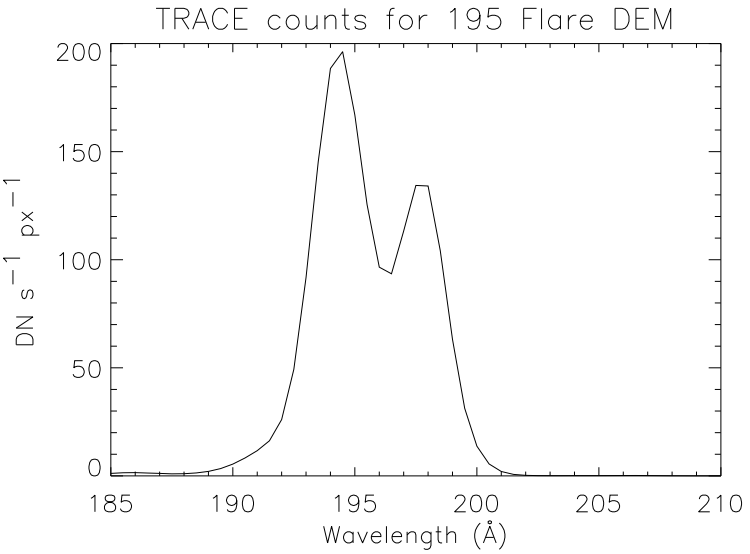

Figure 2.21: TRACE 195 Å predicted counts per pixel using the spectrum in Figure 2.19.

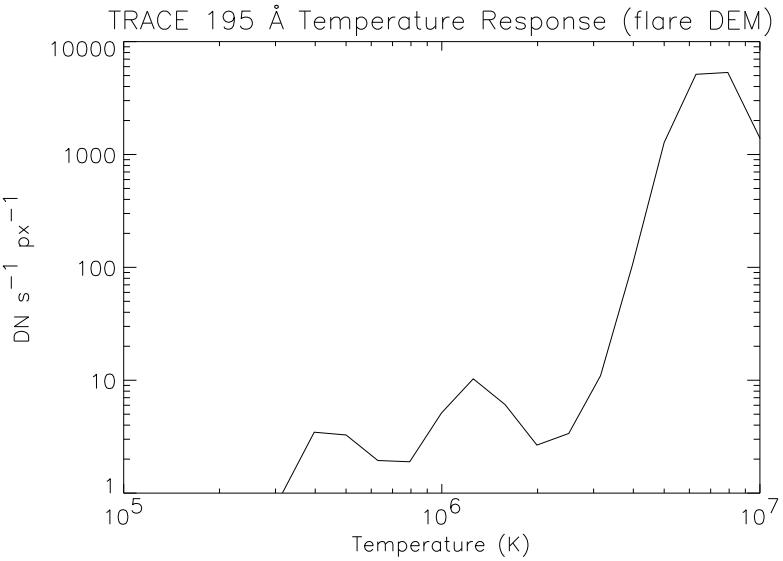

Figure 2.22: TRACE 195 Å temperature response using the spectrum for a flare.

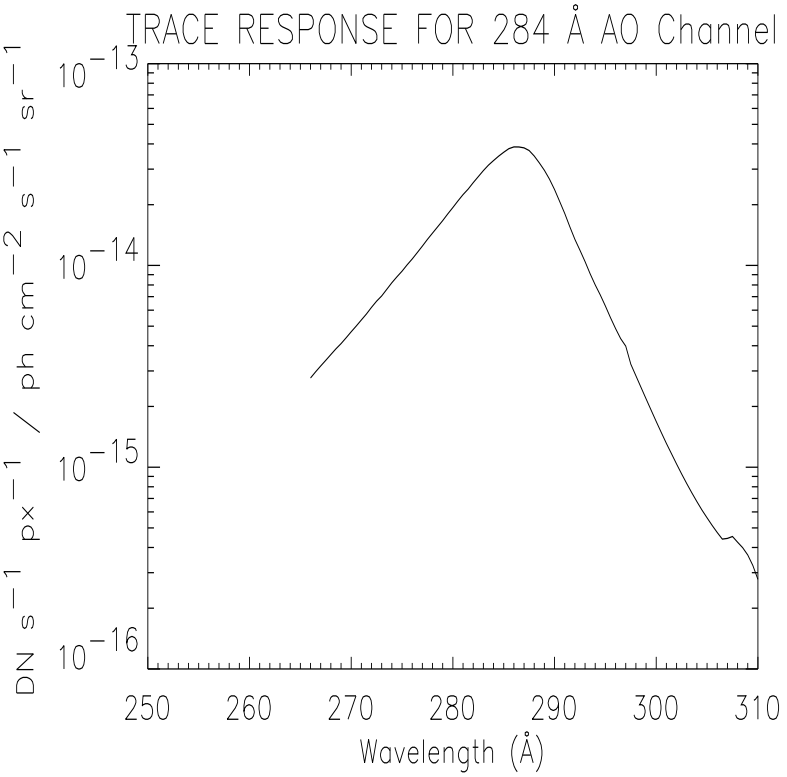

Figure 2.23: TRACE 284 Å wavelength response.

The TRACE 284 Å Channel

The 284 Å passband was designed to image high temperature plasma, generally resulting from a solar flare. The dominant spectral line in this passband, Fe XV, is formed near 2 MK and would not contribute significantly to total counts for non-flaring ARs. At 291.578 Å there is a S XI line that could dominate the channel during observations where the temperature of the plasma is lower than this flaring plasma temperature. Figure 2.22 demonstrates this observation; the only predicted counts are the result of the "cooler" AR lines with temperatures of formation in the range $10^{6.0-6.3}$ K.

The three previous sections on the TRACE EUV passbands indicate that plasma imaged with these narrow-band filters is highly dependent on the activity of the AR.

For non-flaring ARs, the narrow-band images of the solar corona may be observations of the emission from the ions that are generally "assumed" to produce the counts of the images. However, this is a very crude assessment of the plasma temperature, as the solution for the contributions to counts is non-unique. Please refer to Martens et al. [33] for an additional treatment of this currently debated topic.

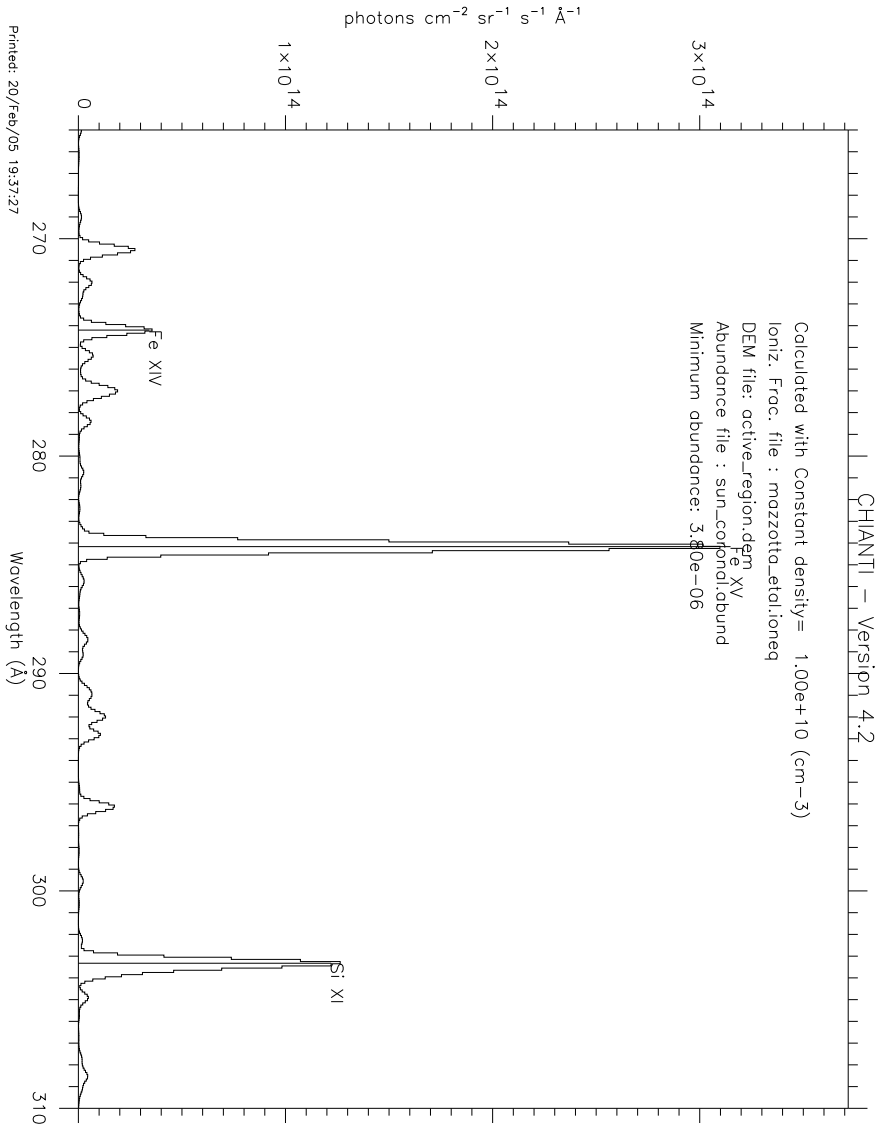

Figure 2.24: TRACE 284 Å AR spectrum. The plot was made using the atomic database CHIANTI and a Differential Emission Measure Curve for an Active Region (same input as used in Figure 2.10).

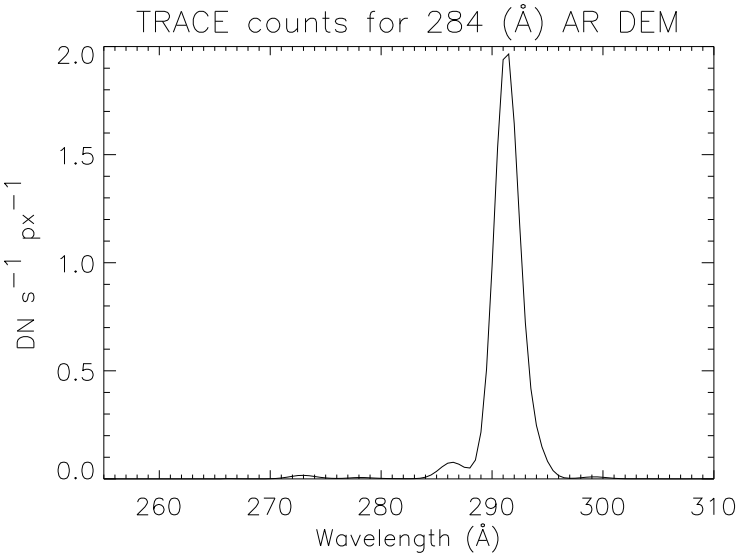

Figure 2.25: TRACE 284 Å predicted flux per pixel using the spectrum in Figure 2.24.

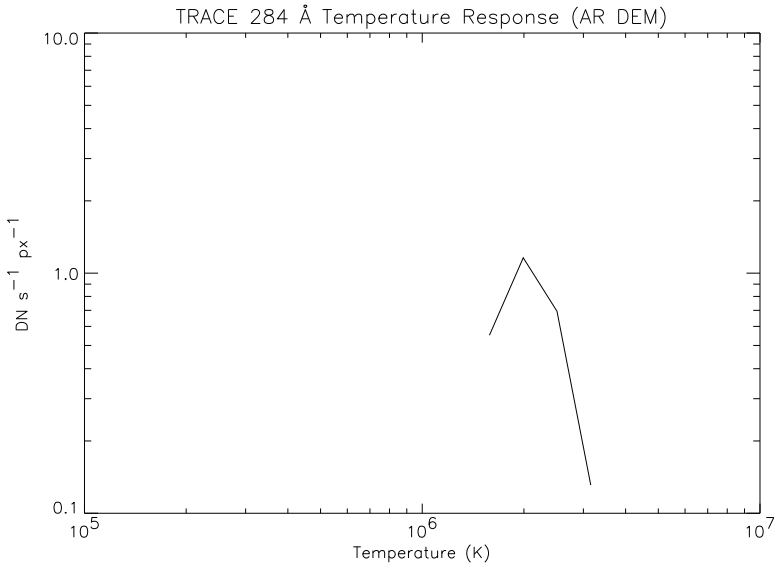

Figure 2.26: TRACE 284 Å temperature response using the AR spectrum.

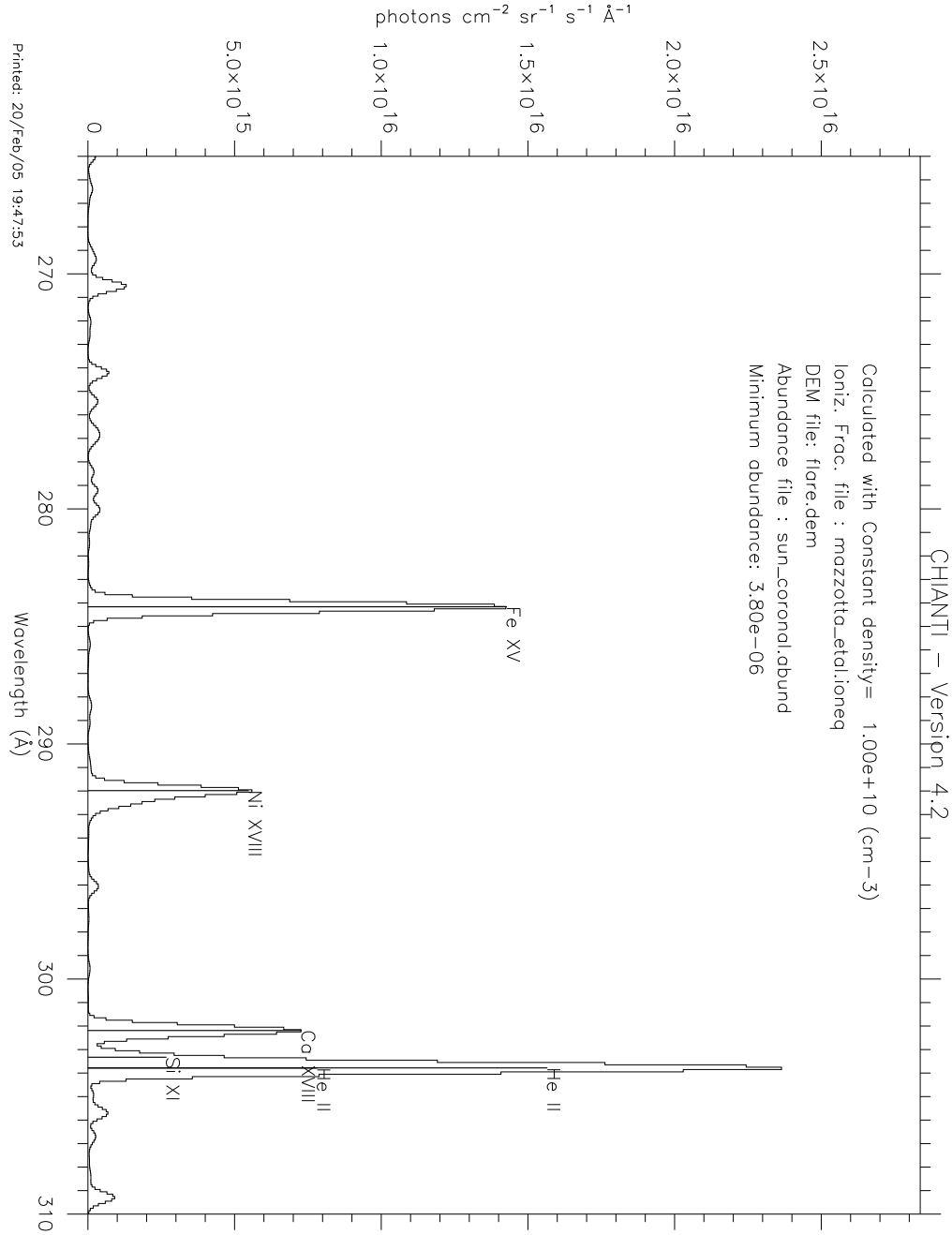

Figure 2.27: TRACE 284 Å flare spectrum. The plot was made using the atomic database CHIANTI and a Differential Emission Measure Curve for a flare (same input as used in Figure 2.13).

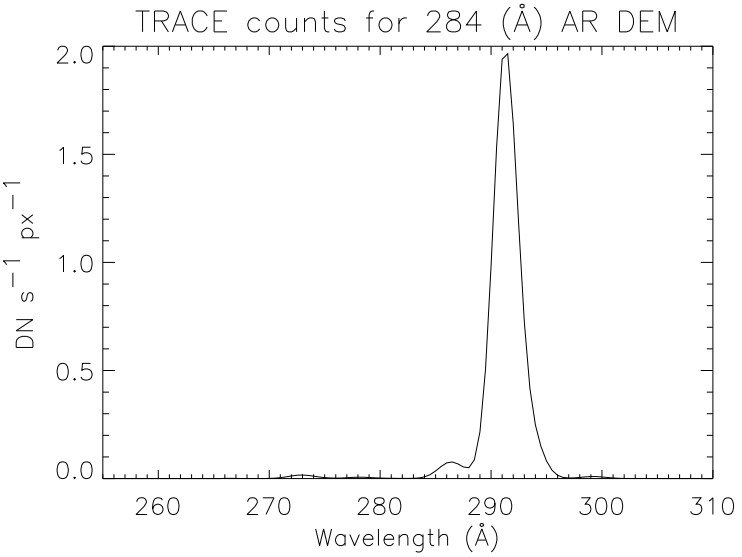

Figure 2.28: TRACE 284 Å predicted counts per pixel using the spectrum in Figure 2.27.

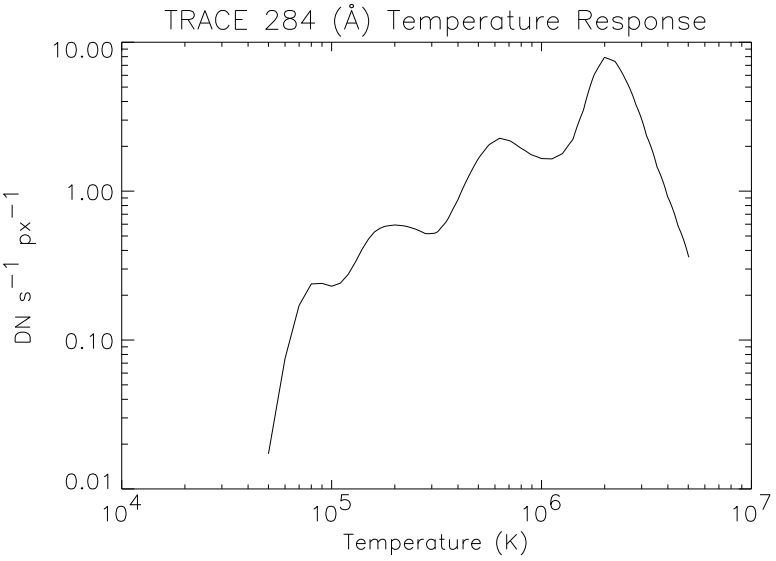

Figure 2.29: TRACE 284 Å temperature response using the flare spectrum.

Joint Observing Program 146

In an effort to combine the positive attributes of the TRACE and CDS instruments, a Joint Observing Program (JOP) was written. A JOP is a defined collaboration between several different observing platforms with a specific target and science goal. Our JOP was designed with this dissertation in mind, and the first observations were taken during the week of September 13, 2001. To date this program has been run on three separate occasions. In each instance several data sets were obtained that included sufficient data permitting a detailed study of AR coronae. The JOP, designated 146 by the SoHO Science Planning team, is described below, and the observations that have been made to date are listed for reference.

Fine Temperature and Density structure of Coronal Loops in a Bi-polar Active Region, as it is technically called, was submitted to the SoHO Science team. The text of the observing request read:

> Currently, several diagnostic approaches for the determination of the temperature stratification along loops exist, dependent upon the observing instrument. These determinations give widely differing results for the nature of the plasma within a coronal loop. Aschwanden et al (ApJ 550,1036; ApJ, 550,1059; etc.) has shown in multiple papers the nearly isothermal results obtained through filter ratios derived from EIT and TRACE data. J. Schmelz and others (ApJ, 556,896) have produced multi-thermal results through the analysis of spectra obtained from CDS observations while Priest et al. (ApJ, 539,1002) have developed a uniform heating model from SXT data. These separate studies have shown that results vary depending on the instrument and subsequent method of analysis. It is therefore of great necessity to perform a co-operative study with all these instruments further constraining the actual thermal gradient of coronal loops. There

have been many joint observing programs with similar goals. However, these have yet to provide a data set that both has a minimum of magnetic complexity, required to distinguish a unique structure by the CDS spectrograph, and co-observation by SXT, TRACE, CDS and EIT of a simple structure on the limb. Recently, JOP 145 was run with SXT, CDS, TRACE and EIT. This JOP offered all of the necessary criteria for the study except it changed target before the structure made it to the West limb. Unfortunately there are many data sets, but none offer that which is here stipulated as necessary to accomplish the scientific study suggested.

J. Schmelz has developed a Differential Emission Measure technique applied to spectral intensity numbers from CDS observations. This method can be modified to evaluate both the spectra from CDS and the filter output from TRACE and SXT. By comparing the spectral intensities from CDS with the 171 Å, 195 Å, and 284 Å filters from TRACE and the AlMg and Al filters from SXT, a high resolution composite of the loop can be created that has spectral data for the structure to further constrain the actual nature of the plasma in both temperature stratification along the loop and fine structure detail of the loop. This analysis method may provide the unique ability to determine the real temperatures of plasma within these structures as well as perform a diagnostic cross calibration of the three instruments.

Pointing:

This program is to be executed at the solar limb thereby minimizing projection effects and preferably targeting a region that has been under observation as it rotates across the disk.

Operation Details:

The JOP is to be performed in the following manner on a per instrument basis:

CDS: target of opportunity with as many sequences as possible.

TRACE: observations to overlap with other instruments when target approaches west limb. Previous observations as loop rotates across disk are preferred.

SXT: target of opportunity only with regard to the Partial Frame Images (PFI) images. The entire study will be on a target of opportunity basis for the month of September or as instrument schedules dictate.

CDS: Three sequences to be run: OLOOP1 and OLOOP2.

OLOOP1 creates a 160 x 240 arc second raster in six wavelength bands. These bands are He I 584 Å, O III 599 Å, O V 629 Å, Ne XI 562 Å, Mg IX 368 Å and Fe XVI 360 Å. It steps in 4 arc second increments. The exposure time at each position is 10 seconds resulting in a cadence of about ten minutes. This should be the initial program for the CDS observation. OLOOP2 has an almost identical purpose but it creates a raster with thirteen wavelength bands over approximately forty minutes. The wavelengths for this program include the six wavelengths for the OLOOP1 run with the addition of Si XII 520 Å, Si X 347 Å, Al XI 562 Å, Fe XIV 353 Å, Si IX 345 Å, Si X 356 Å and Mg X 624 Å. This sequence is intended to supplement the OLOOP1 program and should only be run after the OLOOP1 program has completed several runs. These sequences must be run simultaneously with TRACE and SXT. Multiple runs sequentially are preferred.

TRACE: Through the use of currently available observing programs, specif-

ically 'mostly171.utim' and 'mostly195.utim', coverage of an active region will be possible in 171 Å, 195 Å and 284 Å. These filters correspond to spectral lines available with CDS and provide approximate temperatures that overlap the temperatures available in CDS and SXT. Also intermittent C IV 1550 Å runs would be required to supplement the temperature analysis method to be subsequently employed. The observing programs that are suggested for use in this study offer a sustainable cadence of around 40 seconds. The 'mostly171.utim' offers the 171 filter for the main wavelength with 195, 284, 1550, 1700 and WL every eight cycles. The 'mostly195.utim' functions the same way but has 171 Å in context instead of 195 Å.

EIT: Cadence to be determined as allowed by the operations team. Partial frame images would significantly increase the cross calibration ability of the observer, especially in 171 Å, 195 Å and 284 Å. However, full disk observations in 171 or 195 would be beneficial for co-alignment.

SXT: This instrument uniquely provides the higher temperature analysis of these structures. The standard FFI table would be appropriate. If the active region is not so active as to overexpose the CCD on SXT a PFI table could be developed that would visit the limb and briefly point at an appropriate target. If the loop region is large a 128×128 PFI at full-resolution will be sufficient. This should use sequential exposures in Al.1, AlMg, and Al12 with automatic exposure control. PFI images could follow the same basic procedure with a 64×64 OR at full resolution. It is important to note that although the structure may not be visible in the SXT images, this to is an important null result.

JOP 146 was granted weekly priority on a per request basis. The primary goal of

the study was characterization of the properties of solar coronal loops. This was to be performed by convolving the data collected by the CDS and TRACE instruments.

The TRACE quadrant shutter began to suffer from an anomalous "software glitch" a few years after launch. Consequently, the science planning team was often hesitant to perform rapid movements of the shutter, which are required for high cadence multiple filter images. The first run of JOP 146 chose to only use the 173 Å filter to avoid the cost to the observing time when the quadrant shutter lost knowledge of the quadrant positions. Campaign 6805 began 11 September 2001, but was terminated due to the terrible events of September 11, 2001. It was resumed on 13 September 2001 and continued until 19 September 2001. CDS collected exposures from a set of 13 spectral passbands, and created 55 sets of 13 spectral images formed by moving the scan mirror across the southeast solar limb. These images are $160'' \times 240''$ for the OLOOP2 context images and $80'' \times 240''$ for the shorter duration OLOOP1 observing program. I operated TRACE and Dr. C. Kankelborg supervised. TRACE made 13,786 1024×1024, or $512'' \times 512''$, 173 Å images. TRACE also made 364 images with the UV channel. These were taken for context and co-registration with the SoHO/MDI images.

JOP 146 was next performed as Campaign 6873 from 11 June through 16 June 2002. No terrorists attacked the USA during this period, and the observations were uninterrupted. The requested observations from each instrument were modified from the previous run of the JOP, and a smaller set of spectra were taken using a smaller field of view. The reduction in the number of exposures and spectral lines was certainly a drawback, but the desire to cover as much of the ARs observed in as short a time as possible required this adjustment. CDS generated 66 sets of raster images. JLOOP1 was a set of four passbands with a field of view (FOV) of $114 \times 240''$. The FOV of JLOOP2 was the same as that for JLOOP1 but incorporated the 13 pass-

bands used in OLOOP2. Limiting the FOV in this manner was not a wise decision since any inaccuracy in the selection of the pointing could completely miss the AR and so this type of observing routine was avoided in later observations. TRACE made another 10,235 1024 × 1024 173 Å images, 85 1024 × 1024 195 Å images and 978 512 × 512 UV images.

The final "official" operation of JOP 146 was Campaign 6918. This was performed 14 - 20 January 2003. This is arguably the finest data ever collected on the solar corona. The previous two observations provided quality data, but were also most instructive in the techniques for making the observations. Several procedural and structural changes were made to the observing routines for both CDS and TRACE. The challenge in developing these observations is not TRACE program definitions; it is the use of CDS that is difficult. In order to maximize the coverage area, spectral coverage and cadence must be sacrificed. Spatial resolution is $\approx 2''$ at best, and the time required to collect sufficient information on some of the lines formed at lower temperatures can be 40 seconds or more. In an effort to play one hardship off of the other, the CDS observations were partitioned into four different classes:

1. Long duration observations, each with 20 passbands, were made for context images. These were 60 second exposures per step with a FOV equal to 241 × 240″. These were given the program name ARDIAG2 (AR Diagnostic).

2. Fourteen passbands were used in the ARDIAG4 routine. These had a FOV of 104 × 240″ and were not subsequent steps as were the previous observations, but innovatively skipped 8″ between each exposure. This scanned the AR in a much shorter time without sacrificing spectral coverage.

3. Fourteen passbands were also used for the so-called fast scans. These were 53 × 240″ rasters; this time 12″ were skipped between exposures.

4. Finally, ten passbands were used to generate $244 \times 240''$ high spectral and spatial resolution images with the $2''$ slit.

CDS collected 243 sets of data during this week of observations to form a total of 2163 raster images. Having fine-tuned CDS, TRACE multi-EUV passband images were requested of the planner. He agreed. (I was the planner.) This presented a mild risk of the shutter sticking and no data being collected, but it was for a good cause. TRACE performed brilliantly taking 5885 1024×1024 173 Å images, 439 1024×1024 195 Å images, and 287 512×512 284 Å images. In addition, MDI high resolution magnetograms were made of an AR JOP 146 target near disk center.

The data that resulted from the last operation of the JOP have spawned an international collaboration of scientists from the University of Cambridge (UK), Mullard Space Science Laboratory (UK), St. Andrews University (Scotland), the Smithsonian Astrophysics Observatory (SAO), Montana State University (MSU), the Naval Research Laboratory (NRL), and several others. The data presented in the following chapter is a subset of the data collected during JOP 146 operations. A group of scientists from SAO, MSU, MSSL, and the University of Cambridge will present the preliminary results of the first study at the European Geophysical Union annual meeting April 2005 and at the Solar Physics Division of the American Astronomical Society annual meeting May 2005.

An example of the multi-EUV filter observations is shown in Figure 2.27.

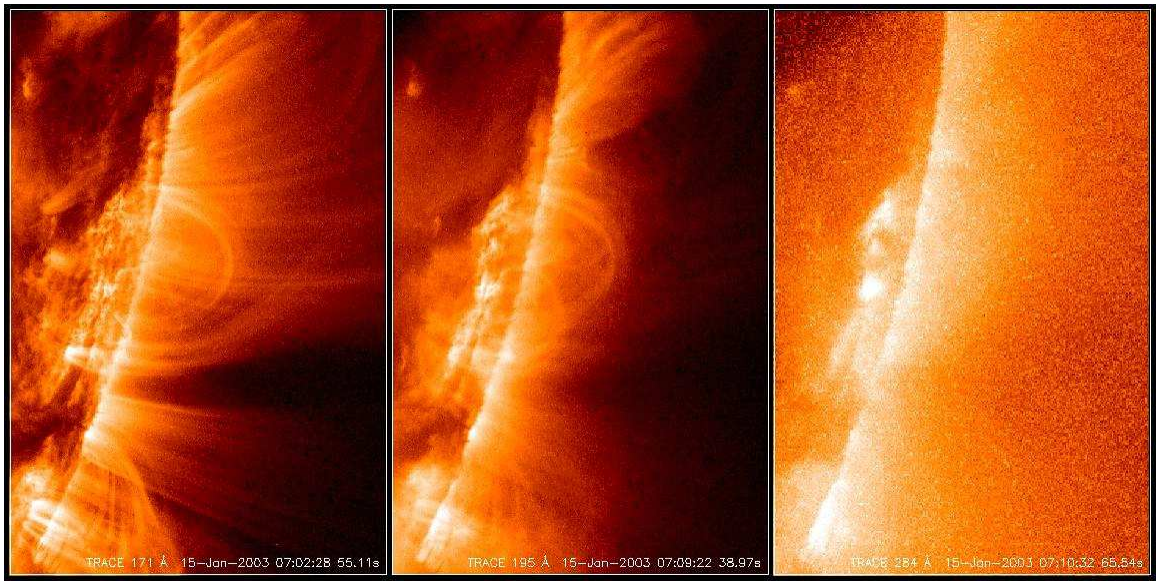

Figure 2.30: TRACE EUV filter images from JOP 146. From left to right, these are 173 Å, 195 Å, and 284 Å images. Notice that the 284 Å image does not contain many (if any) resolved structures. This is an important observation that will be examined in Chapter 3.

CHAPTER 3

THE UNRESOLVED EUV CORONA

Introduction

After the results from the X-ray experiments on *Skylab* it has become well established that the most prominent source of coronal X-ray emission is elongated arch-like structures called coronal loops. In the last decade several new instruments further refined our view of the corona. Observations from missions like the Solar Maximum Mission (SMM), *Yohkoh*, the SoHO, and TRACE confirm the results of *Skylab*: the corona is a highly-structured, complex atmosphere. It has several evolutionary length and time scales, dependent on the emergence of magnetic flux from below the photosphere and magnetic recombination and relaxation processes in the corona.

There is much debate over the analyses of the recent flood of data available from the numerous telescopes. There are many different conclusions about the actual temperature and density of coronal loops. Del Zanna and Mason (2003) [32] note that the discrepancies among these differing results are most likely due to an inappropriate approximation for the background contribution to the total emission.

Recent journal articles (for example Testa, Peres and Reale (2002) [34]) conclude that it is necessary to subtract the background contribution to intensity in order to derive the physical characteristics of a structure. Several methods are currently employed in an attempt to correct for this line-of-sight "contamination". For example, Testa et al. (2002) [34], using TRACE 173 Å data, determine the background emission by first finding the real intensity profile measured across a structure's cross section

along a 1×8 pixel strip. An example of this is shown in Figure 2 of their paper. The background is assumed to be the intensity below the line that is fit to the minimum of the intensity profile, and the peaks of the profile correspond to the loops which are along the strip of pixels. The value for the background is then subtracted from the data to yield an approximate measure for intensity due only to emission from the structure. Winebarger, Warren and Seaton (2003) [25] use a method similar to one first introduced by Porter and Klimchuk (1995) [35]. With this technique the image is deformed to be rectangular with the coronal loop of interest running lengthwise through the middle of the rectangle. The pixels within the loop are set to zero and assigned a new value found by linear interpolation of the data points (pixels) that are just outside the strip of loop pixels. This image is smoothed and then subtracted from the original image. The uncertainties associated with this method come from the Poisson statistics and the errors resulting from the background subtraction. An example of this method is shown in Figure 3 of Winebarger et al. (2003) [25]. Del Zanna and Mason (2003) [32] have calculated the intensity of emission lines for pixels within and just outside the coronal loop and have corrected the value for intensity by subtracting the background measured value from the intensity for a pixel within the loop.

It is important to analyze and understand the physical origin of solar EUV and soft X-ray emission, both from flares and ARs, to enable modeling and forecasting of flares and CMEs. We cannot even begin to accurately model AR solar EUV emission if we do not know whether its main source is in coronal loops – as is widely assumed – or in the unresolved background. In this thesis we will demonstrate that the EUV background emission surpasses that of loops, in contrast to the situation for soft X-rays, a finding in support of Del Zanna and Mason (2003) [32]. *Hence any future comprehensive physical model for coronal heating will have to predict both the loop*

and background components of the emission. We have analyzed two non-flaring ARs and we find that the scale height temperature determined from the observations is consistent with that expected for an isothermal hydrostatic atmosphere.

Instead of the typical analysis of individual coronal loops, this work is a study of the emission from an active region as a whole. A possible explanation for the emission from the unresolved corona is offered, and a systematic method for more accurately accounting for this emission is provided. The observations and the data reduction techniques applied are outlined. We analyze the corona in two active regions on the east limb using ion emission lines of ions formed in a temperature range of 1 MK - 3 MK. An analysis of an AR above the west limb is also presented; 20 CDS passbands were available for analysis during this observation. The intensities for the CDS spectral passbands are measured, and the curve fitting technique applied to the observed decrease in intensity as a function of altitude is outlined for the first of the three ARs. We apply same method to all three ARs. We then describe the different functions used to determine the best fit to the observed intensity decrease with altitude. The conclusions of the EUV coronal background investigation are detailed in Chapter 5, as well as the conclusions pertaining to a study of post background subtraction flaring-AR loops.

Active Region 9628

AR Background studies of JOP 146

JOP 146 was initially designed to investigate the physical properties of active region coronal loops. Data collected by JOP 146, SoHO Campaign 6805, includes images taken with the TRACE 173 Å filter and spectral line intensities collected by CDS. During this campaign SXT also observed the target with the Al.1, Al.12, and AlMg filters. Although not directly requested for support, EIT observed the solar

corona in the standard sequence whereby images were taken using all the filters. The EIT images provide useful context and were used in the co-alignment of the data from CDS and TRACE. The temperature coverage extended over 0.075 - 5 MK. The TRACE images are 20 second exposures with a $512'' \times 512''$, $\approx 8'$ field of view. The spatial and temporal resolution of TRACE allow observations of the structural evolution within the field of view. The TRACE images also allow us to identify the number of loops resolved by TRACE that contribute to the emission within one CDS pixel. This is an important constraint: CDS has pixels that are 8×3 times larger than those of TRACE, and many solar coronal features are far below the resolution of CDS.

JOP 146 requested observations of the corona below 100 Mm. The targeting was chosen so that the limb was present in the image but filled a minimum of the total field of view. Additionally, to limit the total time needed to complete the CDS raster, we requested 40 exposures per raster from CDS, limiting the CDS coverage to 112 Mm above the limb. These requirements provide solar limb context for co-alignment between instruments and allow for approximate altitude determinations.

The start time for the CDS investigation was 18 September, 2001, 15:39 UT. We present results using five raster scans, ending with a scan that began at 20:14 UT. We used the $4 \times 240''$ slit, and the raster field of view was 160×240 ″. The rasters were composed of 40 exposures, each exposure had a duration of 60 seconds, with a total time to complete the raster of approximately 50 minutes. A balance between spectral coverage and the time to complete a raster required limiting the number of wavelength passbands. CDS measured spectral line intensities for spectral lines contained within 13 passbands.

We have intentionally neglected the presentation of the analysis for the ions with a peak formation temperature below 1 MK as these ions do not exhibit the same

decrease with altitude as the ions formed above this threshold temperature. The ions used in this study are listed in Table 3.1. We intend to present the results for the transition region lines (below 1 MK peak formation temperature) at a later date. In a future work, We will show what inference can be drawn from the fact that only the transition region lines show pronounced increases in intensity resulting from a compact flare event, These transition region lines did not exhibit the same exponential decrease in intensity as the ions formed above 1 MK..

Ion	λ_{pred} (Å) (CHIANTI)	Transition	$T_{pf}(\log_{10})$
Mg IX	368.070	$2s^2\ ^1S_0 \leftrightarrow 2s2p\ ^1P_1$	6.05
Si X	347.403	$2p\ ^2P_{\frac{1}{2}} \leftrightarrow 2s2p^2\ ^2D_{\frac{3}{2}}$	6.10
Mg X	624.941	$1s^22s\ ^2S_{\frac{1}{2}} \leftrightarrow 1s^22p\ ^2P_{\frac{1}{2}}$	6.15
Fe XIII	348.184	$3s^23p^2\ ^3P_0 \leftrightarrow 3s3p^3\ ^3D_1$	6.2
Si XII	520.668	$1s^22s\ ^2S_{\frac{1}{2}} \leftrightarrow 1s^22p\ ^2P_{\frac{1}{2}}$	6.25
Fe XVI	360.768	$3s\ ^2S_{\frac{1}{2}} \leftrightarrow 3p\ ^2P_{\frac{1}{2}}$	6.40

Table 3.1: Spectral Lines Observed with CDS for JOP 146 used in this study with a peak formation temperature above 1 MK.

The target for SoHO Campaign 6805 was AR 9628, which appeared on the south-east limb on 17 September 2001, and was completely visible on the disk by 19 September 2001 at 0300 UT. The active region covered about 3′ (120,000 km) in latitude. An intensity image using the Si XII emission line is provided in Figure 3.1. A TRACE 173 Å image is shown in Figure 3.2. This image includes the radial line we present in detail (solid line). Four other radial lines are also plotted in Figure 3.2; these dashed lines are additional radial lines we used to determine the intensity versus altitude and the results for these dashed lines are presented in Table 3.3. The two arrows in Figure 3.2 point out unresolved structures in the TRACE image.

Many transient loops seen in the TRACE images are also evident in the CDS observations. In addition to these dynamic structures, rising ballistic material from a compact M 1.4 flare is observed to travel along the field lines and then fall back to the

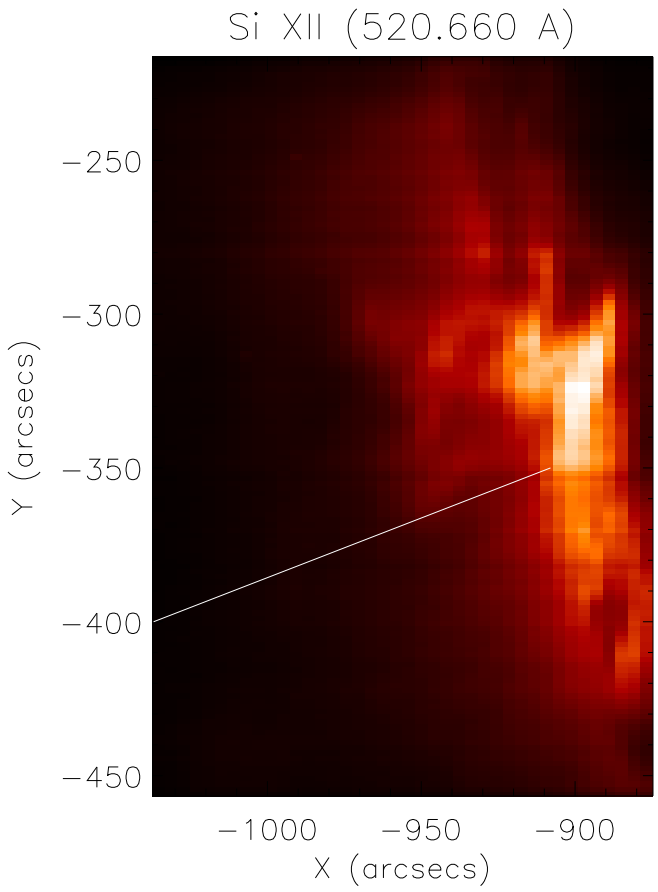

Figure 3.1: Si XII (520.660 Å intensity image with radial line. Raster began at 15:39:11.201 UT

chromosphere. The evidence of this flare is clearly shown by the the Geostationary Operational Environmental Satellite 8 (GOES)[1] plot of the solar X-ray output per one minute interval (Figure 3.3).

In spite of the vigorous activity of the AR below a few tens of Mm, we will demonstrate that the unresolved corona appears to be mostly unaffected by the activity at least in terms of any departure from hydrostatic equilibrium. The term unresolved

[1]http://rsd.gsfc.nasa.gov/goes/text/databook/section01.pdf

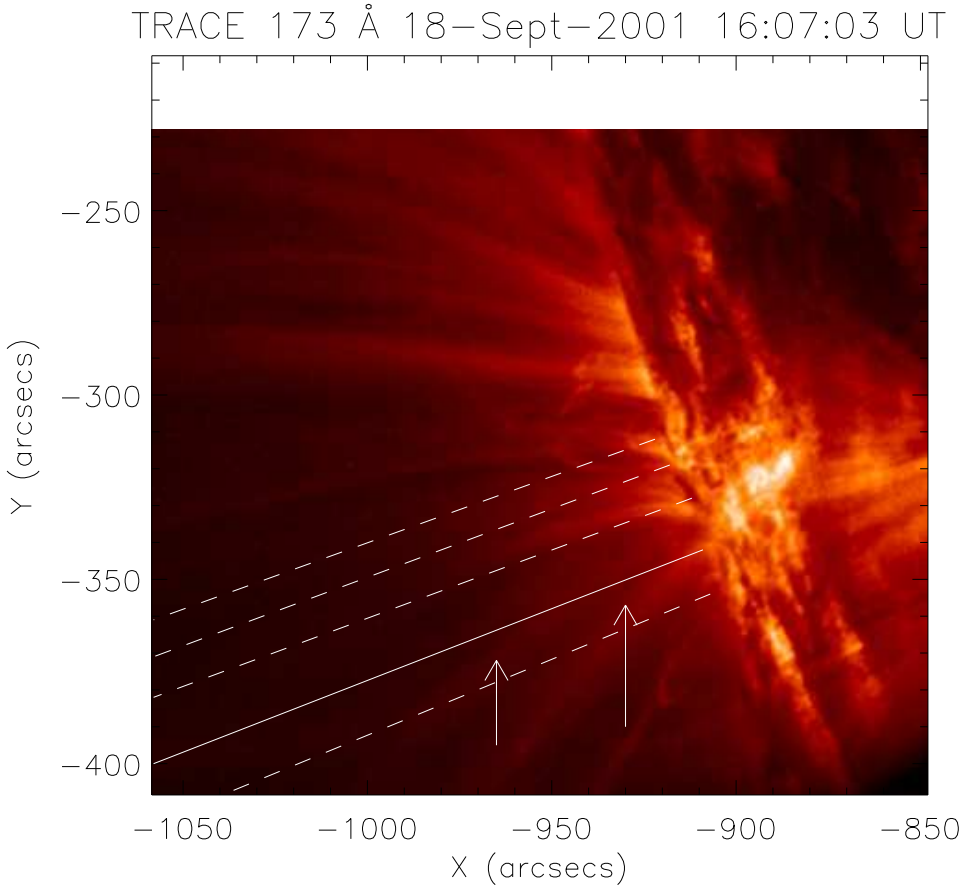

Figure 3.2: TRACE 173 Å image of AR 9628 including the main radial line of this study (solid line). For the solid radial line, intensities have been determined as a function of position along the line for the CDS intensities. The results for the dashed lines are presented in Table 3.3. The two arrows indicate unresolved structures in the image.

corona is used to imply that the background consists of loops that are so numerous that they are not separable by current imagers. This step from unresolved to resolved structures is evident in comparisons between EIT and TRACE data, and we believe that this will be seen again when higher resolution observations become available.

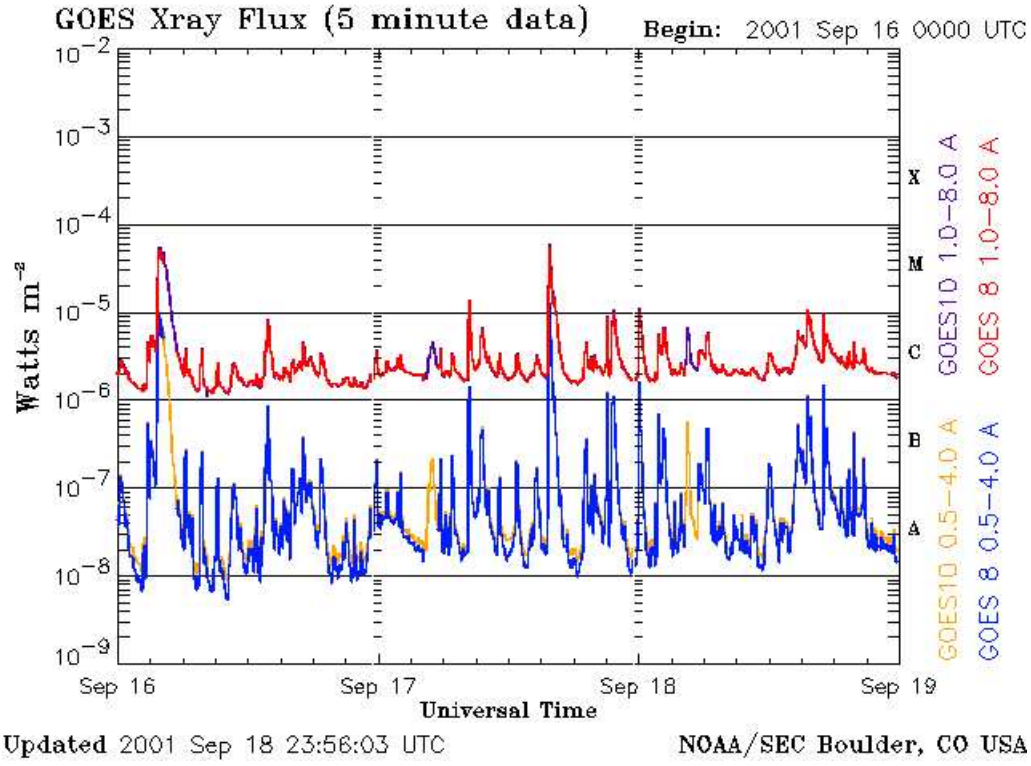

Figure 3.3: GOES plot of X-ray flux. The sizeable increase seen at 17:04 UT is due to a M 1.4 flare that erupted from AR 9628.

Data Reduction and Analysis

The CDS data were reduced by first applying a cosmic ray detection routine. Affected pixels were noted and eliminated from this study. Another procedure subtracted the a dark current and readout pedestal from the data. These applications are all part of the *Solar Soft* software package for CDS available for use with *Interactive Data Language* (IDL). We note that there is an offset between the NIS 1 and NIS 2 data coordinates (7″ in $\hat{y}$ and 2″ in $\hat{x}$), and we selected all points based upon solar Cartesian coordinates to avoid this problem. After the *SoHO* recovery in the fall of 1998, broadened Gaussian curves best characterize the intensity profiles of the emission lines observed by CDS (Haugan (2004) [36]). Instrumental contributions to line broadening are known to produce the largest contribution to line width (Haugan (2004) [36]), although the reason for this is still not well understood. Any contri-

bution to broadening resulting from gas pressure effects would produce Lorentzian tails in the profile (Bransden and Joachain (2003) [29]), and this line shape was not observed (see Figure 3.4).

The TRACE data were also calibrated using the standard techniques. A dark current image was subtracted from the data, and a cosmic ray detection routine determined the location of cosmic ray strikes on the CCD. Additionally, the TRACE images were co-aligned with both the EIT and CDS data by application of a procedure that found the limb in the images and performed cross-correlation to determine the correction to the coordinates of TRACE for co-alignment with EIT. The EIT image used for this application was taken within 1 minute of the TRACE image. Using limb identification and the cross-correlation procedure, we have determined a co-alignment from the data of these different instruments to approximately 2″. This is of order one EIT pixel.

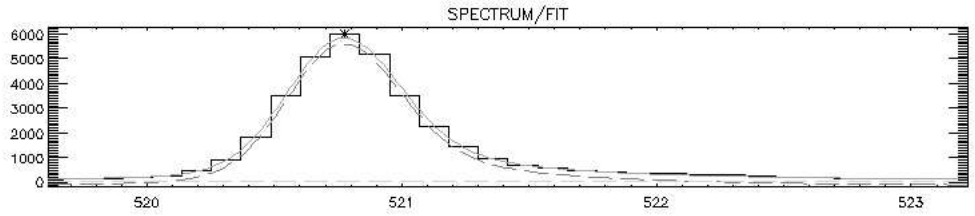

Figure 3.4: Example of the Broadened Gaussian curvefit for Si XII.

Line Intensities and Curve Fitting

Intensities, in units of erg cm^{-2} s^{-1} sr^{-1}, were calculated using the curve-fit programs written specifically for CDS data analysis. An example of one of these gaussian curve fits is shown in Figure 3.4. The spectral background continuum was determined for every passband, and this was subtracted from the line profile. Any pixel with a signal to noise ratio of less than 10 was eliminated from the analysis; the noise is assumed to be due to Poisson-random events and is characterized as the square root

of the observed photon flux. In addition to intensity, the line width and centroid wavelength were also recorded for every pixel.

The intensity was measured for 36 pixel positions along the solid radial line shown in Figures 3.1 and 3.2. The radial line was found by determining the line that passed through a point at the limb and disk center. We found pixels that were along the radial line and were the closest to constant steps in altitude. However, the CDS pixels are rectangular, longer in horizontal extent than vertical. We selected points such that subsequent steps along the radial line were an increase in altitude. As can be seen in Figure 3.2, the radial line presented here is not parallel to the loops resolved by the TRACE 173 Å filter images. Both Figures 3.1 and 3.2 include the radial line chosen as representative of all the radial lines analyzed in the study. This particular line was selected because of its proximity to the active region center, and only one of the radial segments is shown to keep this presentation short. All of the results from each of the radial line selected provide evidence supporting our conclusions. We have included the results for 4 additional radial lines, indicated by dashed lines in Figure 3.2, and note that we have not included more than this limited set as the CDS pixel size limits the number of radial lines that can be selected. We did use a total of ten lines in this work and found no result inconsistent with what we present in this thesis.

Scale Height Temperature Determination

Several different functional forms were used to find the best representation of the intensity decrease with altitude. We first used a least square fit to a straight line, where *y(h)* represents intensity, y, as a function of altitude, h,

$$y(h) = a_0 + a_1 * h \quad . \tag{3.1}$$

Here h is the height above the solar limb and a_0 and a_1 are the fit parameters. Next

we used a least square polynomial fit for a quadratic,

$$y(h) = a_0 + a_1 * h + a_2 * h^2 \quad , \tag{3.2}$$

and finally least square fit for an exponential function,

$$y(h) = a_0 * exp(-a_1 * h) \quad , \tag{3.3}$$

was attempted. We found that the exponential function was a much more accurate approximation of the decrease in intensity with altitude for all of the ions observed. For example, using the solid radial line presented in Figure 3.2, the straight line has $\chi_r^2 = 1201$, the quadratic has $\chi_r^2 = 42.91$ for Si X. The exponential fit for the same radial line has $\chi_r^2 = 8.53$. All radial lines henceforth presented show a similarly great disparity in reduced chi-squared values, making the exponential fit the clear choice in every case.This is true for all radial lines presented henceforth. We then compared the calculated exponent for each of the ions to the exponent derived for the emission measure scale height. This is known to be of the form,

$$EM(h) = EM(0) * exp(-\frac{h * \mu m_H * g_{sun}}{k_B * T_e}) \tag{3.4}$$

Here h is the altitude above the limb, μ is the molecular weight ≈ 0.62, m_H is the mass of hydrogen, g_{sun} is the solar gravity term ($274\ \frac{m}{s^2}$), k_B is Boltzmann's constant, and T_e is the electron temperature. EM(0) is assumed to be the emission measure at the base of the corona (see Chapter 2 for the derivation). We have allowed the least square curve fit program to determine the value of the two parameters in our curve fit, a_0 and a_1 from Equation 3.3, and used these to calculate the inferred temperature for the scale height. For all of the radial lines presented in Figures 3.6-3.15, we have listed the observed emission measure scale height temperature derived from the data.

In equation 3.3, the value a_1 is assumed to equal λ^{-1}, where

$$\lambda = (\frac{k_B * T_e}{\mu m_H * g_{sun}}) \quad . \tag{3.5}$$

The parameter λ is the hydrostatic emission measure scale height. It should be noted that the same radial line was used for each of the data sets. If we had selected different radial lines for each of the five CDS data sets analyzed it would not be clear that we measured the same portion of the AR and a valid comparison of the results found for each of the data would not have been straightforward.

The final step in this analysis is to determine the contribution to total intensity from resolved loops that intersect the radial line, and to subtract this value for loop intensity from the total intensity. It is important to realize that we are suggesting that the emission from unresolved structures is most likely due to loops below the resolution of both CDS and TRACE. To perform this analysis we use the following steps:

1. Using TRACE images taken at the same times as each of the CDS exposures, a composite image was constructed. This image simulates the compiled exposures of CDS that are used to form a CDS raster image. For every CDS 4″slit position, the portion of the TRACE image co-spatial and co-temporal with the slit were cut out of the TRACE image and combined to form a TRACE 'raster' image. Each of the TRACE images contained in the composite are then analyzed to determine the locations along the radial line where loops were visible. A list of the radial line pixel positions containing visible loop segments is generated.

2. We find the loop cross-section from the TRACE data, and the profile of a loop or a group of loops is identified in the image as a feature that is less than 15 data points in width (each pixel represents 350 km on the sun), yet greater than 2 pixels, and more than 25 data points in distance along the cross-sectional axis of the loop,

s. The limitation on the width was necessary to distinguish a resolved loop from a set of structures juxtaposed in an image. We found the criteria listed to be a fair representation of structures commonly called coronal loops.

3. The CDS pixels corresponding to TRACE loop locations are modified to correct for the increase in intensity from the resolved loop. This is done by calculating the average intensity of CDS pixels near the affected pixel, but not containing a TRACE identified loop.

4. We then create a profile from the intensities measured along a radial line by the procedure outlined above. The resulting profiles are shown in Figures 3.11 - 3.15 for the same radial line represented by Figures 3.6 - 3.10.

ION	T_{bf} (MK) 15:39 UT	χ^2_r	χ^2_r LS	T_{bf} (MK) 16:47 UT	χ^2_r	χ^2_r LS	T_{bf} (MK) 17:56 UT	χ^2_r	χ^2_r LS
Si X	1.4	8.53	4.61	1.6	5.42	2.79	2.1	6.07	3.08
Mg IX	1.3	2.31	2.29	1.5	7.23	5.48	1.9	8.47	4.22
Mg X	1.9	2.19	2.05	2.1	2.10	10.3	2.4	2.51	2.50
Fe XIII	2.5	4.06	2.87	2.1	3.61	7.02	3.0	3.67	2.43
Si XII	2.1	2.50	2.11	2.3	1.78	3.41	2.5	1.72	1.72
Fe XVI	2.1	1.99	1.98	2.4	1.50	1.33	2.4	1.68	1.68
	T_{bf} (MK) 19:05 UT	χ^2_r	χ^2_r LS	T_{bf} (MK) 20:14 UT	χ^2_r	χ^2_r LS			
	2.2	2.98	2.30	2.0	2.07	1.74			
	1.8	2.77	1.91	1.7	2.47	2.61			
	2.2	2.01	2.00	2.2	1.29	1.29			
	2.6	7.82	9.64	2.9	2.13	1.85			
	2.5	1.42	1.42	2.2	1.37	1.37			
	2.2	1.38	1.38	2.3	1.25	1.25			

Table 3.2: Best fit temperature for intensity along the solid radial line shown in Figures 3.1 and 3.2. LS stands for Loop Subtracted intensities.

The reduced χ^2 values given in Table 3.3 for the unresolved intensity profiles indicate that the scale height approximation (Equation 3.4) is a good fit to the decrease

	Line 2		Line 3		Line 4		Line 5	
	T_{bf}	χ^2_r	T_{bf}	χ^2_r	T_{bf}	χ^2_r	T_{bf}	χ^2_r
Si X	1.3	8.53	1.4	6.12	1.0	2.97	1.0	2.64
Mg IX	1.4	3.65	1.4	4.12	1.2	3.49	1.2	2.41
Mg X	1.6	1.99	1.8	2.52	1.7	3.54	1.9	2.73
Fe XIII	1.9	5.88	1.9	8.50	2.2	7.68	2.5	5.19
Si XII	2.0	2.21	2.0	2.84	2.1	2.19	2.2	1.80
Fe XVI	2.0	1.87	2.1	2.34	2.0	1.97	2.1	1.45

Table 3.3: Best fit temperature for intensity along the dashed radial segments in Figure 3.2 that are numbered from top to bottom in Figure 3.2. LS stands for Loop Subtracted intensities. Data is from the CDS raster beginning 15:39:11 UT.

in intensity for all of the ions - better than for any other function we attempted to fit to the data. The associated temperatures for these ions are near their peak formation temperatures. The error bars in Figures 3.6 - 3.15 include the Poisson uncertainty in the intensities, the error associated with the Gaussian curve fits, and the error in the exponential curve fits. These have been added in quadrature as they are all independent sources of error.

There are faint structures in Figure 3.2 (indicated using arrows in the figure) that are nearly parallel to the radial line. To make this clear Figure 3.5 has been included with arrows pointing to examples of these faint unresolved structures. These structures are not considered resolved loops by the criterion listed in step 2, since they cannot be resolved into stand-alone features. Moreover, their intensity is only 1.5 times the intensity of the surrounding background, so their inclusion would have no measurable effect on the exponential fit. Figure 3.5 demonstrates this separation between resolved and unresolved structures. The TRACE 173 Å image has been rotated into a three dimensional image where the $\hat{z}$ axis is Dn/s; here *Dn* is data numbers. The arrows point to unresolved coronal structures. Unresolved structures can be spatially indiscernible because of insufficient counts relative to the Poisson background or other structures in close proximity. In either instance it is these unresolved structures

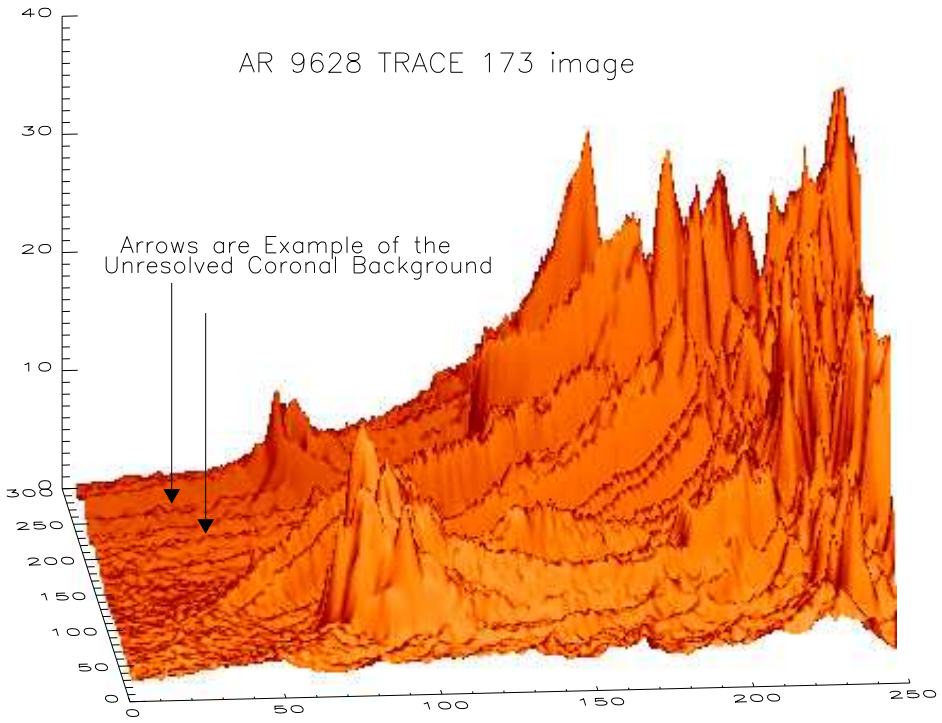

Figure 3.5: TRACE 173 Å image shown in 3-D. Image includes two arrows indicating unresolved coronal structures. The image was taken at 18:34 UT on 18 Sept 2001.

that are being investigated.

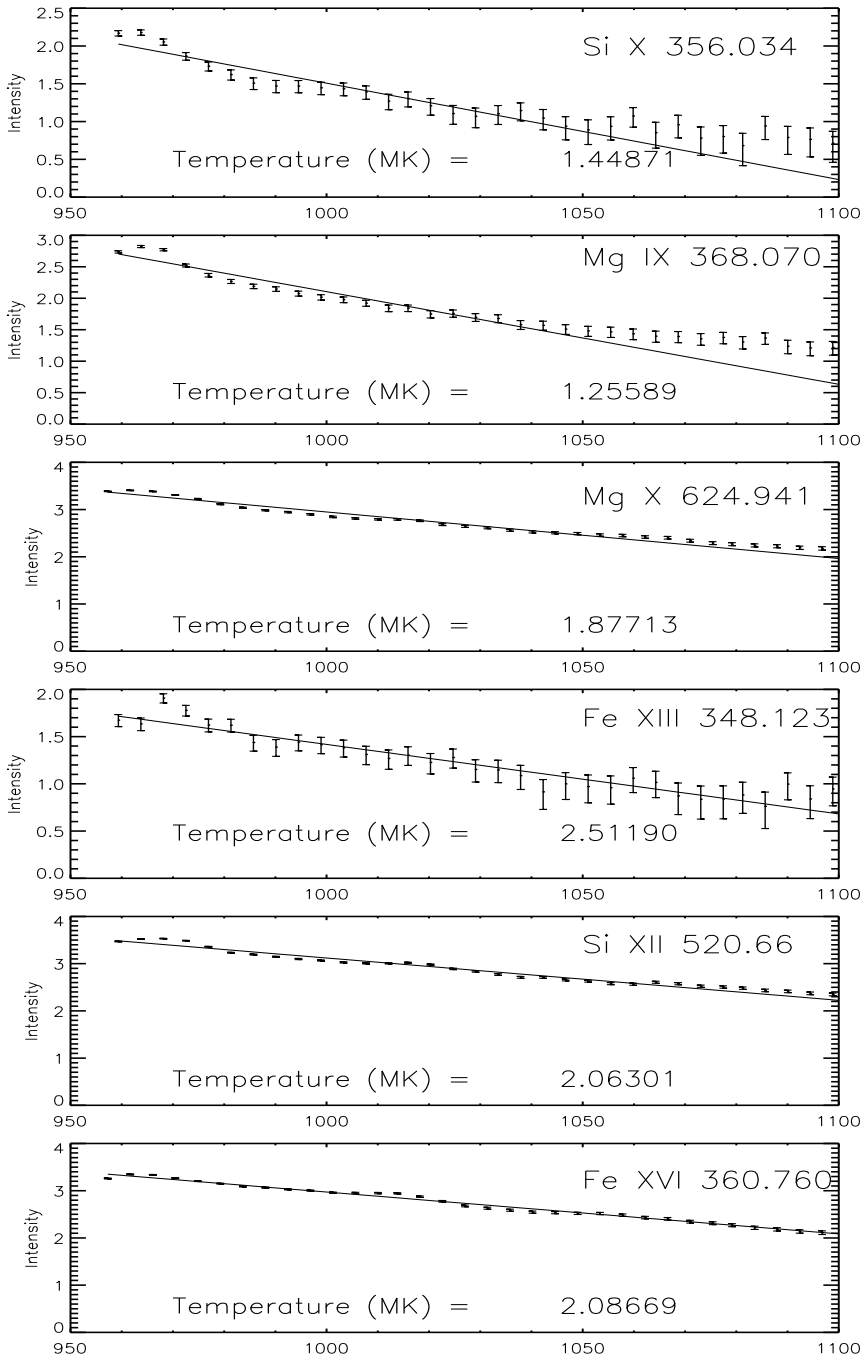

Figure 3.6: CDS intensities plotted as a function of distance along the solid radial line shown in Figures 3.1 and 3.2. Data is from raster scan starting at 18 Sep 2001 15:39:11.201 UT. Intensities are in units $\log_{10}$ ergs s^{-1} cm^{-2} and the distances (x axis) are given in arcseconds. One arcsecond is approximately 700 km on the Sun.

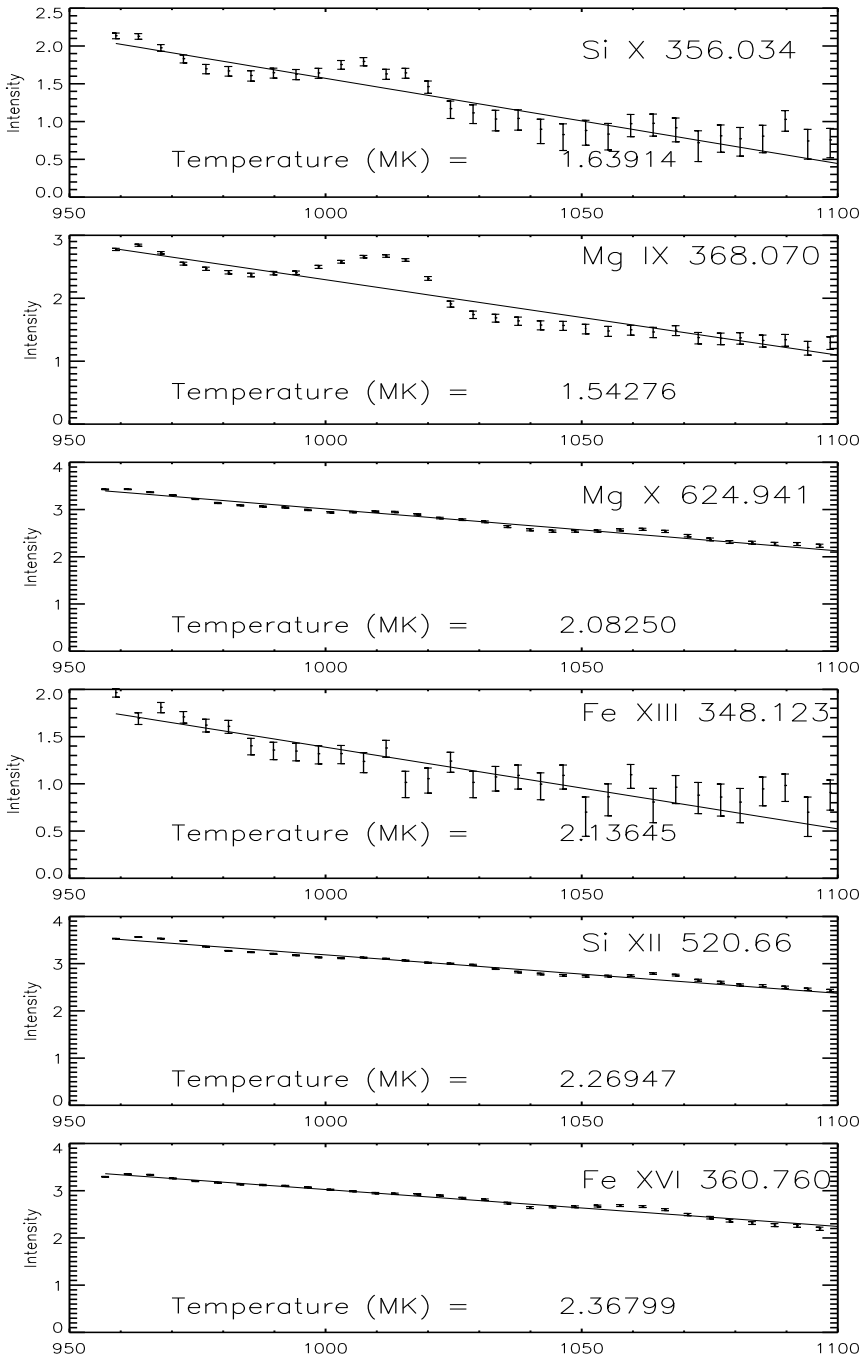

Figure 3.7: CDS intensities plotted as a function of distance along the solid radial line shown in Figures 3.1 and 3.2. Data is from raster scan starting at 18 Sep 2001 16:47:33.447 UT. Intensities are in units $\log_{10}$ ergs s^{-1} cm^{-2} and the distances (x axis) are given in arcseconds. One arcsecond is approximately 700 km on the Sun.

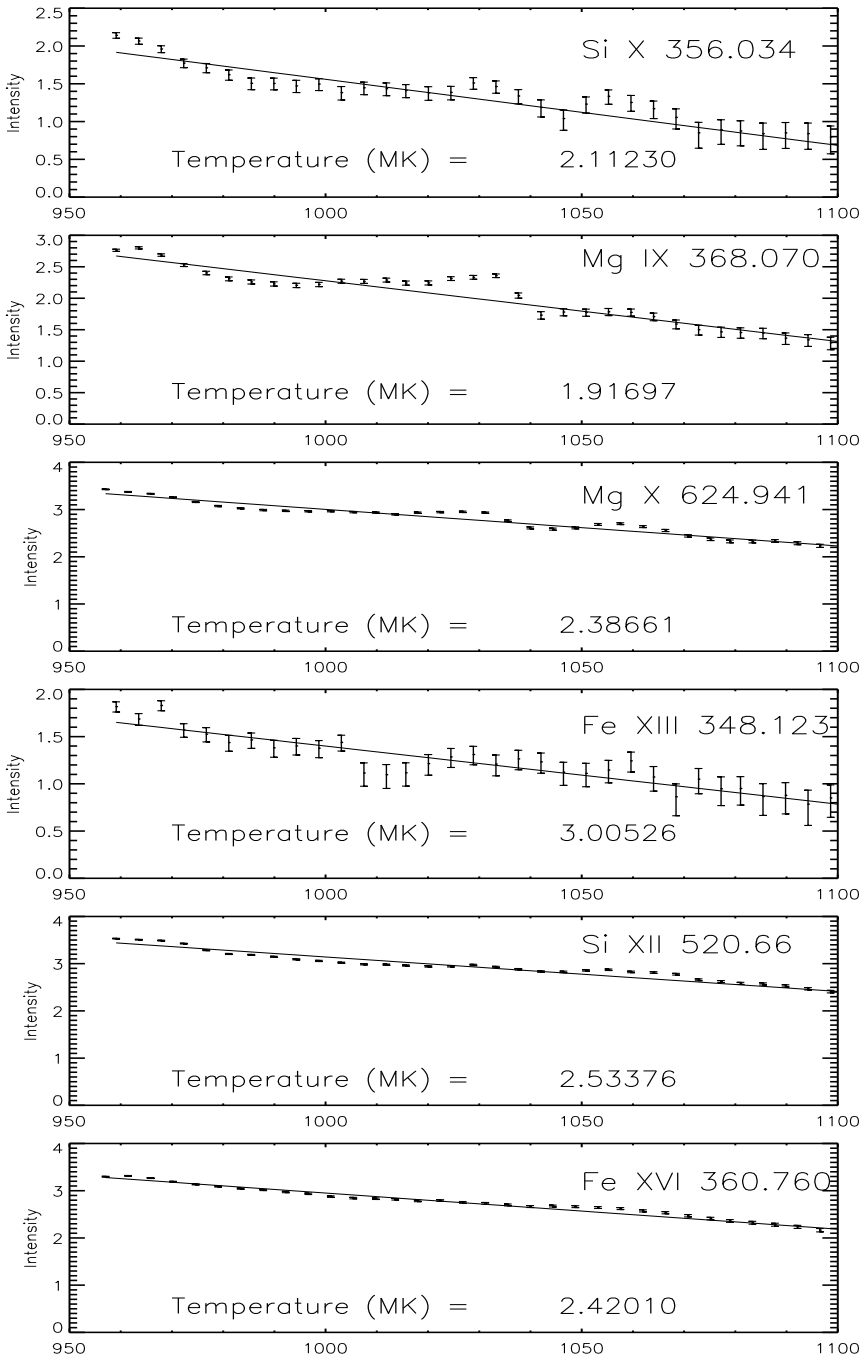

Figure 3.8: CDS intensities plotted as a function of distance along the solid radial line shown in Figures 3.1 and 3.2. Data is from raster scan starting at 18 Sep 2001 17:56:37.727 UT. Intensities are in units $\log_{10}$ ergs s^{-1} cm^{-2} and the distances (x axis) are given in arcseconds. One arcsecond is approximately 700 km on the Sun.

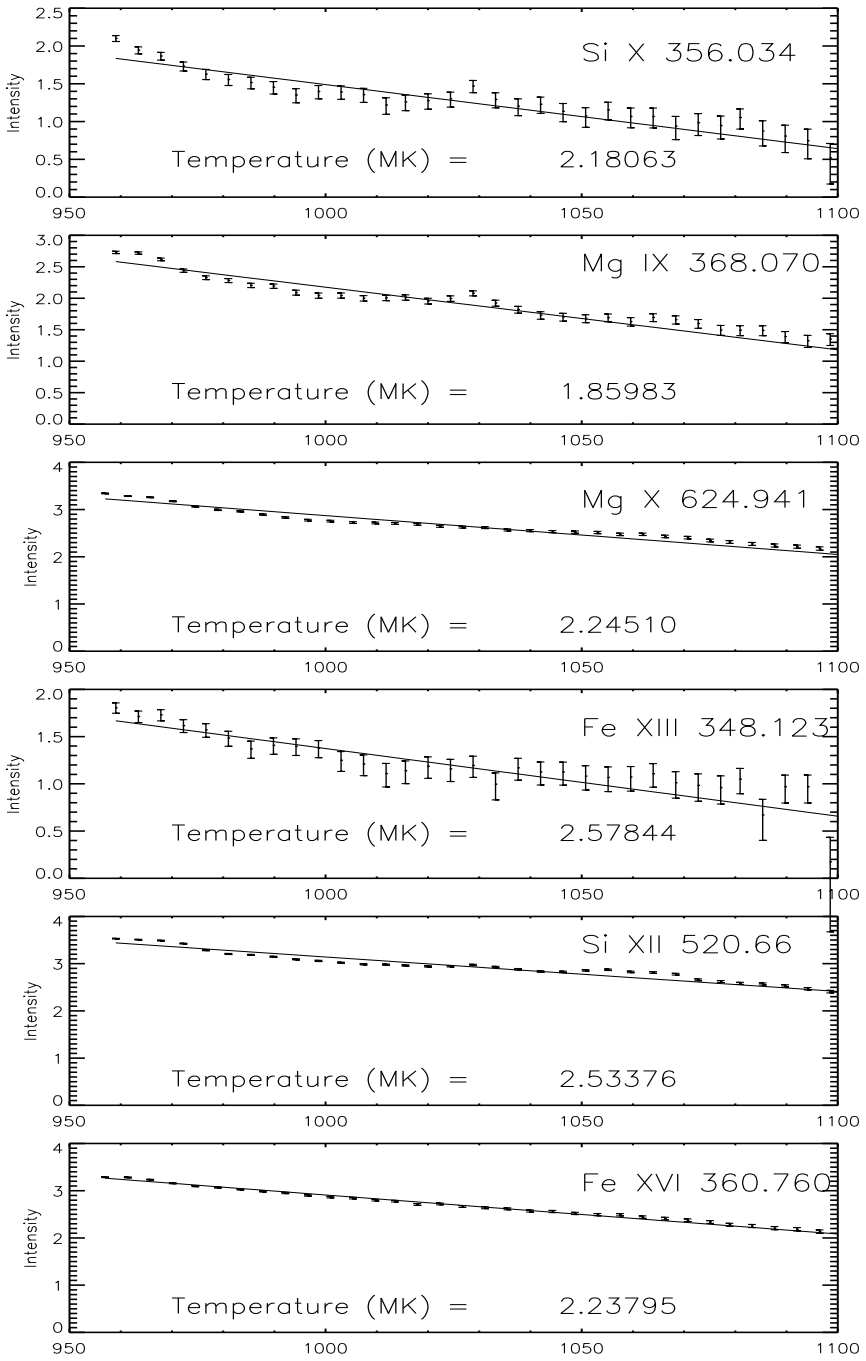

Figure 3.9: CDS intensities plotted as a function of distance along the solid radial line shown in Figures 3.1 and 3.2. Data is from raster scan starting at 18 Sep 2001 19:05:47.163 UT. Intensities are in units $\log_{10}$ ergs s^{-1} cm^{-2} and the distances (x axis) are given in arcseconds. One arcsecond is approximately 700 km on the Sun.

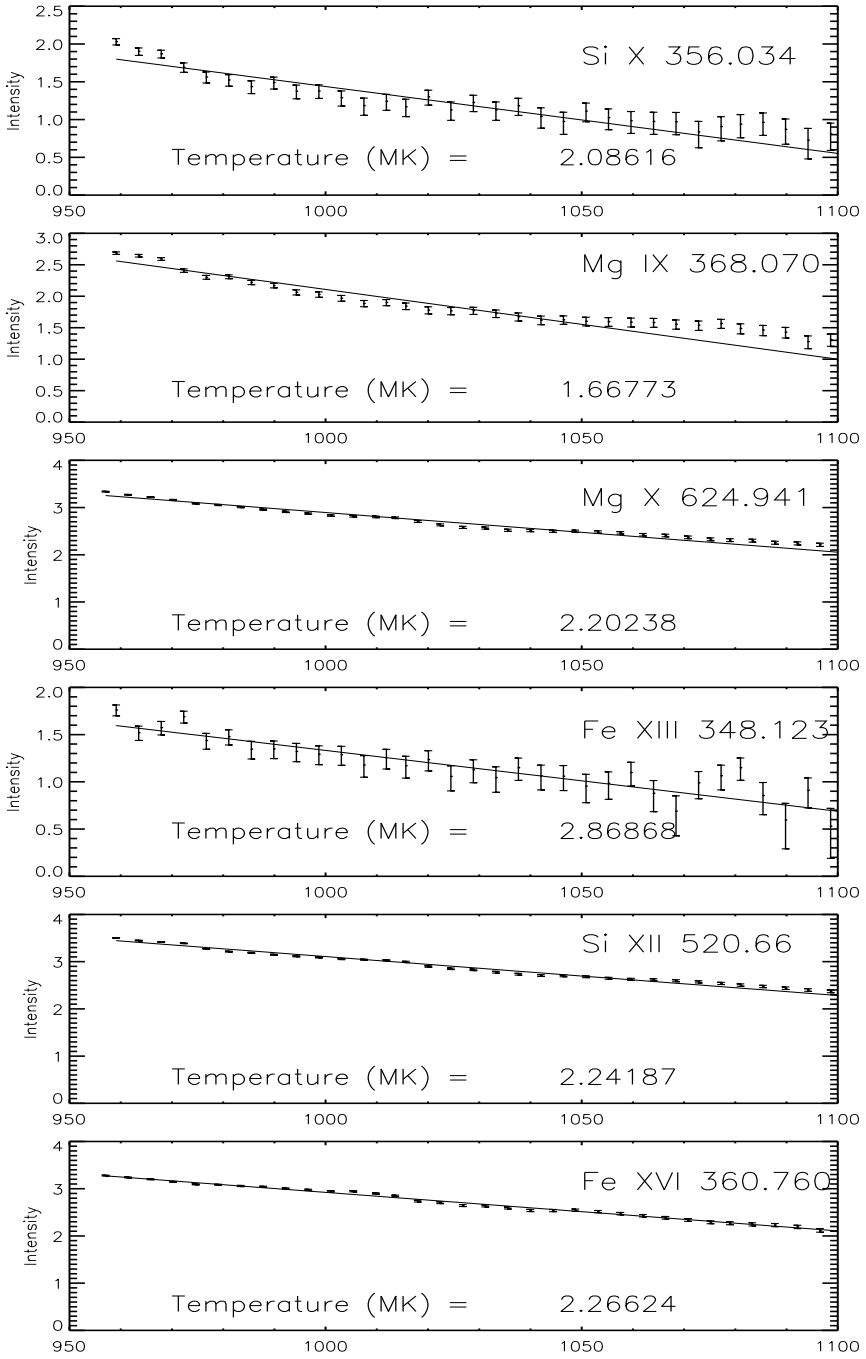

Figure 3.10: CDS intensities plotted as a function of distance along the solid radial line shown in Figures 3.1 and 3.2. Data is from raster scan starting at 18 Sep 2001 20:14:55.803 UT. Intensities are in units $\log_{10}$ ergs s^{-1} cm^{-2} and the distances (x axis) are given in arcseconds. One arcsecond is approximately 700 km on the Sun.

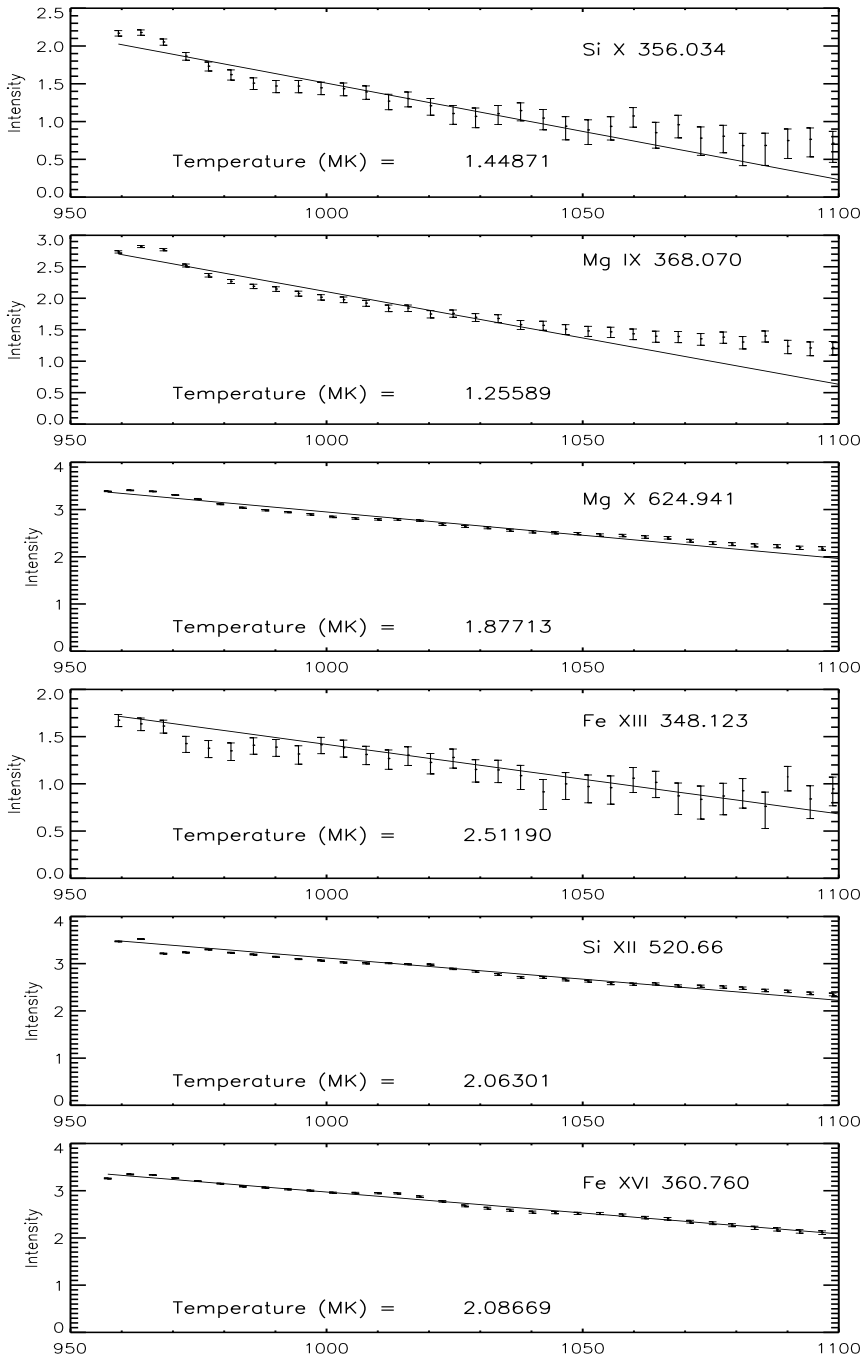

Figure 3.11: Loop subtracted CDS intensities plotted as a function of distance along the solid radial line shown in Figures 3.1 and 3.2. Pre-subtraction results are in Figure 3.6. Intensities are in units $\log_{10}$ ergs s^{-1} cm^{-2} and the distances (x axis) are given in arcseconds. One arcsecond is approximately 700 km on the Sun.

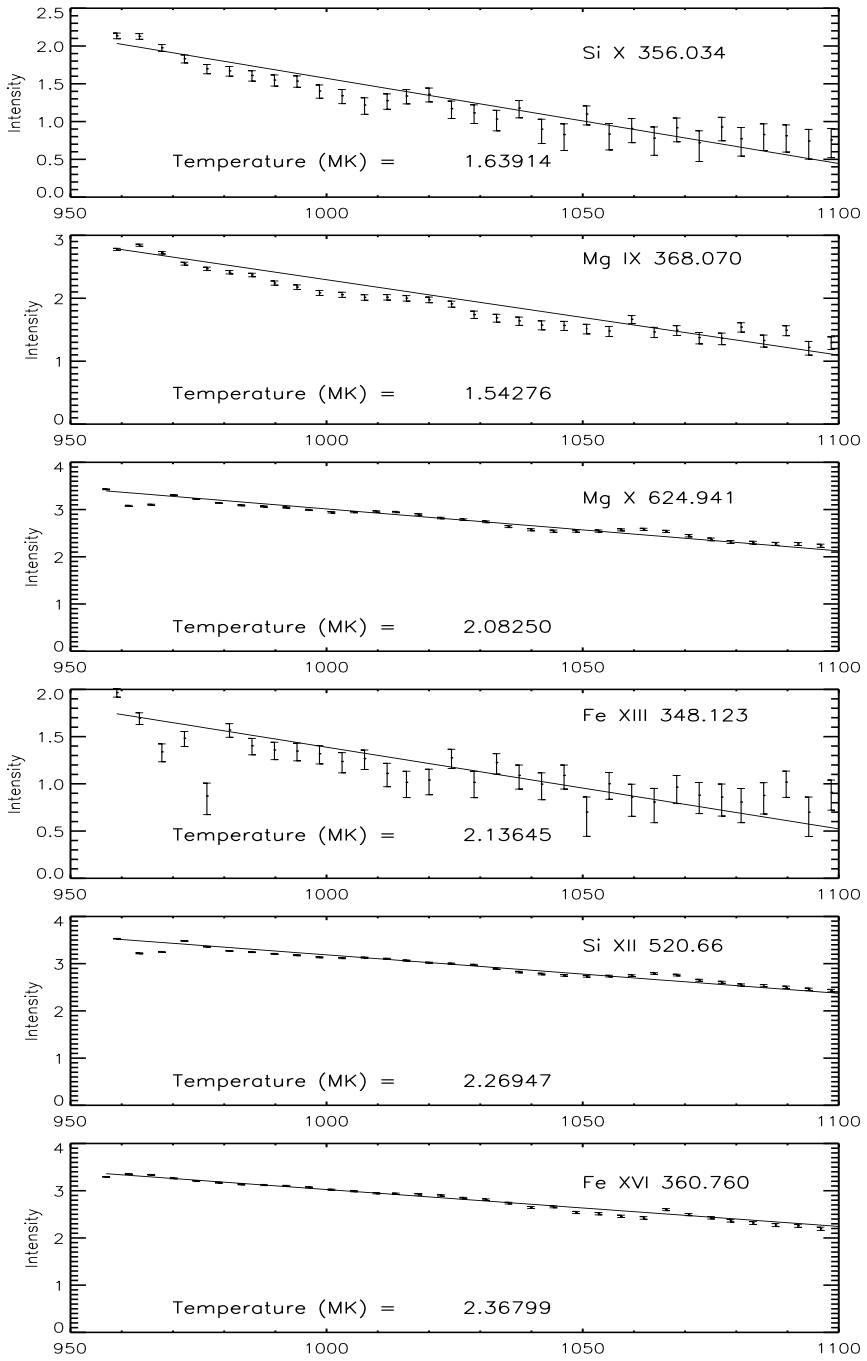

Figure 3.12: Loop subtracted CDS intensities plotted as a function of distance along the solid radial line shown in Figures 3.1 and 3.2. Pre-subtraction results are in Figure 3.7. Intensities are in units $\log_{10}$ ergs s^{-1} cm^{-2} and the distances (x axis) are given in arcseconds. One arcsecond is approximately 700 km on the Sun.

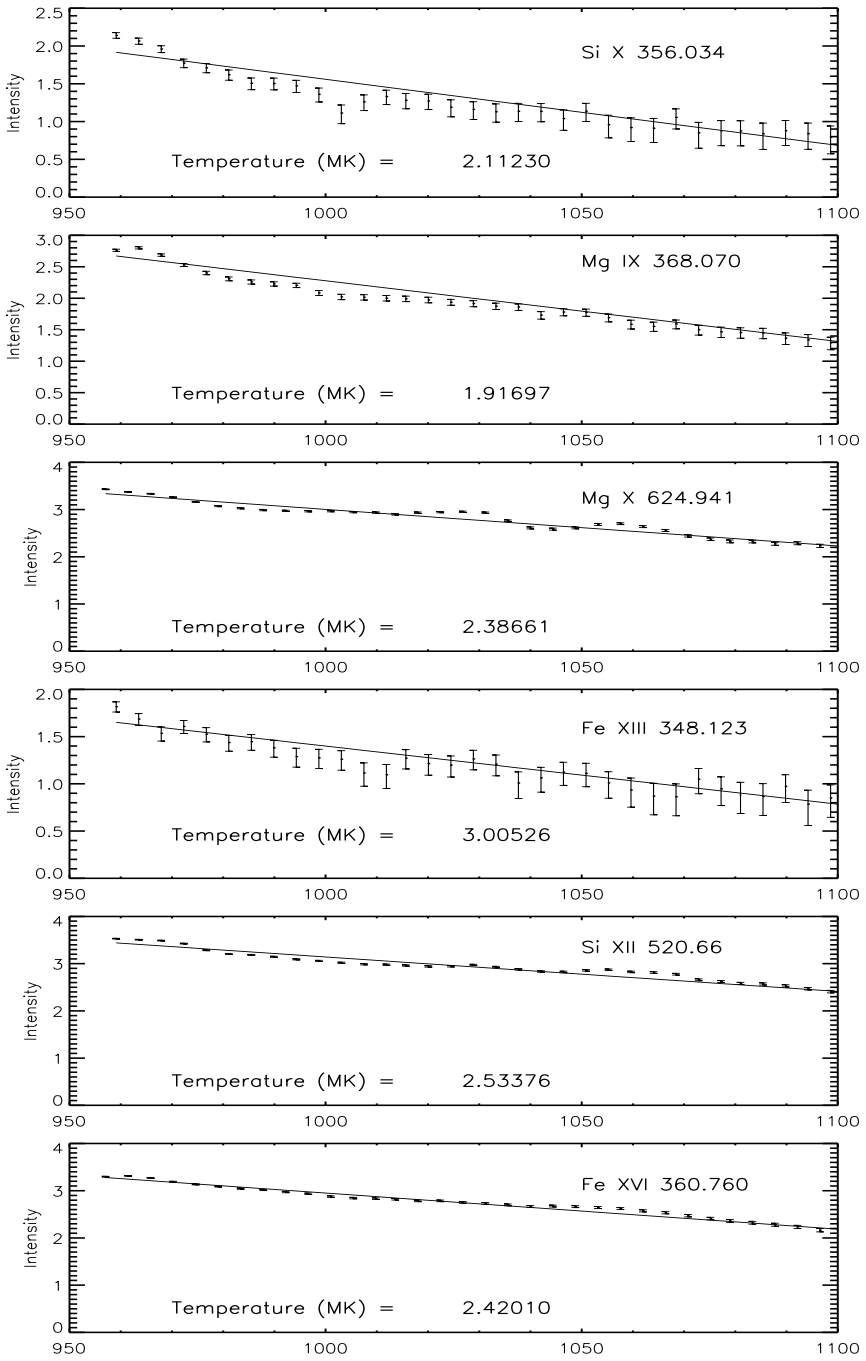

Figure 3.13: Loop subtracted CDS intensities plotted as a function of distance along the solid radial line shown in Figures 3.1 and 3.2. Pre-subtraction results are in Figure 3.8. Intensities are in units $\log_{10}$ ergs s^{-1} cm^{-2} and the distances (x axis) are given in arcseconds. One arcsecond is approximately 700 km on the Sun.

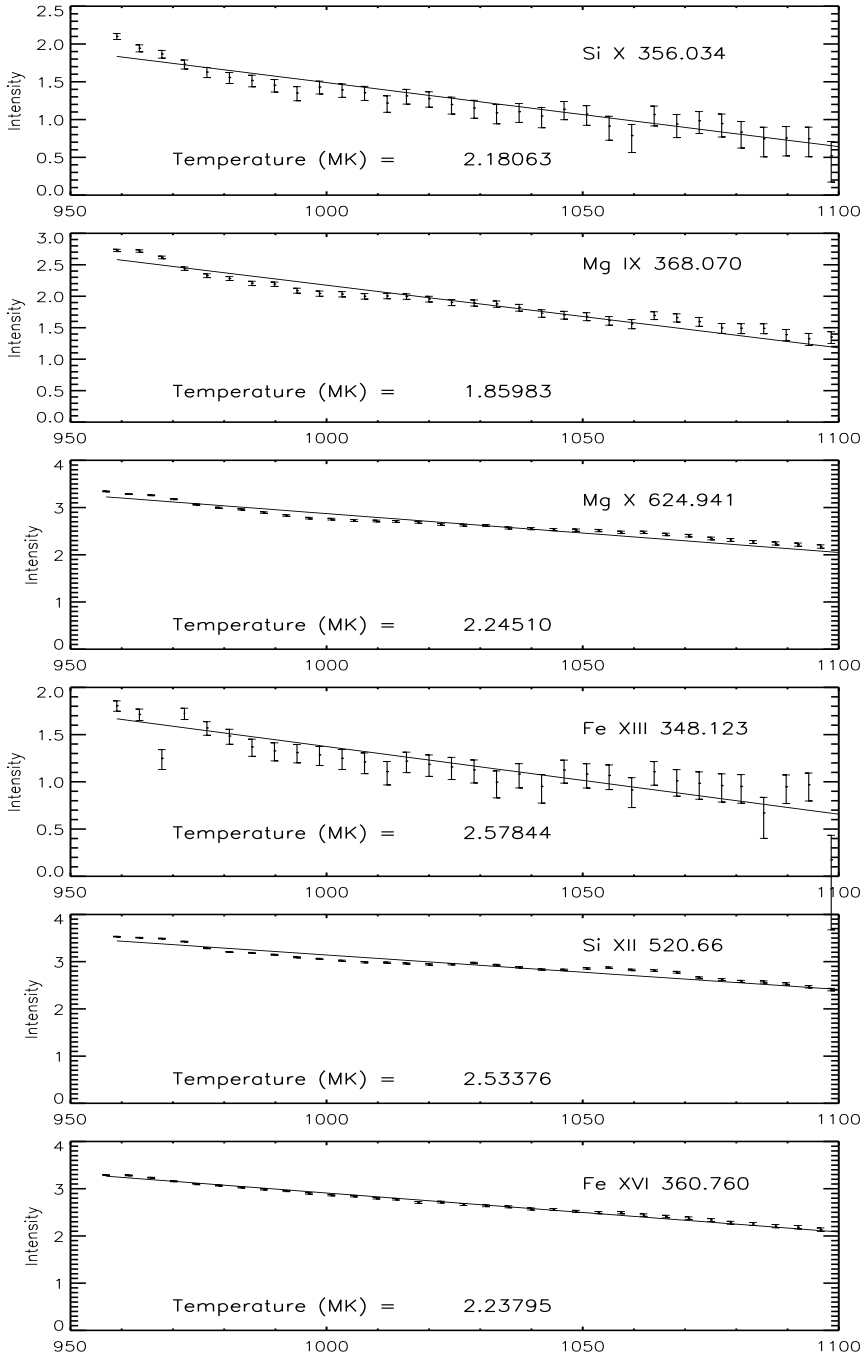

Figure 3.14: Loop subtracted CDS intensities plotted as a function of distance along the solid radial line shown in Figures 3.1 and 3.2. Pre-subtraction results are in Figure 3.9. Intensities are in units $\log_{10}$ ergs s^{-1} cm^{-2} and the distances (x axis) are given in arcseconds. One arcsecond is approximately 700 km on the Sun.

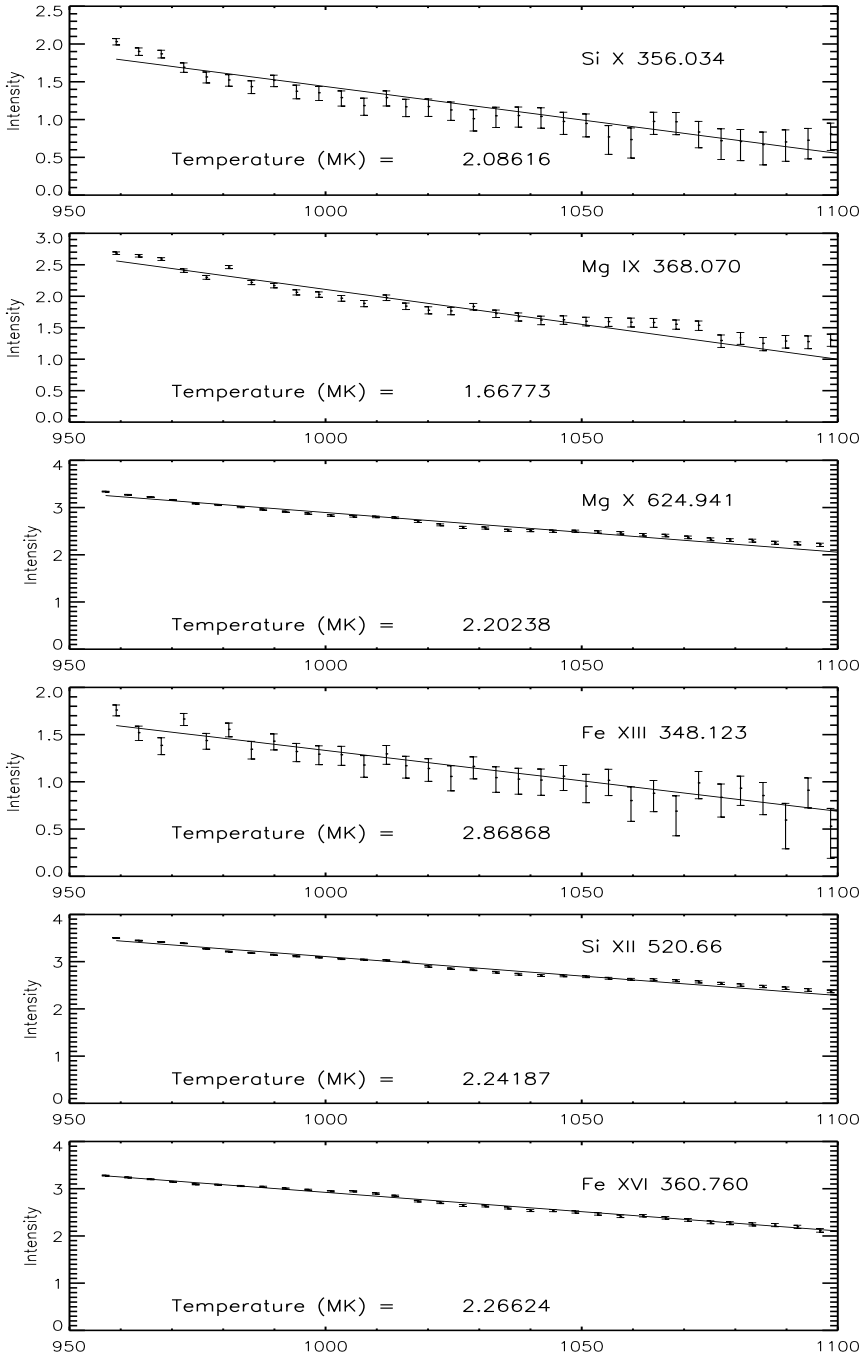

Figure 3.15: Loop subtracted CDS intensities plotted as a function of distance along the solid radial line shown in Figures 3.1 and 3.2. Pre-subtraction results are in Figure 3.10. Intensities are in units $\log_{10}$ ergs s^{-1} cm^{-2} and the distances (x axis) are given in arcseconds. One arcsecond is approximately 700 km on the Sun.

Results

Figures 3.6 - 3.15 show that, at the resolution of CDS, the majority of the total emission from the corona above an active region is from the unresolved background. Structures along the line of sight only account for a small fraction of the total observed emission, a result in agreement with Del Zanna and Mason (2003)[32]. Subtracting the intensity of the background emission from the combined emission of a structure and background indicates that, for pixels near the limb, or above 20 Mm, the background constitutes a majority of the total intensity. This background emission can be accurately characterized by using hydrostatic scaling with a temperature approximately equal to the peak formation temperature of the ion for this active region. The combination of our result that the emission due to unresolved coronal structures is best characterized by hydrostatic scaling laws and the statement first made by Del Zanna and Mason (2003) [32] requires any model of solar coronal AR emission account for these observations. We have also proven that statement by Del Zanna and Mason (2003)[32] independently using CDS observations; they did not have this opportunity.

We have found that the total of the unresolved emission for TRACE images is also larger than the total contribution to flux from resolved structure emission. We have also noticed that the percentage of the total attributable to the unresolved background is a function of the activity of the AR. For post-flare ARs like AR 9628, the contribution from the unresolved structures is a larger fraction of the total flux of the AR than the loop contributions. For non-flaring ARs the 173 Å passband may be mostly O VI and Fe IX emission. These ions have scale heights below 30 Mm and would not exist high in the corona. As such, images of these ARs would only show the locations of hydrodynamically evolving loops, and the static background would be nearly absent. The TRACE unresolved background is a current research topic for

us and we plan to perform a detailed analysis of TRACE full disk mosaics taken over the last 7 year to determine the consistency of this finding.

A previous study by Warren (1999) [37] using SoHO's Solar Ultraviolet Measurements of Emitted Radiation (SUMER) instrument [38] and TRACE computes line intensities as a function of height for TRACE 173 Å and 195 Å images. In Figure 4 of their paper the intensity decreases exponentially with height, in agreement with our results. In their paper, they determine that the temperatures and emission measures found via filter ratio technique with the TRACE data are lower than those determined by the EM loci technique using the SUMER data. They conclude that this could be the result of either inaccurate ionization balance calculations for Fe IX and Fe X, inaccurate collision rates for the emission lines, or possibly a combination of both. This conclusion is supported by the temperatures and emission measures calculated with line ratios of the Fe IX and Fe X lines observed with SUMER. The study of Warren (1999) [37] used data collected on the quiet sun. In Table 3.2 we note the best fit temperature for the Si X line available in our data which is formed over the same temperature range as the Fe IX and Fe X lines. This is approximately the temperature found by Warren (1999) [37]. We speculate that this result is due to the underlying 1.3 MK corona, present everywhere within regions of locally closed field. The multi-thermal background in the AR is the result of cooling in the aftermath of the flare, and the range in the temperatures that are necessary to describe the observations is also affected by the dynamic evolution of the AR.

Discussion

The curve-fits for the intensities as a function of height (Figures 3.6 - 3.15) indicate that the corona above the flaring AR in these observations is best described by $T_{fit} = T_{pf}$ for $T \geq 1$ MK before the flare; here T_{pf} is the peak formation temperature of the ion. After the flare, the best fit scale height temperature increases sharply, nearly

50% for all lines observed, and then slowly returns to approximately its starting value after 2.5 hours have passed. The small error in the curve-fits indicates it is likely that there is a hydrostatic corona present in regions of locally closed field. This static AR corona has several interesting characteristics. The M 1.4 flare was first recorded by the GOES 8 satellite at 17:04 UT; it peaked 4 minutes later in X-rays. The flare's peak flux measured by TRACE was 3 minutes later at 17:12 UT. In Figure 3.9, a pronounced increase in the intensity of the Mg IX and Si X lines is evidence of material that was ejected during this event. In spite of this flare, the corona does not appear to depart significantly from hydrostatic equilibrium since the plots of the intensity versus altitude are still well fit with an exponential. The scale height temperature decreases in the three observations directly following the flare. The exponential trend for intensity from ions formed above 1 MK shows clearly that the emission decreases as required for a hydrostatic scaling law to apply. After subtraction of the loop contribution to intensity the curve fit χ^2 are improved moderately.

Another observed property of this static corona is that it constitutes the bulk of coronal EUV emission. Although resolved structures exhibit a higher intensity when compared to the unresolved corona, these are local phenomena that do not fill a substantial fraction of the coronal volume in the AR. However, the unresolved corona fills this coronal volume, and the fact that there is a *measurable contribution to intensity for any line-of-sight through the volume* is highly suggestive of the dominance of the unresolved corona in total radiative energy for the AR. As a result, any flare heating model must account for this observation and allow for dynamic activity observed at low altitudes. Additionally, the corona of the quiet sun has an emission measure scale height temperature of 1.3 MK [37]. The unresolved corona is most-likely composed of loop-like structures, and these unresolved loops could connect between active regions, or to flux elements in quiet sun regions. These interconnecting loops would of course

be very long and, given enough of them through any volume element along the line of sight, could explain the "diffuse" appearance of the corona in images taken with the 195 Å and 284 Å filters of TRACE and EIT (see Figures 3.23 and 3.24). This idea is supported by the work presented here and would explain the diffuse nature of the high corona. The result which finds the decrease in intensity as a function of altitude approximates the exponential decrease indicative of a hydrostatic atmosphere is a new observation. However, the result that most EUV emission from AR's is from the unresolved corona was first found by Del Zanna and Mason (2003) [32] using TRACE data. We have solidified this result by direct observation using to independent instruments, TRACE and CDS. Moreover, this result passes the common sense test: TRACE EUV loop pixels are typically only a factor 2 or 3 brighter than the surrounding pixels. In an AR image there are many more background pixels than loop pixels (otherwise one could not distinguish the individual TRACE loops), and hence the integrated total AR background emission must surpass the integrated loop emission (80% to 20% in our analysis).

Although it was stated earlier that SXT observations were available during the TRACE and CDS observing times, we did not use this data in the determination of the unresolved coronal background. We wanted to characterize the EUV background, and the primary emission SXT observes is X-rays. However, we did inspect the SXT data and noticed something peculiar that was already known from previous studies such as Porter and Klimchuk (1995) [35]. The contribution to flux in the SXT data is primarily due to emission from structures, and even though the resolution of SXT may cause the structure to look slightly diffuse, it is still resolved against the background and has a much larger value for flux than the ambient background. This is in direct contrast to the EUV data studied here and investigations carried out by many other authors. We have found that the diffuse corona in EUV has a peak intensity

near 1.3 MK, and it also has substantial emission from ions both above and below this temperature which seem to be in hydrostatic equilibrium. However, the emission decrease as a function of temperature could explain why there is little background contribution to flux recorded by SXT in X-rays. The temperature response of SXT is low at the 1.3 MK temperatures and does not reach a peak signal as a function of temperature until 3 MK. As such, SXT would not detect the emission from sources within the unresolved EUV corona, but would detect the loops described by Porter and Klimchuk (1995)[35]. In summary, SXT images do not follow the same exponential trends as EUV images, a key example of the temperature dependence of the result and for the AR heating mechanism in general.

Results from the study of the unresolved emission characteristics above other active regions has indicated that: for flaring ARs, there is a multi-thermal background with a range in temperatures for the scale heights which appears to be dependent upon the strength of the flare and the length of time that has passed after the flare occurred. For non-flaring ARs there is a isothermal unresolved corona where the majority of the unresolved emission is from a plasma with a scale height temperature slightly larger than 1 MK. We have begun a survey of numerous ARs to develop a statistical sample.

Conclusions

The previous section is an analysis of the CDS spectral scans in an active region at the limb. We have measured the spectral line intensities as a function of distance above the limb. Using the results of these analyses we have found the following:

1. The unresolved coronal background for a post-flare active region cannot be approximated by a single temperature. It is indeed multi-thermal, and for each line that we analyzed formed above 1 MK, the coronal background falls off exponentially with the scale-height temperature approximately equal to the peak formation temperature

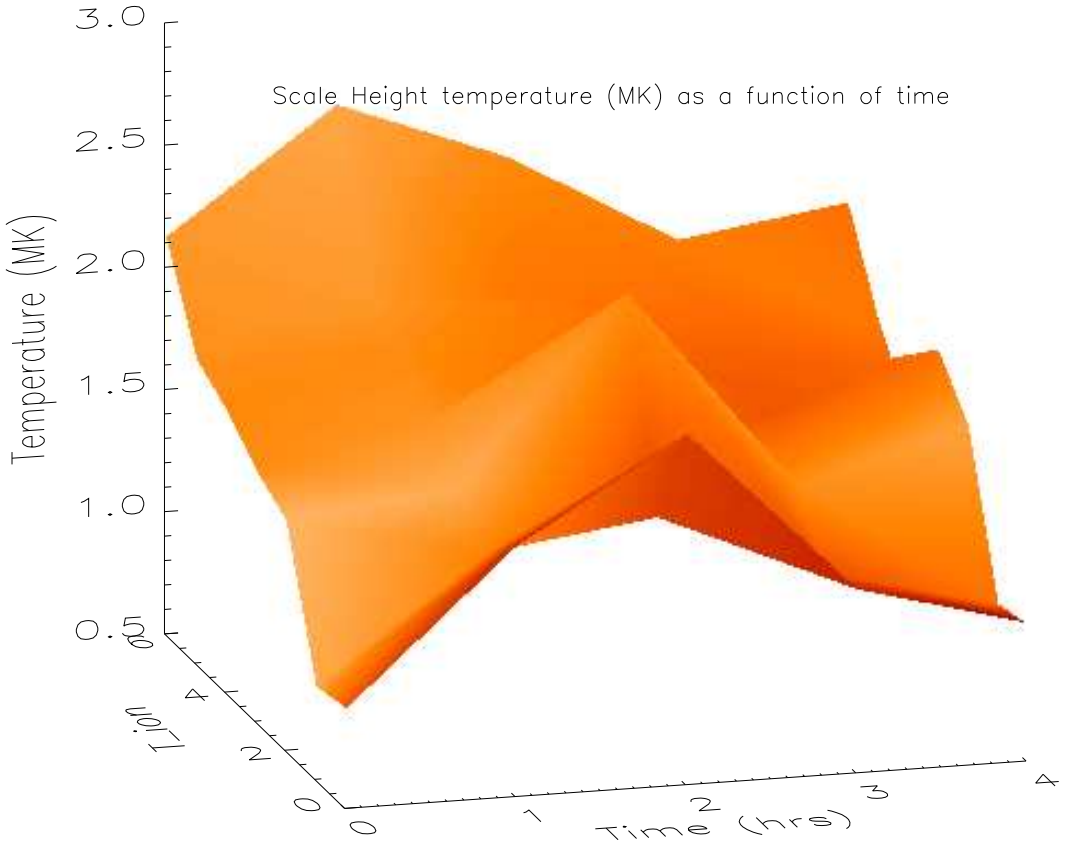

Figure 3.16: The scale height temperature as a function of time for AR 9628. The x axis is time in hours, the y axis lists the ions in order of peak formation temperature, and the z axis is the observed scale height temperature. The large increase in the scale height temperatures is coincident with the onset of the flare.

of the ion. These temperatures range from 0.9 to 2.2 MK.

2. The coronal unresolved EUV emission is by far the majority contributor to total EUV emission above active regions. This is apparent from Figure 3.18. It should be considered by those evaluating the temperature and density of EUV structures so that a more accurate estimate of these physical properties of the plasma can be made.

The Atmospheric Imaging Array (AIA) on the Solar Dynamics Observatory (SDO) can verify this result. This telescope will have seven EUV passbands, and a FOV large enough to encompass the entire solar disk and the corona below 200 Mm. Images from

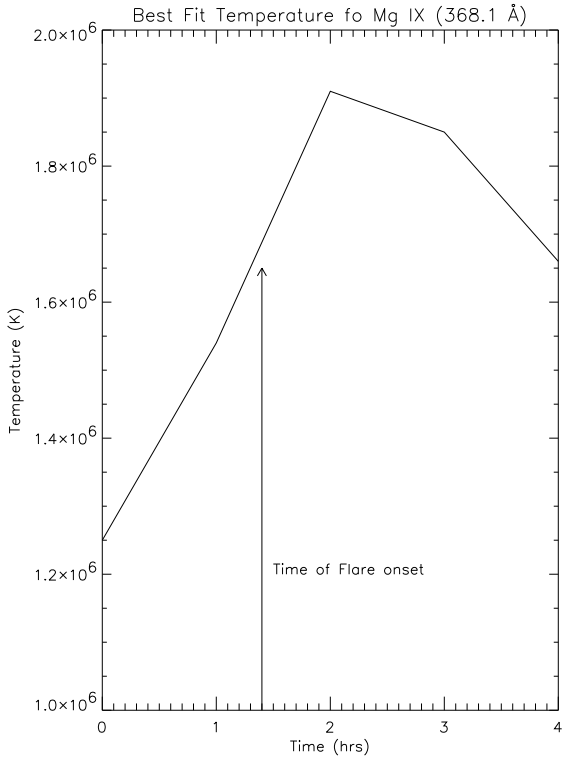

Figure 3.17: The scale height temperature as a function of time for AR 9628 using Mg IX (368.070 Å). The x axis is time in hours and the y axis is the observed scale height temperature. The large increase in the scale height temperatures is coincident with the onset of the flare as indicated by the arrow.

this device should show an increasing number of coronal structures as the dominant ion in the passband is formed at increasingly higher temperatures. The spatial resolution of this device is TRACE-like, and the temporal resolution is a factor of 10 better. This should permit better characterization of these ubiquitous coronal features, but resolving these structures will require an instrument of capable of resolving structures an order of magnitude (or more) smaller than current imaging devices permit.

Active Region 10001

During the second JOP 146 campaign, SoHO Campaign 6873, observations of AR 10001 were made as the AR rotated into view. On June 13, 2002 the AR footpoints

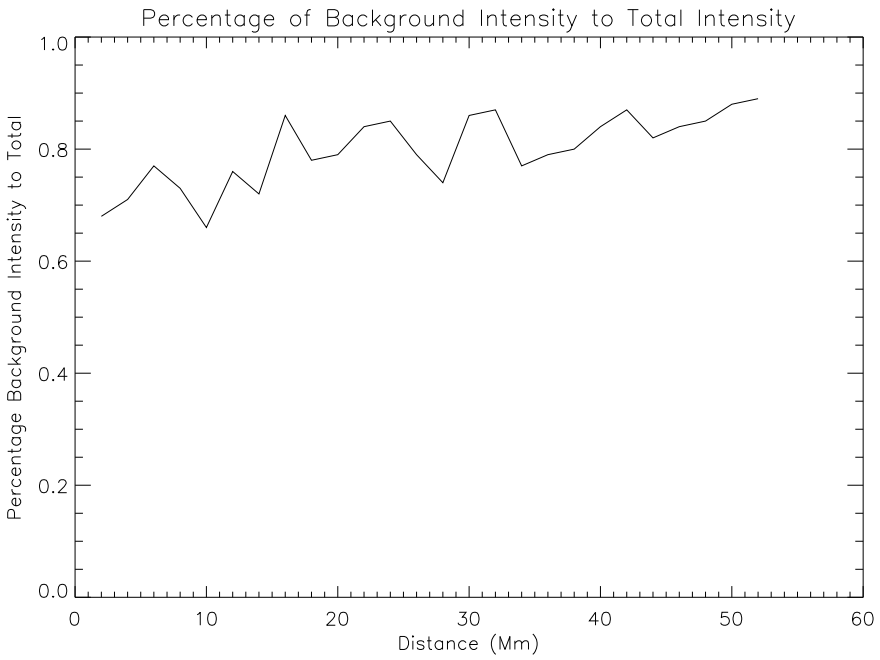

Figure 3.18: This plot shows the percentage of the unresolved emission to the total intensity measured for the entire AR. We have used intensity measurements along the radial line to determine the contribution of the structures intersected by the radial line and subtracted these intensities to form the unresolved intensity. The ratio of the unresolved background intensities to the total intensities for the radial line were used to calculate these percentages.

originating from the leading polarity sunspot were visible late in the day (UT) and by 20:00 UT on 14 June 2002, the entire region was visible on the disk. The majority of the emission was above the north-east limb during JOP 146 observations, and this permitted an investigation of the AR intensities as a function of altitude. We used the same techniques applied to AR 9628. The restricted FOV of the CDS rasters limits the number of pixels above the limb, however, enough data points along the radial line were available to determine a trend of intensity versus altitude.

Unlike AR 9628, this was a fairly quiescent AR. No flares were recorded by NOAA while AR 10001 was visible on the disk. The TRACE 173 Å images show a number of loops, but they show no discernible emission fluctuations during the CDS observations. An example of the TRACE 173 Å images is provided in Figure 3.19.

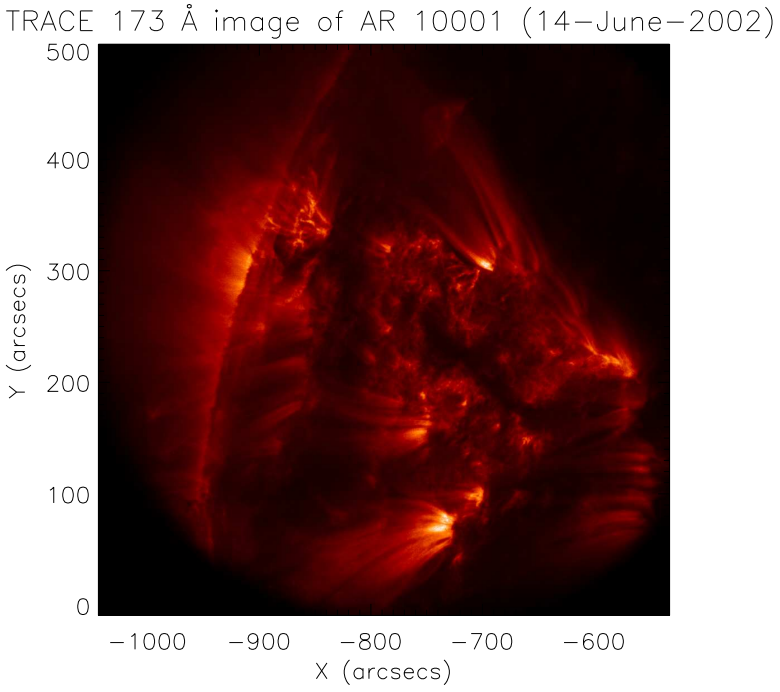

Figure 3.19: AR 10001 TRACE 173 Å image taken on 14 June 2002.

Additionally, the radial line selected for the study did not pass through any resolved loops, and this eliminated the need for the background subtraction process outlined for AR 9628. Furthermore, the measured intensities during several observations were nearly identical. A Si XII image of the AR is provided in Figure 3.20, and the radial line presented is included in this image.

Results

The emission lines used for study of this AR are listed in Table 3.1. Two data sets were analyzed, and the intensity verses altitude plots are presented in Figures 3.21 and 3.22. A table of the temperatures for the different ions and the associated χ_r^2 is given in Table 3.4.

Evident from Figures 3.21 and 3.22 and Table 3.4 is the conclusion that the

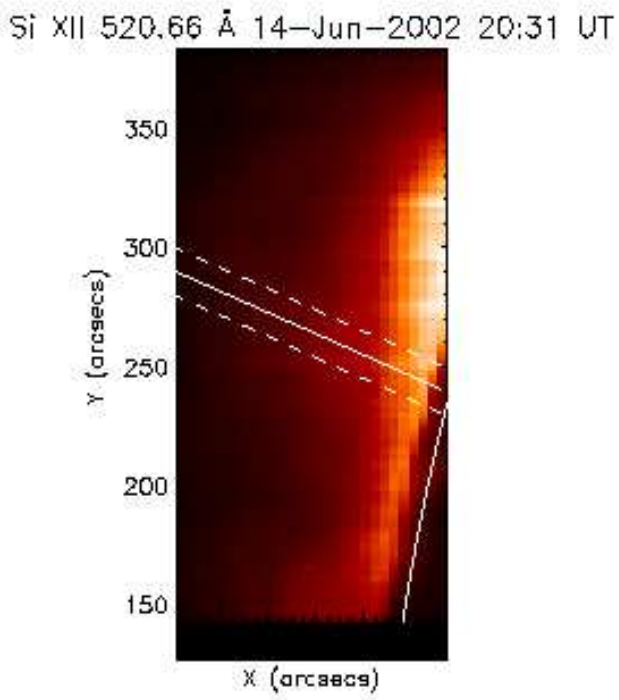

Figure 3.20: AR 10001 CDS Si XII 520.66 Å image taken on 14 June 2002. Shown on the plot are the selected radial line and the solar limb. The same radial line was used for all intensity verses altitude measurements. The two dashed lines are other radial lines used to measure the scale height temperature.

best fit scale height temperature for this AR is independent of the peak formation temperature of the ion because ions typically formed near 1 Mk are found to have scale height temperature near 1.7 MK and an ion with peak formation temperature near 2.7 MK (Fe XVI) is also found to have scale height temperatures near 1.7 MK. The quiescent AR unresolved corona is nearly isothermal, with a variance in the observed temperature of only 0.3 MK.

Discussion

The unresolved corona in this quiescent AR is nearly isothermal. It does not change in any consequential way over the course of a few hours. Unfortunately, there are no soft X-ray observations of this AR, and the EIT 284 Å images show no distinct

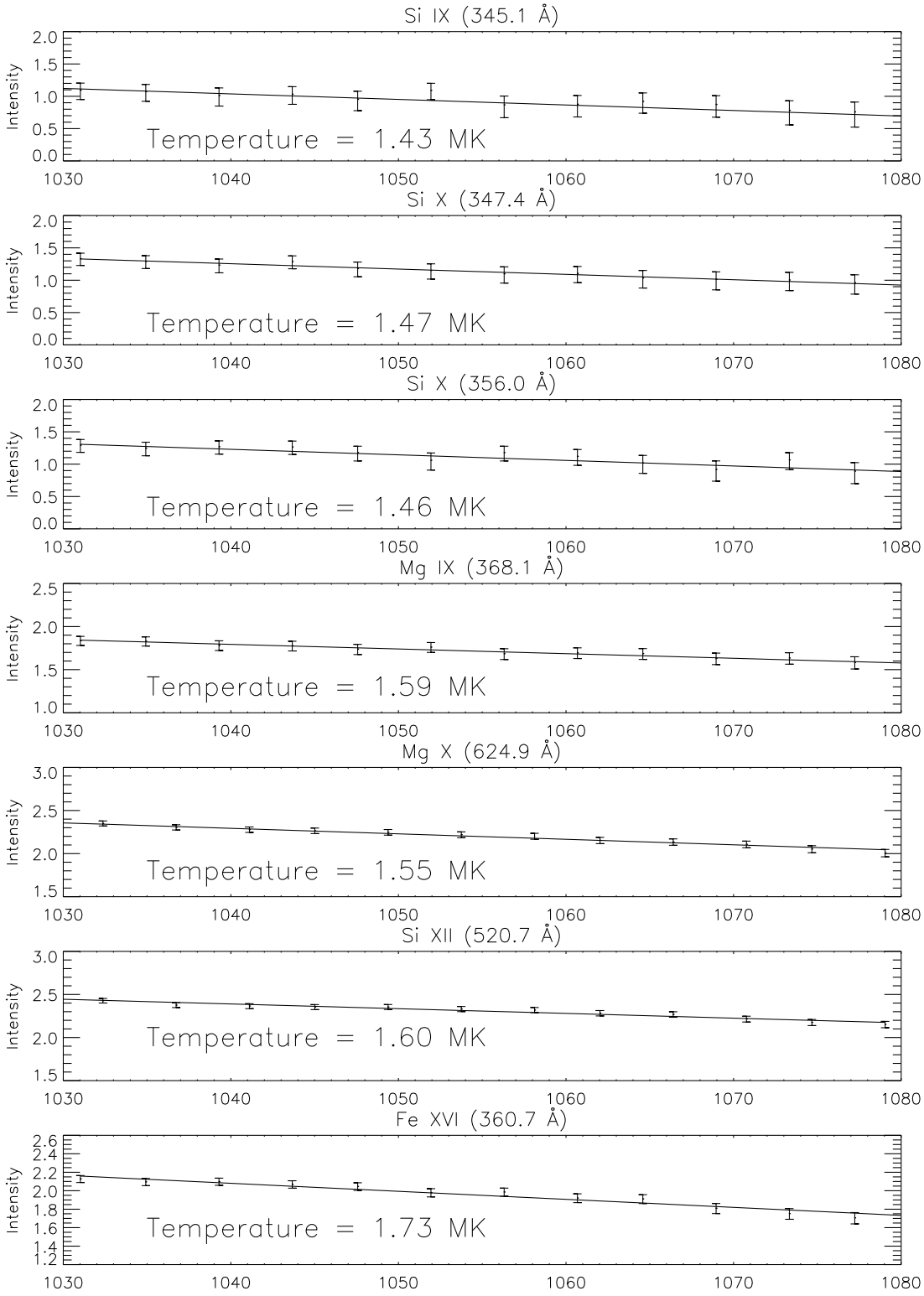

Figure 3.21: Intensity versus altitude for 14-June-2002. Raster began at 20:31 UT. Intensities are in units $\log_{10}$ ergs s^{-1} cm^{-2} and the distances (x axis) are given in arcseconds. One arcsecond is approximately 700 km on the Sun.

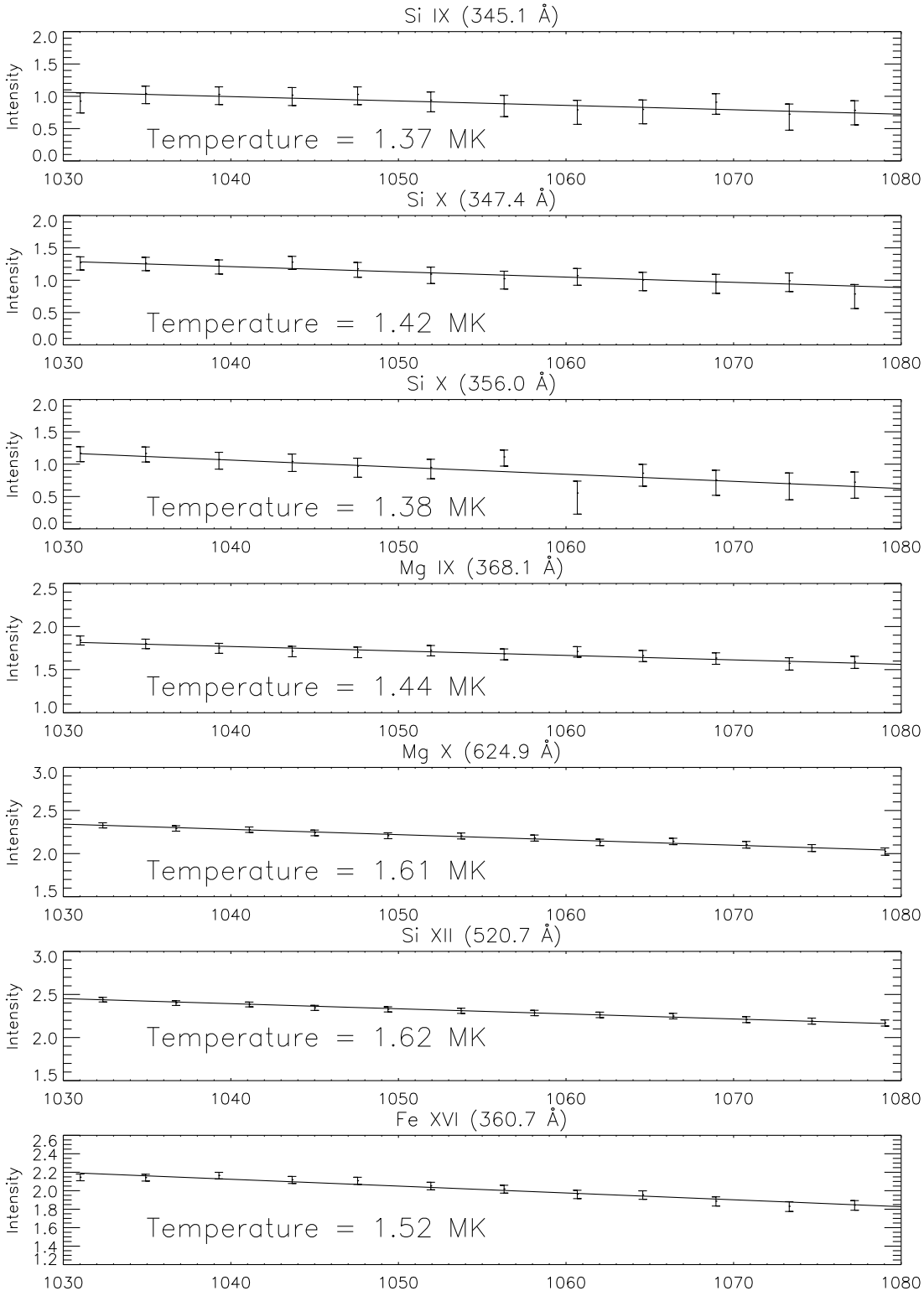

Figure 3.22: Intensity versus altitude for 14-June-2002. Raster began at 21:20 UT. Intensities are in units $\log_{10}$ ergs s^{-1} cm^{-2} and the distances (x axis) are given in arcseconds. One arcsecond is approximately 700 km on the Sun.

ION	T_{bf} (20:31)	χ^2_r	T_{bf} (16:47)	χ^2_r
Si IX	1.43 MK	1.31	1.37 MK	1.05
Si X	1.47 MK	1.25	1.42 MK	1.55
Si X	1.46 MK	1.47	1.38 MK	1.81
Mg IX	1.59 MK	1.15	1.44 MK	1.38
Mg X	1.55 MK	1.53	1.61 MK	1.11
Si XII	1.60 MK	1.56	1.62 MK	1.49
Fe XVI	1.73 MK	1.51	1.52 MK	1.59

Table 3.4: Best fit temperature for intensity along the radial segment for AR 10003.

features in the AR. Since the emission dominating the 284 Å passband is due to Fe XV (peak formation temperature of 2.5 MK), it is not surprising that no coronal loops are seen in the images; no structures are apparent in the Fe XVI, Si XII and Mg X rasters either and these ions exist over the range in temperatures as Fe XV. The TRACE 173 Å images do have a number of resolved loops, yet they are show no variation in brightness for several hours. Increases loop brightness in the corona is not observed, and the loops are visible, on average, for hours. It would seem that the dominant source of heating for this AR is a different heating mechanism than the one responsible for the observations of AR 9628. It is possible that AR 9628 would have reached this 'quiescent' background temperature if observations were available long enough after the flare event such that the energy input from the flare had dissipated via radiative and conductive processes.

Active Region 10249

On 15 January 2003, AR 10249 was near the southwest limb. It had been selected as the target for JOP 146 on the previous day, and it had produced a number of loops that were seen from the side, permitting investigation of the temperature and density along the loop length. It was decided to follow the AR over the limb, and

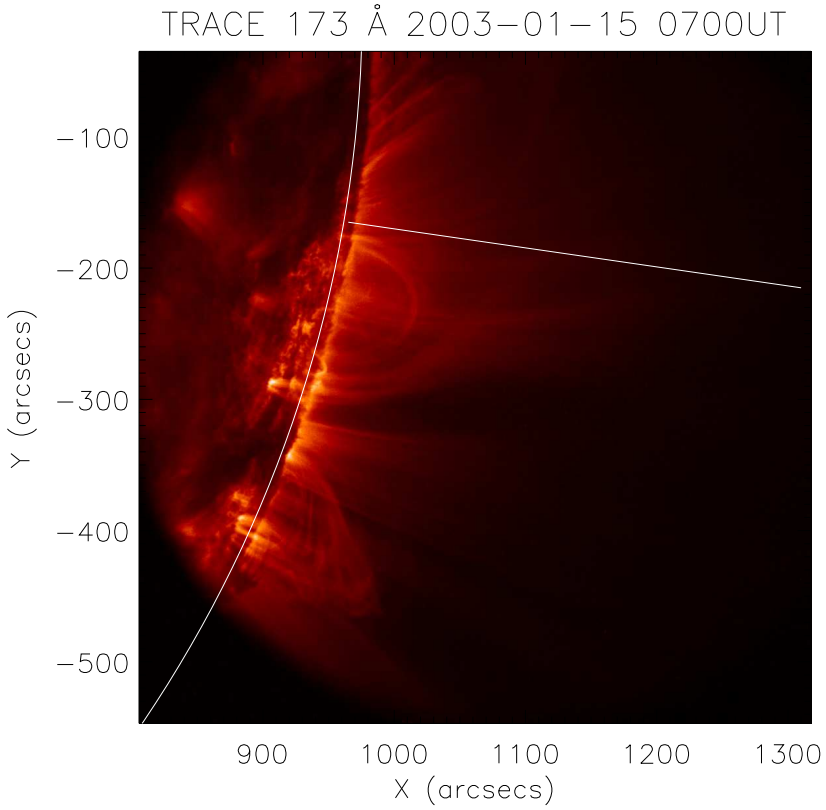

Figure 3.23: AR 10249 TRACE 173 Å image taken on 15 Jan 2003. Image includes the radial line selected for determination of the scale height temperature.

possibly image more such loops in the process. However, the activity of the region with respect to resolved loops decreased, and on 15 January few loops remained that had this same perspective. Since there were few loops contaminating the line-of-sight, these data presented a perfect opportunity to investigate the intensity as a function of altitude.

CDS observations of AR 10249 during SoHO campaign 6918 were much more complicated than performed previously. The details of the observations are presented in Chapter 2, but a brief description of the data used in this analysis is in order. CDS measured the intensity of emission in 20 different spectral bands. For each exposure

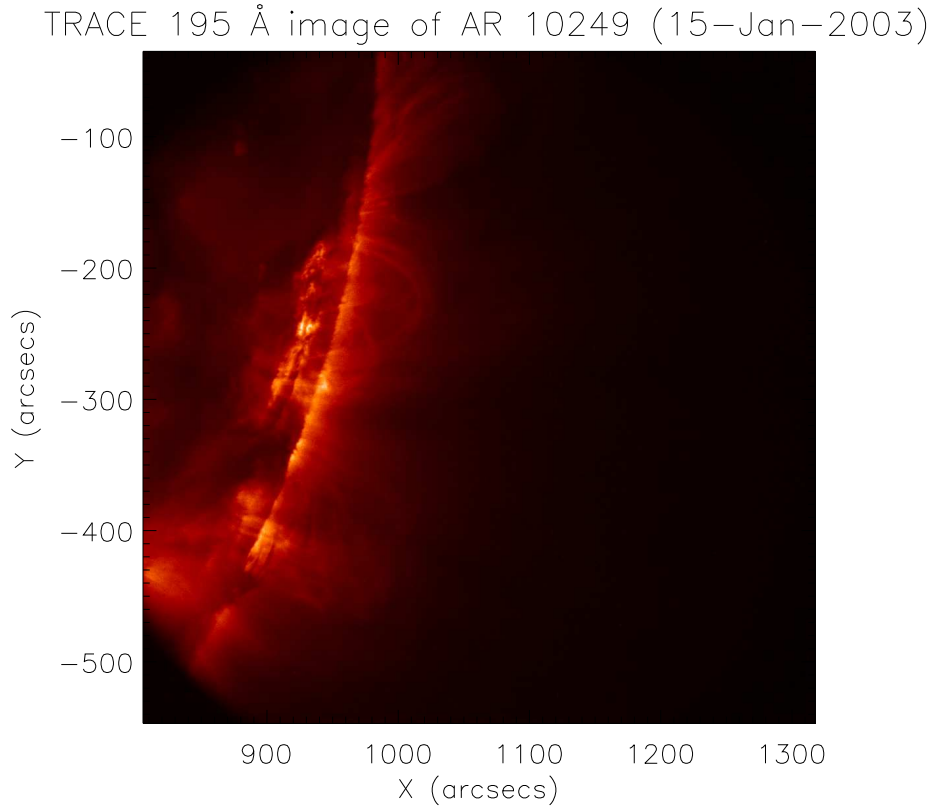

Figure 3.24: AR 10249 TRACE 195 Å image taken on 15 Jan 2003.

the $4 \times 240''$ slit was used, and 60 such exposures were made to form a raster covering $243 \times 240''$ FOV. Since there were few resolved loops in the AR, numerous radial lines could have been selected that would not require loop subtraction. An example of such a radial line is shown in the TRACE 173 Å image in Figure 3.23. These rasters took an hour to produce, and additional observations were made between these large FOV data sets. This fact limited the number of large FOV context images to only 2, but it was found that the data from these two rasters did not change in a significant way, so it is presumed that the AR was quiescent. No flares were recorded by the NOAA GOES instruments, so this appears reasonable.

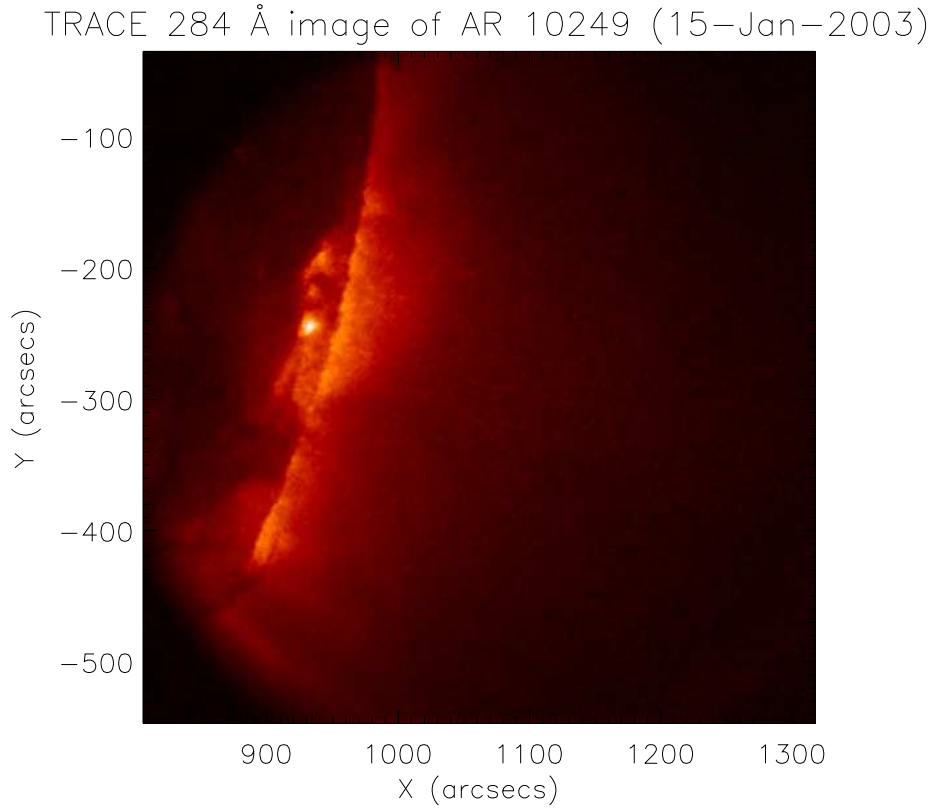

Figure 3.25: AR 10249 TRACE 284 Å image taken on 15 Jan 2003.

Data Analysis

The analysis technique for this CDS data was outlined for AR 9628. For each spectral passband the spectra at every pixel was fitted with a broadened Gaussian curve, and the intensity was output into an array. This formed an intensity image of the AR for each spectral line. A subset of these intensity images is shown in Figures 3.26 - 3.27. The images are presented in order of the peak formation temperature of the ion, starting in the upper left (coolest) and continuing to the lower right (hottest). It should be noted that the low temperature emission lines show no emission above the limb at any substantial altitude. This is in contrast with the observations of AR

9628, which had pronounced emission from these spectral lines. Figures 3.28 and 3.29 demonstrate the intensity decrease with altitude for a representative set of the available data. Other emission lines were observed, and the results of the curve fits determining the scale height for these ions are listed in table Table 3.5.

Results

The lack of data for the ions formed below 0.5 MK indicates a lack of episodic heating; if there were any intermittent deposition of energy into the loops of this AR, cooling processes would dissipate this energy via radiation in these emission lines. However, it is observed that the emission from ions formed at higher temperatures, say $T > 10^{5.9}$ K, is basically constant for nearly four hours during the observations. It would seem, based on these observations and the results of the scale height determination, that the unresolved corona of this AR is held at a fairly high temperature; the details of this heating mechanism being beyond the scope of this thesis. Furthermore, the temperature characterizing the unresolved component of the emission is the same for each of the ions observed with a formation temperature greater than the threshold temperature of 1 million Kelvin.

A noticeable departure from the isothermal background temperature determinations determined from most of the emission lines is evident in the scale height temperatures calculated for the three lines Si X (347.403 Å), Si X (356.03 Å), and Mg IX (368.07 Å). These scale height temperatures are a factor of two larger than their peak formation temperatures, and 1.5 times larger than the other ions in the data set. This is most likely due to the method employed to fit the curves. The model for the emission measure was based on a planar geometry atmosphere. However, at large enough altitude the true geometry of the atmosphere must be taken into account. In

ION	T_{bf} (06:52 UT)	χ^2_r	T_{bf} (09:19 UT)	χ^2_r	T_{ave}	χ^2_r
Si X (347.4 Å)	1.72 MK	1.38	2.27 MK	2.31	1.70 MK	4.78
Si X (356.0 Å)	1.78 MK	1.26	2.18 MK	2.89	1.70 MK	3.95
Mg IX	1.84 MK	1.24	2.09 MK	2.77	1.70 MK	3.34
Mg X	1.72 MK	1.36	1.92 MK	2.24		
Al XI	1.67 MK	1.74	1.61 MK	2.61		
Si XII	1.69 MK	1.86	1.72 MK	2.27		
Fe XVI	1.69 MK	1.68	1.73 MK	1.99		
Fe XVII	4.01 MK	1.45	3.18 MK	1.82		

Table 3.5: Best fit temperature for intensity along the radial segment for AR 10249. The final two columns are included to show that it is possible that the true scale height temperature for these three ions is probably not the best fit value. The anomalous result is most likely due to inaccurate approximation of the geometry of the atmosphere. A correction to a spherical geometry is attempted subsequently.

a spherical geometry atmosphere, the emission measure scale height is written

$$\mathrm{Em(h)} = \mathrm{Em(0)}\exp(-\frac{\mathrm{h}}{\lambda_{\mathrm{Em}}(\mathrm{T_e})(1+\frac{\mathrm{h}}{\mathrm{R_{sun}}})}) \quad . \tag{3.6}$$

Here h is the altitude above the solar surface. We have fit this function to the intensities along the radial line and present the results in Figures 3.30 and Table 3.6. For ions formed near 1 MK the inclusion of the constant in the exponent has an appreciable effect on the quality of the curve fits. This is obvious in Table 3.6, and the reduced chi-square for all of the ions in the data are improve using the hydrostatic scale height for a spherical geometry atmosphere.

Discussion

AR 10249 is very similar to AR 10001. The magnitude of the intensity does not change appreciably in time, and the scale height temperatures measured from the observations are approximately constant in time. These observed scale height temperatures are apparently independent of the peak formation temperature of the ion.

ION	T_{bf} (06:52 UT)	χ^2_r	T_{bf} (09:19 UT)	χ^2_r
Si X (347.4 Å)	1.55 MK	1.14	1.60 MK	1.51
Si X (356.0 Å)	1.53 MK	1.05	1.63 MK	1.62
Mg IX	1.49 MK	1.02	1.61 MK	1.49
Mg X	1.57 MK	1.19	1.62 MK	1.74
Al XI	1.61 MK	1.31	1.63 MK	1.60
Si XII	1.62 MK	1.45	1.80 MK	1.39
Fe XVI	1.69 MK	1.24	1.86 MK	1.57
Fe XVII	4.01 MK	1.31	3.01 MK	1.67

Table 3.6: Best fit temperature for intensity along the radial segment for AR 10249 using a spherical model for the geometry of the atmosphere.

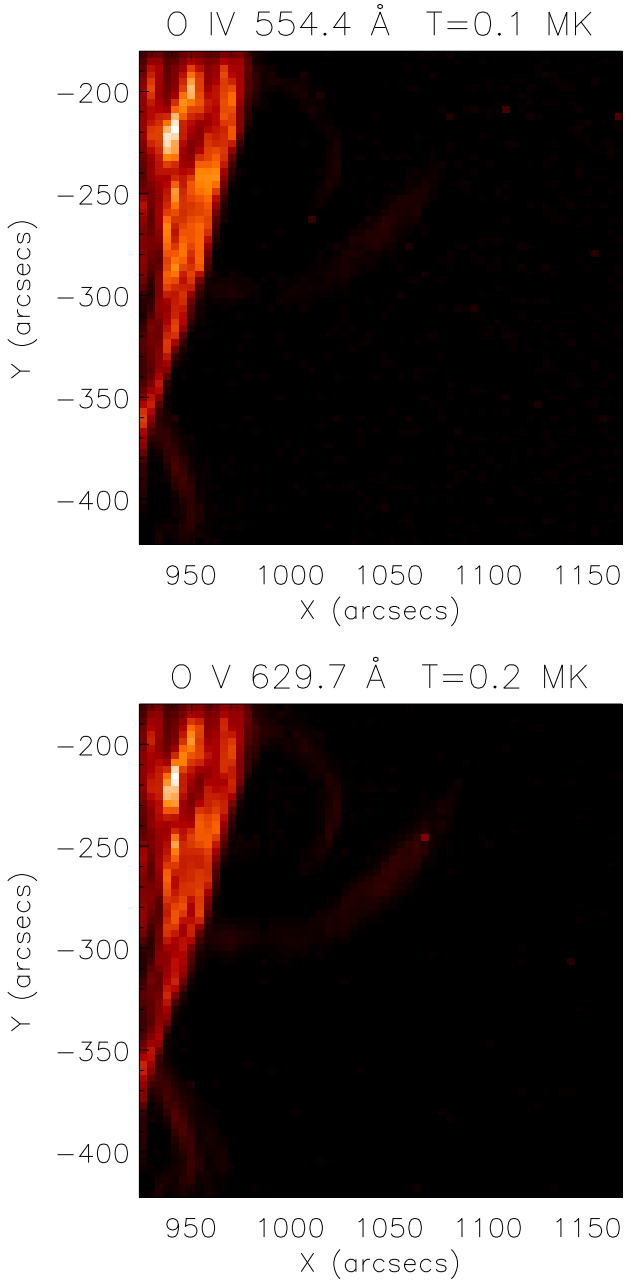

Figure 3.26: AR 10249 O IV (554.4 Å) and O V (629.7 Å) intensity images, with units ($ergs\ s^{-1}\ cm^{-2} pix^{-1}$). Raster began 15-Jan-2003 06:52:26.114 UT and covered 244″ .

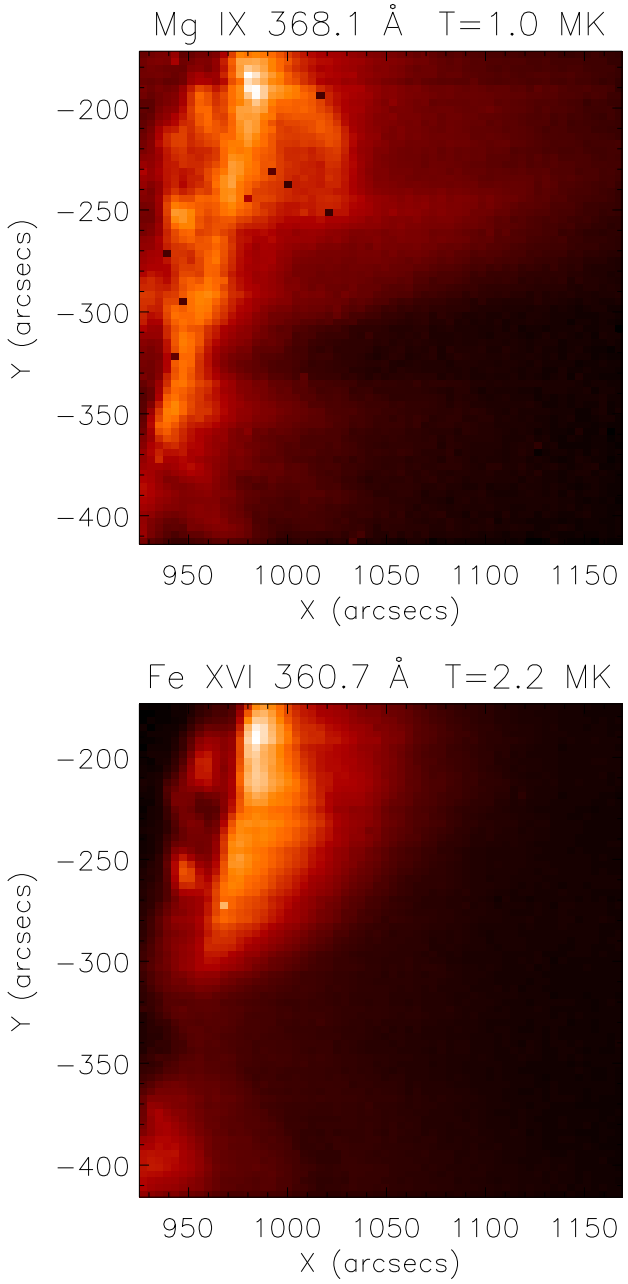

Figure 3.27: AR 10249 Mg IX (368.1 Å) and Fe XVI (360.7 Å) intensity images, with units ($ergs\ s^{-1}\ cm^{-2} pix^{-1}$). Raster began 15-Jan-2003 06:52:26.114 UT and covered 244″ .

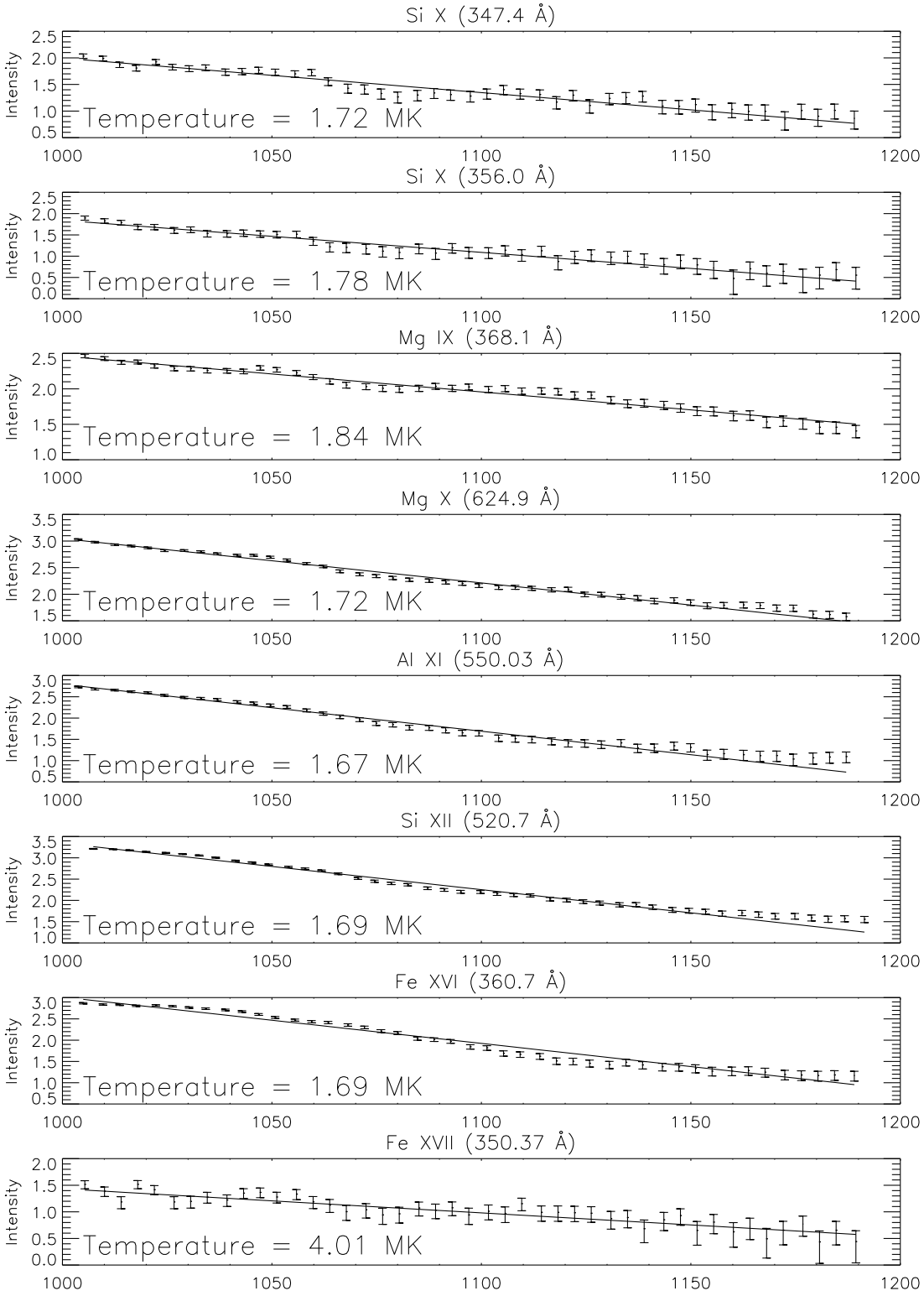

Figure 3.28: AR 10249 scale height best fit temperature plots. Raster began 15-Jan-2003 06:52:26.114 UT. Intensities are in units $\log_{10}$ ergs s^{-1} cm^{-2} and the distances (x axis) are given in arcseconds. One arcsecond is approximately 700 km on the Sun. Results are for plane geometry atmosphere.

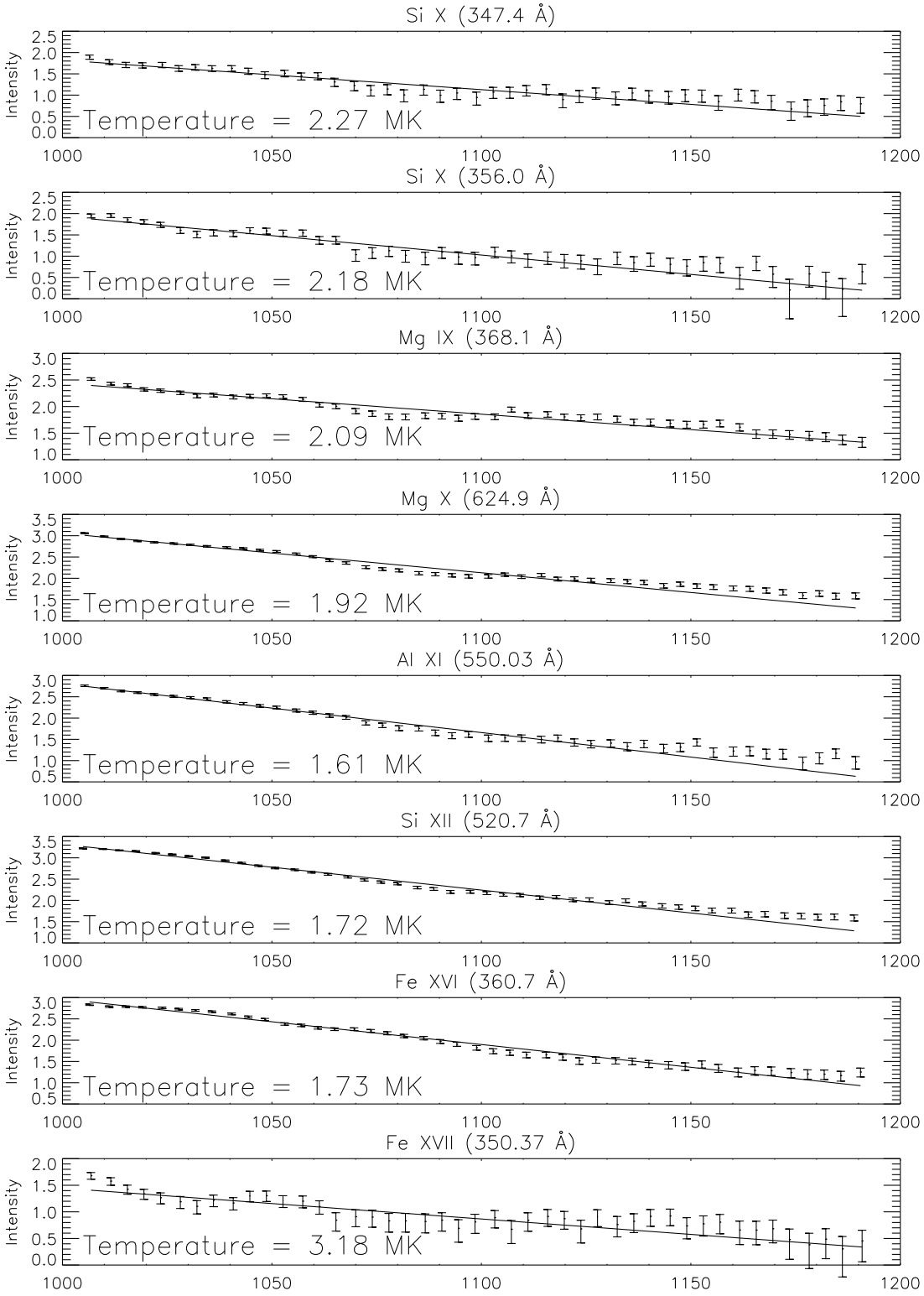

Figure 3.29: AR 10249 scale height best fit temperature plots. Raster began 15-Jan-2003 09:19:45.610 UT. Intensities are in units $\log_{10}$ ergs s^{-1} cm^{-2} and the distances (x axis) are given in arcseconds. One arcsecond is approximately 700 km on the Sun. Results are for plane geometry atmosphere.

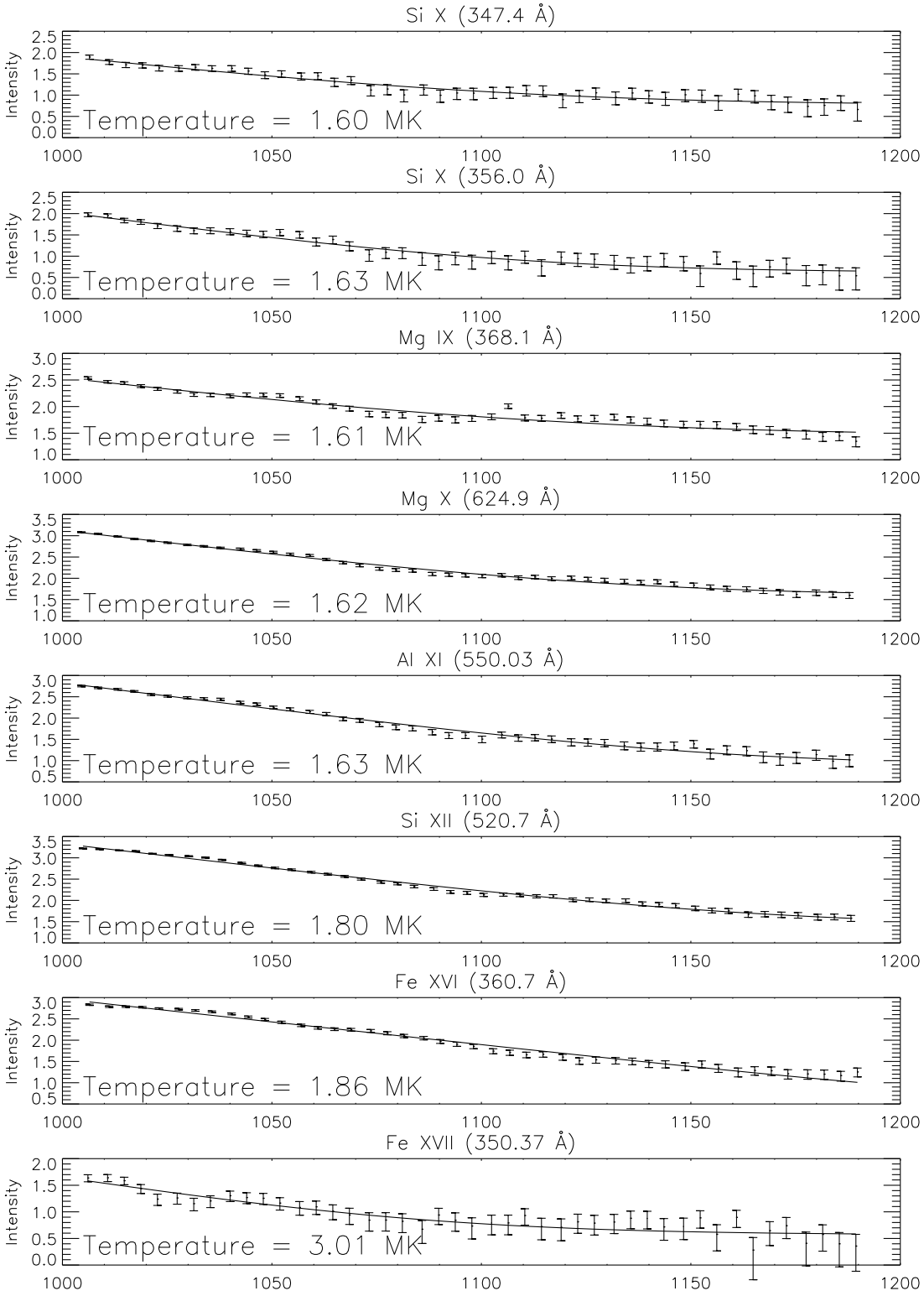

Figure 3.30: AR 10249 scale height best fit temperature plots. Raster began 15-Jan-2003 09:19:45.610 UT. Intensities are in units $\log_{10}$ ergs s^{-1} cm^{-2} and the distances (x axis) are given in arcseconds. One arcsecond is approximately 700 km on the Sun. This result employs a spherical geometry model of the atmosphere. The numerical results are presented in Table 3.6.

Chapter Summary

Aschwanden (2000) [39] presents the so-called hydrostatic weighting bias for the coronal atmosphere. This bias is meant to explain the observed breadth in DEM curves for coronal plasmas. It is most simply explained as the line-of-sight contribution to temperature as a function of altitude. For a hydrostatic atmosphere, the contributions to temperature from the plasma will decrease as a function of altitude because only the highest temperature plasmas will exist at the largest altitudes. Near the transition region there are many loops of varying length, and many temperatures are available to be sampled. At high altitude there will be a smaller range in temperatures sampled, and these will be preferentially shifted toward increasing temperature. In his book, Aschwanden [40] details the multi-hydrostatic corona (see §3.3 of that text). He points out that the K and F corona are, in general, in hydrostatic equilibrium. Furthermore, he indicates that the only deviations from this equilibrium configuration are when "inhomogeneities in the form of brighter loops or active regions occur" (p. 80 [40]). We have observed three ARs and found that there is indeed a component of the total line-of-sight emission due to a hydrostatic corona. This appears to be valid for both flaring ARs and non-flaring ARs, where the only difference between the flaring and non-flaring cases is the range in temperatures found for the emission measure scale height parameter λ.

From the results in this chapter it is highly likely that the unresolved atmosphere in ARs is near hydrostatic equilibrium unless perturbed by an event such as a flare. Even in the case of a flare the corona maintains equilibrium, yet it does so for many different loop lengths. Consequently, the observations show a multi-thermal corona in hydrostatic equilibrium after a flare in which the distributions in temperature decrease with time after the event. Quiescent ARs are also near equilibrium, and the measured scale heights are consistent with an isothermal unresolved corona. These quiescent

ARs appear to have a constant source of heating since the scale height temperature does not appear to change over the course of multiple observations spanning several hours.

The finding that the AR unresolved atmosphere is near hydrostatic equilibrium has a number of interesting applications. Studies of resolved coronal loops are greatly enhanced when the contaminating emission from the line-of-sight background is removed. This "cleaned" data can be used to accurately measure the cross-sections of loops, the temperature and density along the loops and promises to allow study of the evolution in these quantities as a function of time. A preliminary application of a background subtraction method for TRACE data is introduced in the following chapter, and results for several loops are also presented.

CHAPTER 4

AN ANALYSIS OF THREE CORONAL LOOPS

Introduction

With the deployment CDS in 1996 and launch of TRACE in April 1998, a new observing opportunity was possible. The high spatial and temporal resolution of TRACE and the temperature diagnostic capabilities of CDS permit characterization of coronal plasma properties to an extraordinary degree of detail. The first in-depth study of this type was carried out by Del Zanna and Mason (2003a) [32] with remarkable results. Del Zanna and Mason (2003a) [32] were able to measure the temperature, density and pressure for multiple positions along coronal loops using spectroscopy and the EM loci technique. These authors were also the first to report the observation that coronal radiation above 1.5 MK was not from well resolved coronal structures, but instead was from the unresolved background (called diffuse background in their paper).

Using the same methodology presented in Del Zanna and Mason (2003a) [32], we present the results for three coronal loops observed during a campaign written specifically for the joint observation of coronal loops with TRACE and CDS. Unlike Del Zanna and Mason (2003a) [32], the subsequent analysis employs a background subtraction method based on the results of Chapter 3, an innovation.

Instrumentation and Observations

First introduced in Chapter 2, JOP 146 was designed with the intention of combining the spatial and temporal resolution capabilities of the TRACE with the spectral resolution of CDS. On September 18, 2001, AR 9628 was the target for Campaign 6805.

CDS performed the scientific program OLOOP2. It is composed of 13 spectral passbands collected with the 4″ slit during 60 s exposures. There are 40 such exposures defining a total field of view equal to 162×240″. The routine began at 17:56:34 UT and ended approximately 47 minutes later. In addition to the CDS observations, TRACE 173 Å images were taken at a cadence of 35 seconds, with 19.48 s exposures. These images used the full CCD detector, subtending a 512×512″ area of the solar corona. During the time required to complete the CDS raster, 42 TRACE images were taken, with one TRACE image beginning during each of the CDS exposures.

Active Region 9628

Both the TRACE and CDS fields-of-view contained AR 9628. This region appeared behind the southeast limb on 17 September 2001, and the entire region was visible on the solar disk by 03:00 UT 19 September 2001. The active region subtended nearly 3′ in latitude (126,000 km).

The AR produced an M 1.4 flare, as recorded by the GOES satellite, at 17:06 UT 18 September 2001. The flare was visible in the TRACE images by 17:03:51 UT and it launched material into the atmosphere that fell back to the photosphere by 17:38:11 UT. Numerous post-flare loops became apparent in the subsequent minutes. In addition to the observed post-flare loops, there were many loops associated with this AR long before the flare. Using both difference imaging techniques and loop position versus time measurements, no conclusive evidence of loop oscillations could

be found for loops after the flare. Furthermore, no prominence was observed nor did a filament exist during the entire period the AR was visible on the solar disk. Using the Large Angle and Spectrometric Coronagraph (LASCO) on SoHO, there was no observable CME, although an increase in coronal outflow is apparent using the C2 coronograph at 21:30 UT.

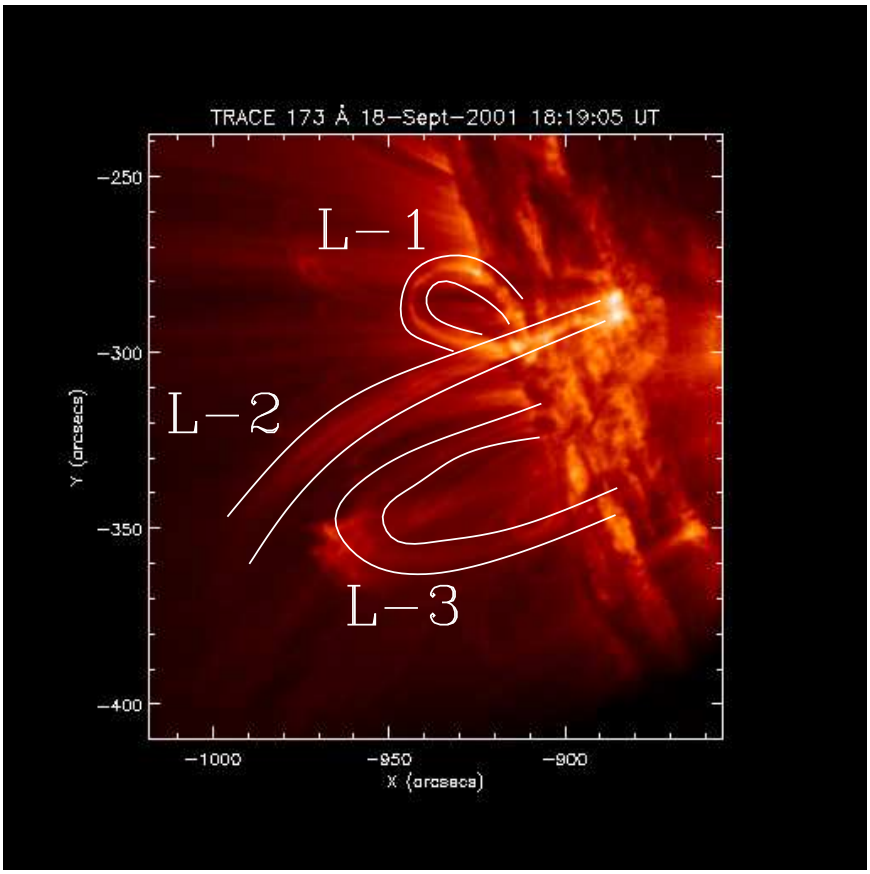

Figure 4.1: TRACE 173 Å image of Active Region 9628 at the start of CDS observations. Three loops (L-1, L-2, L-3) are outlined in the image.

Data Reduction and Analysis

Three loops of interest were chosen, henceforth referenced as L-1, L-2 and L-3. These three loops are shown in Figure 4.1, and the positions selected for measurement of temperature and density are shown in Figure 4.2 for L-1, Figure 4.3 for L-2, and Figure 4.4 for L-3. The TRACE and CDS data have been accurately co-aligned by

changing the TRACE apparent viewpoint to the first Lagrange Point (L1) where CDS is located. It was also necessary to correct the TRACE pointing by $2''$ in the negative $\hat{x}$ direction and $9''$ in the positive $\hat{y}$. These corrections were calculated by cross-correlation using the CDS Mg IX image and a composite TRACE image. A limb fitting routine was also used to match the limb as seen in both of these images.

The TRACE images that were taken during the time required for CDS to complete the rastering across the field-of-view were used to create the TRACE composite image. The start time for each of the CDS exposures is known and this was used to selected the TRACE image(s) taken during each of the 40 CDS exposures. For each of the co-aligned TRACE images, the portion of the TRACE image corresponding to the $4.02''$ slit position were removed from the image and used to form a composite. This was done by reconstructing all of the TRACE "slit" images into a single CDS field-of-view image.

The TRACE composite image was degraded to match the CDS resolution. Pixel positions were then selected along the loops from this TRACE image. This was done to make certain the pixels selected for CDS data analysis were not partially covering a TRACE loop. This would result in an estimate of intensity that was too low for the loop, and density and temperature measurements would have been negatively impacted. Eight pixel positions was found to be the maximum number of pixels possible for loops L-2 and L-3 because the remaining pixels were not completely within the loop. L-1 was restricted to 6 pixel positions using the same reasoning.

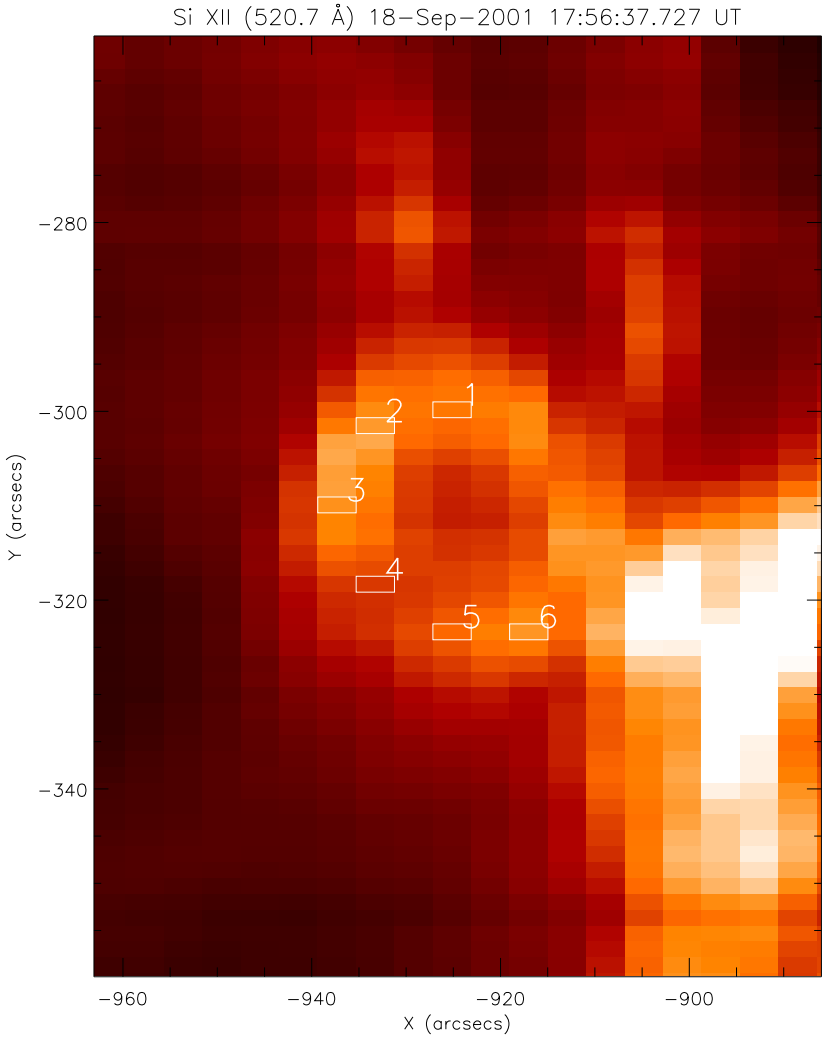

Figure 4.2: CDS Si XII (520.7 Å) intensity image of L-1. The pixels selected for measurement of temperature and density are shown on the image.

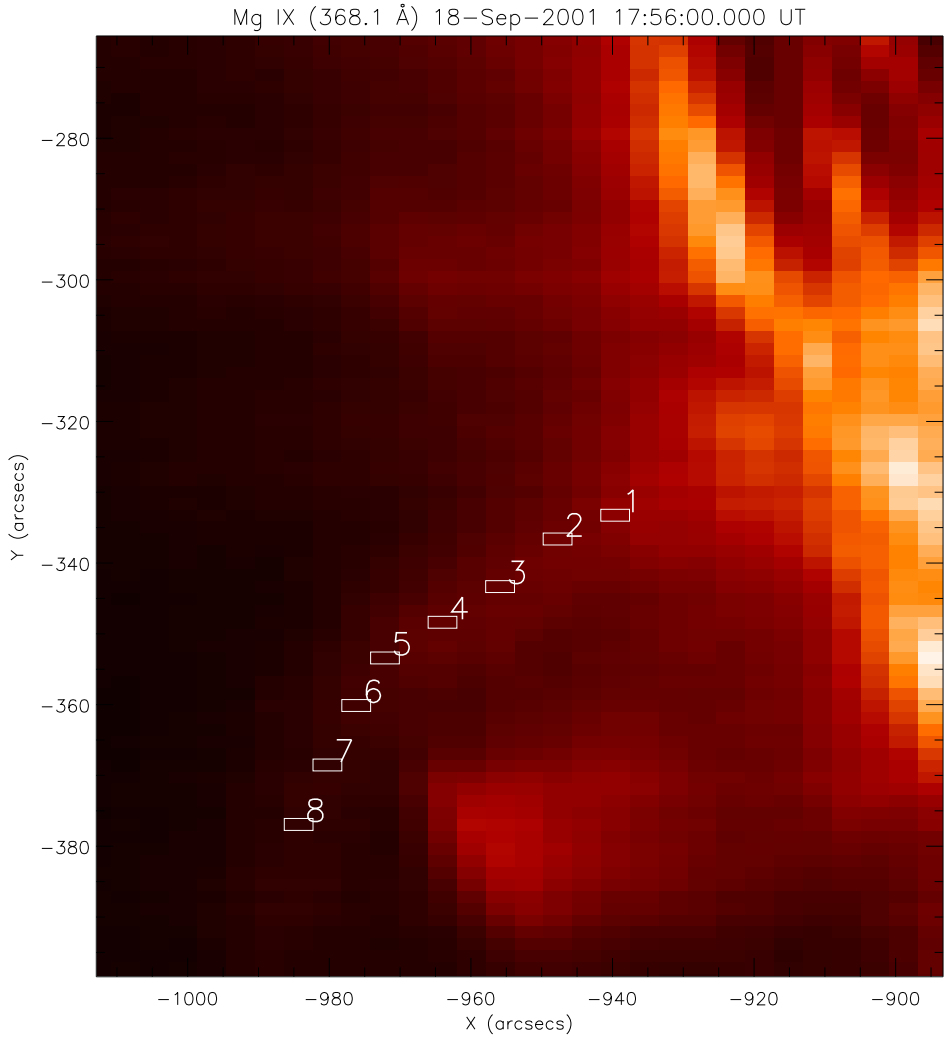

Figure 4.3: CDS Mg IX (368.1 Å) intensity image of L-2. The pixels selected for measurement of temperature and density are shown on the image.

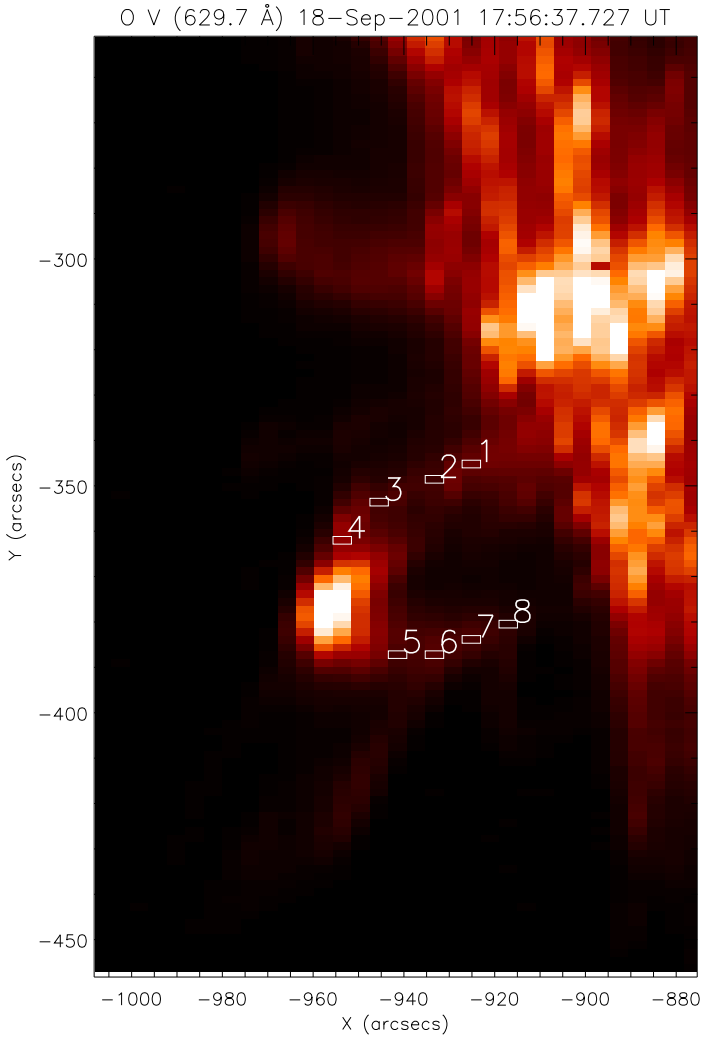

Figure 4.4: CDS O V (629.7 Å) intensity image of L-3. The pixels selected for measurement of temperature and density are shown on the image. The large enhancement at the 'top' of this loop is actually the location of several loops intersecting along the line-of-sight. No pixels were selected at this location as a result.

Data Analysis

TRACE background subtraction:

Before recording measured values for the TRACE flux pix^{-1}, application of the standard Solarsoft data preparation procedures and a background subtraction routine were performed. The TRACE images have a nearly uniform background emission for the low corona, which is found to be smaller in total counts per pixel when compared to bright features in the images such as coronal loops. This background emission decreases exponentially as a function of distance above the solar disk. The value for the background emission is determined in two different ways.

1. Fit an exponential surface to the background emission. The initial value for the surface was taken to be the average value of the flux measured one pixel above the limb. Every pixel along the limb was used to determine a radial line, and an exponential was fit to the flux along each of these radial lines. All of these exponential fits were juxtaposed to form a background "image", and we subtracted this background "image" from the original image.

2. Determine the average count rate at the limb and then use the relation

$$I = I_{ave} e^{-\frac{alt}{s}} \tag{4.1}$$

to determine the count rates for all points above the limb. Here I is the "corrected" value and I_{ave} is the average value for count rate at the limb, *alt* is the distance above the limb, and s is the emission measure scale height for Fe IX. The two different derivations of a background image from procedure 1 and 2 differ by less than 9%.

A model of the EUV background for Fe IX was used to generate the image given in

Figure 4.5, and the background subtracted image is shown in Figure 4.6. The peak formation temperature for Fe IX was selected as the best temperature to approximate the background for the TRACE 173 Å since the Fe IX line is predicted by the spectral package CHIANTI to be the dominant line in the TRACE 173 Å channel. Please refer to Chapter 2 for more details on this assumption. This may be the first procedure yet offered to subtract a model of the real coronal background.

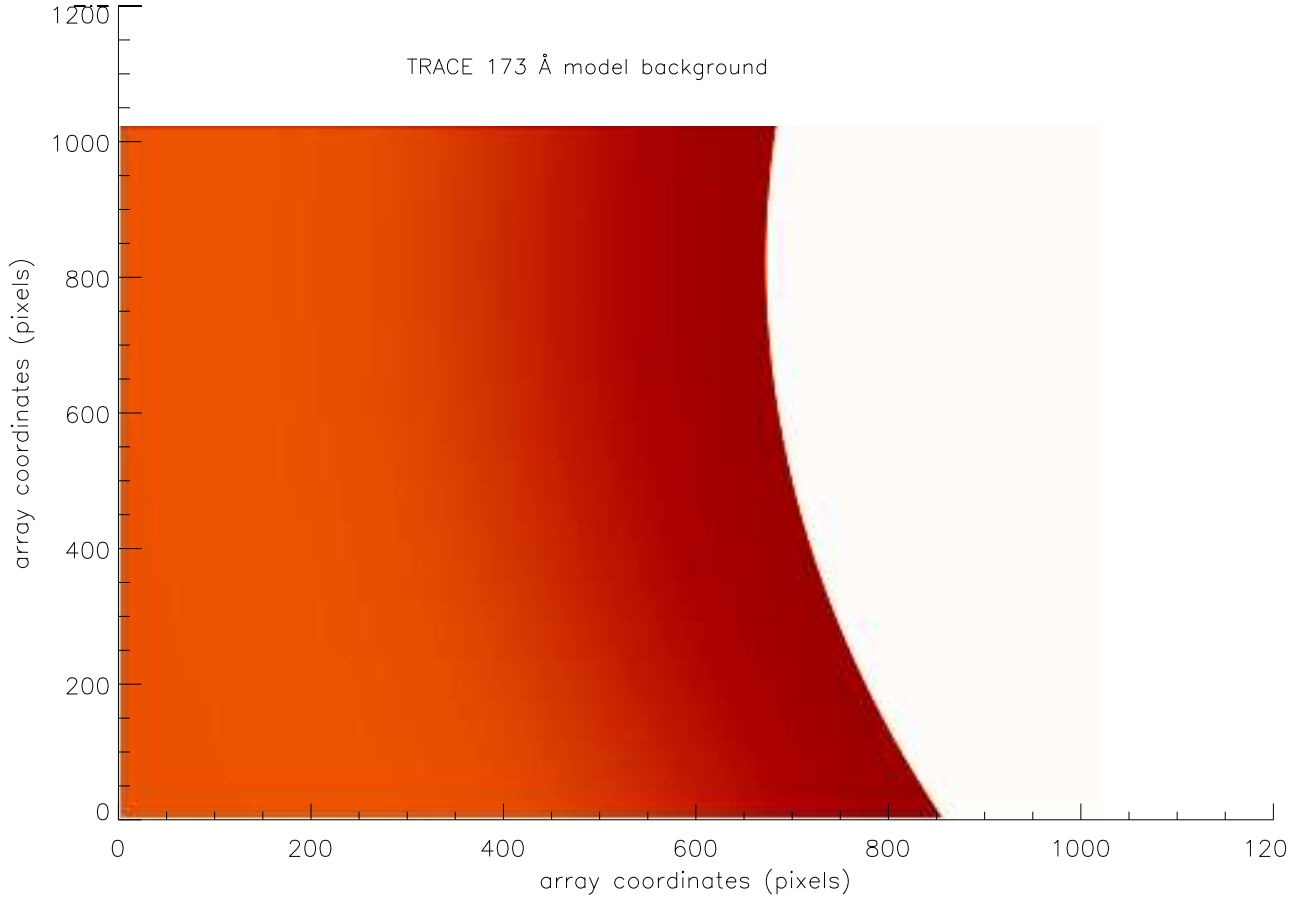

Figure 4.5: The background image subtracted from the TRACE image set. A model for the background was developed for Fe IX using the hydrostatic scale height assumptions of Chapter 3.

The background subtraction process outlined above reduces the background values for pixels below 34 Mm to 0.0 ± 0.67 counts. This process also increases the contrast

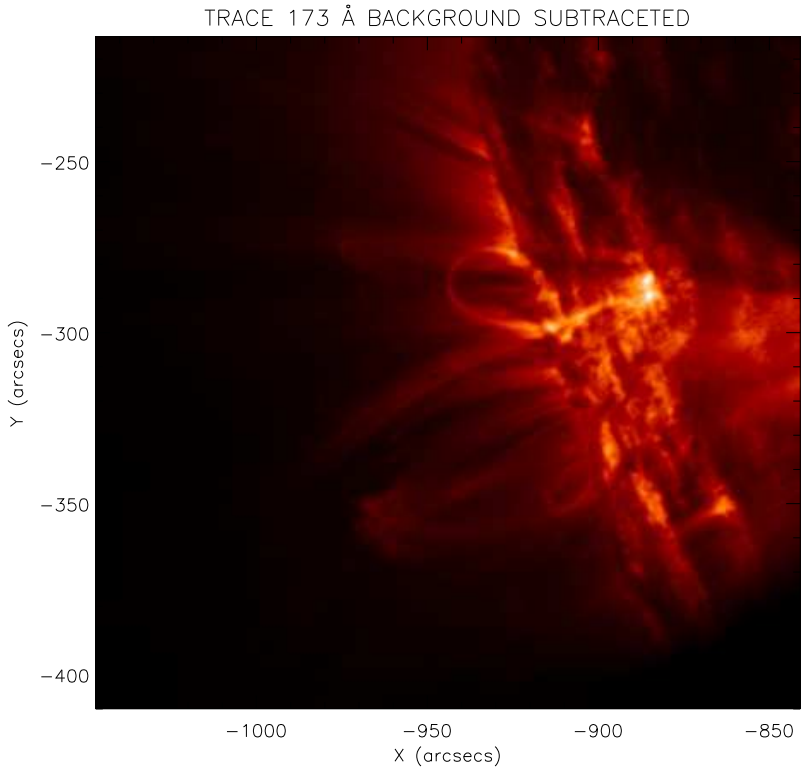

Figure 4.6: TRACE 173 Å image of Active Region 9628 at the start of CDS observations after background subtraction. This image is the same image as shown in Figure 4.1 prior to background subtraction.

for structures like coronal loops, as the underlying emission has been removed and the overlying structures are now an order of magnitude larger than the background (instead of the factor of two or three larger found prior to subtraction).

TRACE measurements for the Three Loops:

After the data were calibrated and the background subtracted, we found the values for flux at several points along each of the three loops. The locations of these positions are shown in Figures 4.2 - 4.4. Since selected positions below the limb did not include an estimate of the background, these positions were eliminated from the analysis. The

flux values measured for all three loops are given in Tables 4.1, 4.2, and 4.3. In these tables, I_{total} is the pre-background subtracted value of flux and I_{bg} is the flux for the resolved loop after background subtraction. The cross-sections of the loops have also been measured at the chosen pixel positions and recorded in the tables. The cross-section is herein defined to be the full width at half maximum of the profile in counts across a resolved loop. An example of one of these Gaussian fits and the derived width are shown in Figure 4.7. The distance along the loop half length, designated $S_{\frac{1}{2}}$, is measured by finding the length of a segment from each chosen position to the next chosen pixel. The distance for pixel 1 for each of the three loops was found by measuring the length of the segment from the loop footpoint to pixel 1. The center of the pixel was used as the endpoint for all of the segments.

Using 42 TRACE images and beginning with an 173 Å image taken at 17:53 UT, the values for the flux and cross-section are determined. The loops are not each visible for the entire period spanned by the 42 images, but all three do have at least 18 images available for these measurements.

CDS temperature and density derivations:

For each of the loops in Figure 4.1, CDS intensities calculated for all of the pixel positions indicated in Figure 4.2 - 4.4 were used to determine the temperature and density sensitive line ratios. The Fe XIII and Fe XVI, Si X and Si XII, Mg IX and Mg X, Si IX and Si X, and O IV and O V line pairs were used to determine the temperature of the plasma. Using the density sensitive line pair Si X (356.1 / 347.4 Å) the density is calculated at the different pixel positions. The density is calculated based upon the rel.ative intensity of the forbidden line (347.403 Å) to the allowed transition. This method is detailed in Chapter 2 (pg 24 ff.). Two different values for density are provided in the tables. N_e(BG) is the density proior to background subtraction and $N_e(-BG)$ is the density post-background subtraction. The results

of these measurements are shown in Tables 4.1 - 4.3. A review of these methods for CDS data is available from Mason et al. (1997) [41].

The measurement of temperature and density for these numerous pixel positions allows for a determination of the pressure along these loops. It is a straightforward calculation and as is evident from Table 4.1 - 4.3, a gradient in the pressure calculated from the observations is found for both L-1 and L-3. The results for L-2 are not consistent with a gradient in the pressure, yet it is not possible to conclude L-2 is in hydrostatic equilibrium as the emission and density do not decrease exponentially with altitude.

	$S_{\frac{1}{2}}$ (10^4 km)	N_e (BG) 10^8 cm^{-3}	N_e (-BG) 10^8 cm^{-3}	$\log_{10}$ T_e Si IX Si X (K)	$\log_{10}$ T_e Mg IX Mg X (K)	$\log_{10}$ T_e Si X Si XII (K)	$\log_{10}$ T_e Fe XIII Fe XVI (K)
1	1.4	62 ± 23	54 ± 34	6.3 ± 0.1	6.3 ± 0.2	6.3 ± 0.2	6.3 ± 0.1
2	1.96	68 ± 26	58 ± 36	6.3 ± 0.1	6.3 ± 0.1	6.3 ± 0.1	6.4 ± 0.1
3	2.52	64 ± 25	56 ± 35	6.3 ± 0.2	6.4 ± 0.2	6.4 ± 0.2	6.4 ± 0.2
4	1.96	54 ± 17	46 ± 28	6.2 ± 0.1	6.3 ± 0.1	6.3 ± 0.1	6.4 ± 0.2
5	1.4	67 ± 25	59 ± 38	6.3 ± 0.1	6.3 ± 0.1	6.3 ± 0.1	6.3 ± 0.1
6	0.84	58 ± 19	50 ± 28	6.2 ± 0.1	6.2 ± 0.1	6.2 ± 0.1	6.3 ± 0.2

	I_{total} counts/s	I_{bg} counts/s	W_{tot} (10^3 km) (10^3 km)	W_{bg} (10^3 km) (10^3 km)
1	4.4 ± 0.3	0.98 ± 0.6	3.37 ± 0.11	2.50 ± 0.04
2	4.0 ± 0.3	0.96 ± 0.6	3.01 ± 0.10	2.40 ± 0.04
3	3.9 ± 0.2	0.90 ± 0.6	2.98 ± 0.09	2.31 ± 0.03
4	3.8 ± 0.2	0.92 ± 0.6	3.15 ± 0.11	2.43 ± 0.05
5	4.2 ± 0.3	0.98 ± 0.6	3.35 ± 0.12	2.42 ± 0.05
6	4.9 ± 0.4	1.12 ± 0.7	3.64 ± 0.16	2.59 ± 0.10

Table 4.1: Physical Characteristics for Loop L-1. The electron densities are in units 10^8 cm^{-3}. Below the double horizontal line are the fluxes from the TRACE 173 Å data in flux pix^{-1} the width of the loop before (W_{tot}) and after (W_{bg}) background subtraction.

	$S_{\frac{1}{2}}$ (10^4 km)	N_e (BG) 10^8 cm^{-3}	N_e (-BG) 10^8 cm^{-3}	$\log_{10}$ T_e Si IX Si X (K)	$\log_{10}$ T_e Mg IX Mg X (K)	$\log_{10}$ T_e Si X Si XII (K)	$\log_{10}$ T_e Fe XIII Fe XVI (K)
1	1.96	23 ± 11	15 ± 10	6.1 ± 0.1	6.1 ± 0.2	6.2 ± 0.1	6.2 ± 0.1
2	2.52	19 ± 10	12 ± 9	6.1 ± 0.1	6.1 ± 0.1	6.1 ± 0.1	6.1 ± 0.1
3	3.00	19 ± 9	12 ± 7	6.1 ± 1.2	6.1 ± 0.1	6.1 ± 0.1	6.3 ± 0.2
4	3.36	17 ± 9	11 ± 7	6.2 ± 0.2	6.2 ± 0.1	6.3 ± 0.2	6.3 ± 0.2
5	3.64	14 ± 6	7 ± 5	6.1 ± 0.1	6.3 ± 0.2	6.3 ± 0.2	6.4 ± 0.2
6	4.20	13 ± 6	6 ± 3	6.2 ± 0.1	6.2 ± 0.2	6.3 ± 0.2	6.3 ± 0.2
7	4.48	10 ± 3	5 ± 3	6.2 ± 0.2	6.2 ± 0.2	6.2 ± 0.2	6.3 ± 0.2
8	5.42	8 ± 2	4 ± 2	6.3 ± 0.1	6.3 ± 0.1	6.3 ± 0.1	6.4 ± 0.2

	I_{total} counts/s	I_{bg} counts/s	W_{tot} (10^3 km) (10^3 km)	W_{bg} (10^3 km) (10^3 km)
1	10.2 ± 3.2	4.8 ± 2.8	3.85 ± 0.14	2.61 ± 0.06
2	10.6 ± 3.3	5.27 ± 2.9	3.71 ± 0.13	2.52 ± 0.05
3	11.4 ± 3.4	5.31 ± 2.9	3.76 ± 0.13	2.40 ± 0.05
4	10.4 ± 3.2	6.12 ± 3.1	3.80 ± 0.13	2.37 ± 0.05
5	10.1 ± 3.2	6.59 ± 3.2	3.83 ± 0.14	2.28 ± 0.04
6	9.4 ± 3.1	7.5 ± 3.3	3.61 ± 0.10	2.11 ± 0.04

Table 4.2: Physical Characteristics for L-2. The electron densities are in units 10^8 cm^{-3}. Below the double horizontal line are the fluxes from the TRACE 173 Å data in flux pix^{-1} the width of the loop before (W_{tot}) and after (W_{bg}) background subtraction. Only six pixel positions in the TRACE images were used due to lack of counts in pixel positions 7 and 8.

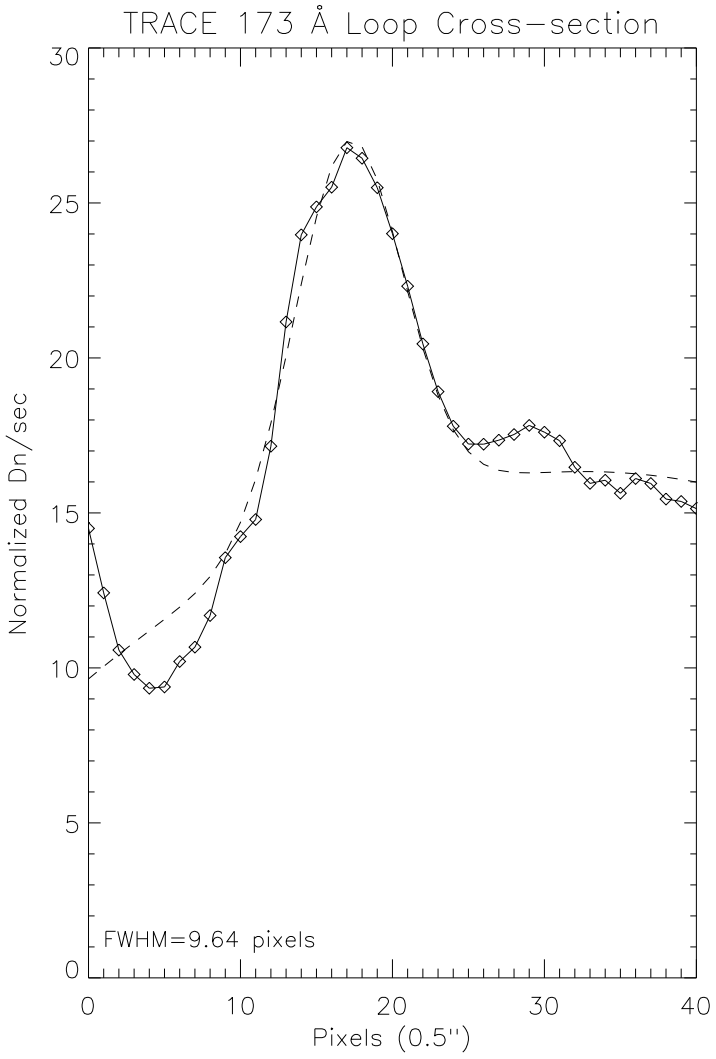

Figure 4.7: TRACE 173 Å loop cross-section. The full width at half maximum of the Gaussian curve fit to the data is defined to be the loop width. The background was fixed at 16 Dn/sec to match the value for flux due to a structure next to the loop cross-section shown above. The FWHM is then the width of the Gaussian at a point halfway between the arbitrary background and the peak of the curve.

	$S_{\frac{1}{2}}$ (10^4 km)	N_e (BG) 10^8 cm^{-3}	N_e (-BG) 10^8 cm^{-3}	$\log_{10}$ T_e O III O V (K)	$\log_{10}$ T_e Si IX Si X (K)	$\log_{10}$ T_e Mg IX Mg X (K)	$\log_{10}$ T_e Si X Si XII (K)
1	0.84	10 ± 5	8 ± 4	5.4 ± 0.1	6.0 ± 0.1	6.0 ± 0.1	0 ± 0
2	1.11	15 ± 7	12 ± 8	5.3 ± 0.1	5.7 ± 0.1	0 ± 0	0 ± 0
3	1.55	19 ± 7	16 ± 7	5.3 ± 0.1	5.8 ± 0.1	0 ± 0	0 ± 0
4	1.95	81 ± 42	56 ± 31	5.4 ± 0.1	6.0 ± 0.2	0 ± 0	0 ± 0
5	1.86	38 ± 22	28 ± 17	5.4 ± 0.1	5.7 ± 0.1	0 ± 0	0 ± 0
6	1.63	22 ± 11	16 ± 7	5.3 ± 0.1	5.7 ± 0.1	0 ± 0	0 ± 0
7	1.41	12 ± 5	9 ± 5	5.2 ± 0.1	5.7 ± 0.1	0 ± 0	0 ± 0
8	1.0	9 ± 3	5 ± 4	5.2 ± 0.1	5.7 ± 0.1	0 ± 0	0 ± 0

	I_{total} counts/s	I_{bg} counts/s	W_{tot} (10^3 km) (10^3 km)	W_{bg} (10^3 km) (10^3 km)
1	4.4 ± 0.3	0.98 ± 0.6	3.37 ± 0.11	2.50 ± 0.04
2	4.0 ± 0.3	0.96 ± 0.6	3.01 ± 0.10	2.40 ± 0.04
3	3.9 ± 0.2	0.90 ± 0.6	2.98 ± 0.09	2.31 ± 0.03
4	3.8 ± 0.2	0.92 ± 0.6	3.15 ± 0.11	2.43 ± 0.05
5	4.2 ± 0.3	0.98 ± 0.6	3.35 ± 0.12	2.42 ± 0.05
6	4.9 ± 0.4	1.12 ± 0.7	3.64 ± 0.16	2.59 ± 0.10

Table 4.3: Physical Characteristics for L-3. The electron densities are in units 10^8 cm^{-3}. Below the double horizontal line are the fluxes from the TRACE 173 Å data in flux pix^{-1} the width of the loop before (W_{tot}) and after (W_{bg}) background subtraction. Only six pixel positions in the TRACE images were used due to lack of counts in pixel positions 7 and 8.

Summary

The results presented in this chapter indicate that the temperatures and densities along resolved coronal loops differ substantially from the results of the unresolved AR corona. The density along these resolved loops is nearly constant with altitude - an indication that these structures are not in hydrostatic equilibrium. This is verified because the loops do not display the same exponential fall off in flux as a function of altitude as does the unresolved background. We have calculated the standard deviation in the mean density for all three loops. The mean density for L-1 was found to be $\bar{N_e} = 61 \times 10^8$ with a standard deviation $\delta N_e = 21 \times 10^8$. Additionally, the temperatures of the three loops analyzed are markedly different from one structure to the next and the results of the temperature ratio measurements are all nearly identical. The mean temperature for L-1 was found to be $\bar{T_e} = 6.31 log_{10}(\mathrm{K})$ for pixel 1 with a standard deviation of $\delta T_e = 0.11 log_{10}(\mathrm{K})$. The results indicated that the density and the temperature are constant along the loop and at a pixel, respectively. There is a temperature gradient along loops L-1 and L-2 however. The mean temperature for L-1 *along* the loop is $\bar{T_e} = 6.39 log_{10}(\mathrm{K})$ and the standard error in the mean is found to be $\delta T_e = 0.12 log_{10}(\mathrm{K})$. The mean temperature at pixel 6 for L-1 is found to be $\bar{T_e} = 6.23 log_{10}(\mathrm{K})$ which is greater than one standard deviation from the isothermal result. The results for L-1 and L-2 indicate each structure is isothermal at the pixel, although the measurements do show a slight increase in temperature as a function of loop half length. L-3 is distinct in that it is the only structure of the three to be multi-thermal at a pixel, and multi-thermal along the loop half length. If it had happened that the line ratios were all markedly different, this would have been consistent with a range in temperatures for the plasma at every pixel, but this was only observed for L-3.

L-1 is at a much higher temperature than the other two loops, and is not apparent

in the TRACE images until 14 minutes after the exposures in CDS were complete. This is clearly shown in Figure 4.8, where the intensity at pixel 3 is shown as a function of time and the time of the CDS exposures are shown on the figure. This provides evidence of the cooling time for these loops, defined to be

$$\tau_{cooling} = \frac{3 n_e k_B T_e}{n_e n_H \Lambda_R} \quad , \tag{4.2}$$

and it is observed to be a factor of three longer than the expected radiative cooling time for two million K plasma, where Λ_R is the radiative loss function. We have used the radiative loss function presented by Martens, Kankelborg and Berger (2000) [42] and the Meyer abundances [1]. Using the mean temperature derived for L-1 at pixel position 3, a cooling time of approximately 430 seconds is found. However the observed delay is 870 seconds. This requires sustained heating of the plasma that decays with time. We plan to investigate the functional form for this heating mechanism in the future.

The cool loop, L-3, also has a nearly constant density as a function of loop half-length. It is observed to decay away and is no longer distinguishable in the TRACE images after only 13 minutes. This too is longer than the radiative cooling time for 500,000 K plasma, but this theoretical cooling time is about 8 minutes and is not inconsistent with what is observed. It is likely that this loop was heated by the flare to some higher temperature and is captured by CDS and TRACE during a stage where no additional heat is provided to the loop, in which case it is radiatively and conductively dissipating this energy. This transient loop also shows clear evidence of multi-thermal plasma at several positions along the loop half length.

Finally, L-2 has a temperature between those measured for the other loops and is quasi-static during the 42 TRACE images. This loop has a density decrease and a marginal temperature increase along the loop half length. It is apparent from the

TRACE images that this is actually a group of loops, probably three, that are in close proximity to each other. However, they are within one CDS pixel of one another and cannot be separated as such.

The background subtraction method outlined in this section improves the resolution of the loops from the background by an order of magnitude, but much work is still required to accurately perform this method for ARs above the limb. A better model will account for the line-of-sight sample of altitudes and will weigh the values for flux at each pixel position accordingly. It must reach a level of complexity to account for the geometry of the field, as arbitrary subtraction of a plane geometry atmosphere is not an accurate estimate of the distribution of mass in the coronal volume. The background is much easier to treat and subtract near disk center where each line-of-sight samples all altitudes with equal weight. The method outlined herein has been applied to several datasets at disk center with consistent results for four different ARs.

We have also done a preliminary study on the predictability of the TRACE observed counts given the spectral emission line intensities collected by CDS. This "idiot" check can tell us several interesting things about the observations and the assumptions made in calculating spectral intensities from packages like CHIANTI. We have used the intensities from CDS to generate a spectrum for the TRACE 173 Å passband, and we have found that CHAINTI does predict the count rates for the TRACE channel to within the errors associated with such a procedure. The estimates of density and temperature are thereby supported by this finding since CHAINTI was used to make these measurements. We have also found that the abundance estimates used in the determination of the spectrum play a factor in the accuracy of the spectrum predicted by CHIANTI. Obvioulsy, this is an interesting application of the results contained in Chapters 3 and 4 and we have discussed the preliminary results with scientists at SAO. We are meeting to discuss a collaboration soon.

One additional point is possible from the analysis of this section. The forbidden and allowed transitions of Si X were used to calculate the density for multiple positions along coronal loops. It was observed while performing these measurements that the intensities of the forbidden 347.403 Å were nearly zero for positions outside coronal loops. It seems as though the resolved coronal loops are at sufficient density to permit the forbidden transition to occur. Background subtraction only really affects the allowed transition at 356.1 Å, reducing its intensity for the pixel on the loop. The ratio of the intensities of these two lines after the background subtraction is only slightly lower than the pre-subtraction value and it is noticed that it is systematically shifted toward the peak density for the forbidden transition to occur. This is an intriguing result that requires more investigation. We plan to do this work at a later date.

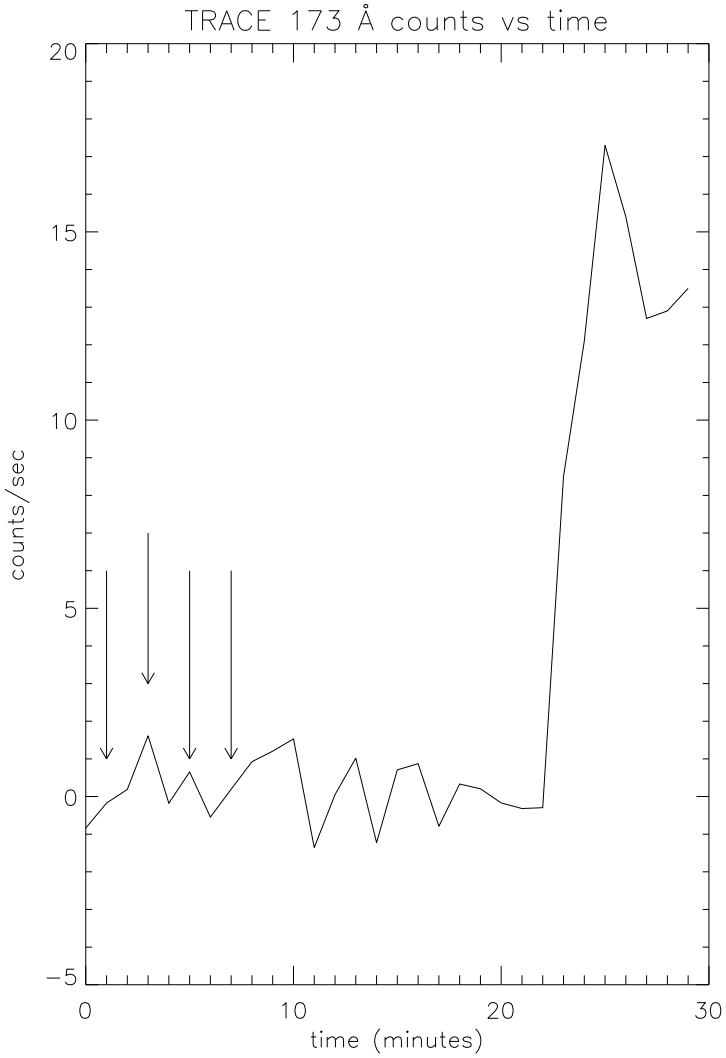

Figure 4.8: TRACE 173 Å counts as a function of time for pixel 3 position (see Figure 4.2) for L-1. The arrows indicate times exposures for CDS intersected L-1. Fourteen minutes passed before substantial counts were observed by TRACE.

CHAPTER 5

SUMMARY OF RESULTS

The EUV AR corona is comprised of an unresolved background and resolved loops. Most often researchers use observations of resolved coronal loops to investigate AR plasma properties such as temperature and density. Here we have analyzed the unresolved corona in three ARs above the limb. Using the results of the unresolved corona, the background for most coronal research, a model of the TRACE 173 Å background is developed and applied to TRACE images. Measurements of the temperature, density, loop-cross section, and TRACE count rates are calculated for three AR loops after subtraction of the background.

Unresolved Corona

Measurement of emission line intensities along a radial line can be used to determine the properties of the plasma contained in an AR. The radial line certainly passes over magnetic field lines that permeate the corona in the AR (see Chapter 1). It is not expected a priori that the observations would indicate the plasma constrained to move along these field lines would be in hydrostatic equilibrium. The physical location and duration of the heating mechanism are the main parameters needed to define a dynamic or static situation. If the injection of energy into the loop occured on a time scale much longer than the radiative and conductive cooling times and was localized relative to the length of the loop, a flow (laminar or turbulent, depending) would be incited and the loop would not be in magneto-hydrostatic equilibrium. Evidence of a turbulent flow could possibly be absorption features and localized brightnings

along the loops at regions of mixed-temperature plasma and enhanced density volume elements along the loops; these were not observed. Yet a complete knowledge of the observational signatures of turbulent flows is not currently known since this would require solution of the coupled non-linear equations governing such motions. Laminar flows are subsonic ($v_p < 100\frac{km}{s}$) and are not easily observed without some sort of tracer moving along with the flowing plasma. This type of flow is much harder to rule out, but the observation that the intensity decreases exponentially with altitude and the exponential decrease can be described by equation 3.3 indicates a laminar flow is not present in the unresolved AR corona. It is without dispute that the intensity decreases can be explained by hydrostatic models and if turbulent flows are present the model for these motions must conform to the observations.

This is an important finding simply because it requires the source of the heating be roughly homogeneous and constant. Fluctuations in the heating, either spatially or temporally, would incite flows and these are not observed. The result in this thesis is unprecedented in its treatment of the coronal AR background, and an extensive liturature search was unsuccessful in finding any relevant article or book that predicted the result. Aschwanden (2004) [40] even points out that it is unlikely that a hydrostatic corona exists in ARs because of their "dynamic nature". It is however an observed fact that the intensity of emission from EUV spectral lines decreases exponentially with altitude, that the unresolved corona constitutes the majority of the total EUV emission in ARs, and the 'background' along the line-of-sight may be accurately subtracted based upon these results increasing the precision of measurement of temperature and density for resolved coronal structures.

AR 9628

AR 9628 produced an M 1.4 flare during JOP 146 observations. The intensity as a function of altitude for this AR was investigated, and it was determined that

an exponential function best fit the observed intensity decrease. The quality of the curve fits indicates that it is highly likely that the post-flare AR unresolved corona is in magneto-hydrostatic equilibrium.

We also found that the scale height temperatures derived from the data show a pronounced increase for all of the ions used in the study following the flare. Despite this increase in temperature, the exponential is still a very good approximation for the intensity decrease with altitude, and the only positions of a marked departure from the exponential trend are associated with post-flare loops. The scale height temperature inferred from data decreases with time after the flare and has nearly returned to the initial observed temperature three hours after the flare occurred.

Flaring ARs are best described by a multi-thermal hydrostatic distribution of unresolved structures along the line-of-sight. As the line-of-sight samples only high altitudes, only high temperature plasma is observed, a consequence of the hydrostatic weighting bias [40]. However, at altitudes below 12 Mm a wide distribution of scale height temperatures has been observed. This helps explain the breadth of the DEM curves produced from spectral line intensities [40].

ARs 10001 and 10249

The deviation of the scale height temperature from the peak formation temperature of the ion is apparently a function of the activity of the AR. For two ARs we studied, the scale height temperature we measured did not match the peak formation temperature of the ion. These ARs did not exhibit any dynamic activity such as a flare or loops that had large brightness variations in time. We determined the scale height temperature from two CDS rasters separated by a few hours, and the change in the calculated values for temperature was negligible.

These quiescent ARs are stable for hours, if not days. In the observed ARs the intensity of emission presented no appreciable indication of local or intermittent

heating. The temperatures calculated from the curve fits to the intensities were also found to be approximately the same, independent of the peak formation temperature of the ion. It is likely, given this observation, that the unresolved corona is in hydrostatic equilibrium. What is unclear from these observations is the distribution of loop lengths. It would seem reasonable to conclude that there are a number of different loop lengths constituting the structures of the unresolved corona. However, these structures are all near the same temperature.

A large study of AR unresolved coronae is planned to develop a statistical sample of AR hydrostatic scale height temperatures. This will help to determine any correlation between the solar cycle and AR activity that could provide evidence for what mechanism is responsible for the heating of these ARs.

Analysis of Background Subtracted Coronal Loops

Adequate application of a background subtraction routine that accounts for the unresolved corona permits accurate measure of the thermodynamical properties of coronal loops. Temporal measurements of these quantities indicate changes to the state of the plasma requisite for inhibited cooling. The theoretical radiative cooling times for the ions used in the results of Chapter Four are a factor of 2 or more shorter than the observed cooling rate, evidence of inhibited cooling. Apparently, heat continues to be deposited into the loops after the initial energy deposition resulting from a flare. This maintains the temperature of the loops, and the location of the heating may be situated close to the loop tops, as these are the first locations to show changes in temperature and density. Since changes in the temperatures and densities of the observed loops are seen to occur near the loop tops, this must be near the source of the heating. No large scale flows are observed in these loops, and the loop cross-sections appear to be constant in time. However, the loop cross-sections do not

appear to be constant along the loop half-length, in contradiction to the results of Porter and Klimchuk (1995) [35]. The changes in the measured width for these loops are larger than the overlap permitted via the error bars. As such, it seems as thought these loops *do* show a variation in width along the length of the loop. The loop width results are not conclusive as it is yet unclear whether the structures observed are actually coherent. It is probable that they are not, and this will only become a conclusive result when higher resolution images become available.

BIBLIOGRAPHY

[1] J. P. Meyer. *ApJ Suppl.*, 57:173, 1985.

[2] R. A. Harrison et al. *Sol. Phys*, 162:233–290, 1995.

[3] B. N. Handy et al. *Sol. Phys*, 187:229–260, 1999.

[4] P. Mazzotta, G. Mazzitelli, S. Colafrancesco, and N. Vittorio. *A & AS*, 133:403, 1998.

[5] J.T. Schmelz, R.T. Scopes, J.W. Cirtain, H.D. Winter, and J.D. Allen. *ApJ*, 556:896–904, 2001.

[6] K. P. Dere and J. W. Cook. *ApJ*, 229:772, 1979.

[7] L. Golub and J. M. Pasachoff. *The Solar Corona.* Cambridge University Press, 1997.

[8] S. Tsuneta, L. Acton, M. Bruner, J. Lemen, W. Brown, R. Caravalho, R. Catura, S. Freeland, B. Jurcevich, and J. Owens. *Sol Phys.*, 136:37–67, 1991.

[9] Delaboudinire et al. *Solar Physics*, 162:291, 1996.

[10] B. Fleck, V. Domingo, and A. Poland, editors. *The SOHO Mission.* Kluwer Academic, 1995.

[11] P. H Scherrer et al. *Solar Physics*, 162:129–188, 1995.

[12] H. Alfvén. *The Solar Corona.* Academic Press, New York, 1963.

[13] H. Alfvén. *Ark. f. Mat. Astr. o. Fysik*, 29B(2):1–17, 1942.

[14] A. R. Choudhuri. *The Physics of Fluids and Plasmas.* Cambridge, 1998.

[15] G. S. Vaiana and R. Rosner. *Ann. Rev. Astron. Astrophys.*, 16:393–428, 1978.

[16] E. Priest and T. Forbes. *Magnetic Reconnection.* Cambridge, 2000.

[17] D. W. Loncope and P. C. H. Martens. *MSU physics course 580*, 2003.

[18] D. M. Rust. *thesis, University of Colorado, Boulder*, 1966.

[19] G. A. Newkirk. *Annual Review of Astronomy and Astrophysics*, 5:213, 1967.

[20] G. V. Rudenko. *Solar Physics*, 198:5–30, 2001.

[21] Y. M. Wang and N.R. Sheeley Jr. *ApJ*, 392:310–319, 1992.

[22] K. H. Schatten and J.M. Wilcox. *Solar Physics*, 6:442–455, 1969.

[23] J. T. Mariska. *The Solar Transition Region*. Cambridge University Press, 1992.

[24] V. Trimble and M. J. Aschwanden. *PASP*, 116:187–265, 2004.

[25] A.R. Winebarger, H.P. Warren, and D.B. Seaton. *ApJ*, 593:1164–1173, 2003.

[26] M.J. Aschwanden, R.W. Nightingale, and D. Alexander. *ApJ*, 541:1059–1077, 2000.

[27] D.D. Lenz, E.E. DeLuca, L. Golub, R. Rosner, and J.A. Bookbinder. *ApJ*, 517:L155–158, 1999a.

[28] R.P. Lin et al. *Solar Physics*, 210(1):3–32, 2002.

[29] B. H. Bransden and C.J. Joachain. *The Physics of Atoms and Molecules*. Prentice Hall, 2003.

[30] G. Athay. *Radiation Transport in Spectral Lines*. D. Reidel Publishing, 1971.

[31] L. Golub, L. Herant, K. Kalata, I. Lovas, G. Nystrom, E. Spiller, and J. Wilcyznski. *Nature*, 344:842, 1990.

[32] Del Zanna G. and H. Mason. *A & A*, 406:1089–1103, 2003.

[33] P. C. H. Martens, J. W. Cirtain, and J. T. Schmelz. *ApJ*, 577:L115, 2002.

[34] P. Testa, G. Peres, and F. Reale. *ApJ*, 580:1159–1171, 2002.

[35] L.J. Porter and J.A. Klimchuk. *ApJ*, 220:643–665, 1995.

[36] S. V. H. Haugan. *private communication*, 2004.

[37] H. P. Warren. *Sol Phys*, 190:363–377, 1999.

[38] K. Wilhelm et al. *Sol Phys*, 162:189–231, 1995.

[39] M. J Aschwanden and N. Nitta. *ApJ*, 535:L59, 2000.

[40] M. J. Aschwanden. *Physics of the Solar Corona*. Springer Praxis, 2004.

[41] H. E. Mason, P. R. Young, C. D. Pike, R. A. Harrison, A. Fludra, B.J.I. Bromage, and G Del Zanna. *Solar Physics*, 170:143–161, 1997.

[42] P. C. H. Martens, C. C. Kankelborg, and T. E. Berger. *ApJ*, 537:471, 2000.